1 Basic Description of Structural Architecture in Transform Margin Settings

1.1 Introduction

Throughout this book, we will consider in detail many aspects of strike-slip faults in general, and transform margins in particular. The aim of this introductory chapter is to focus on the classification of the various types of strike-slip faults, and on their structural architecture.

In order to understand structural styles of transform margins, one needs to discuss continental strike-slip fault zones and pull-apart basins, transform margin precursors represented by continental transforms and continent–ocean transforms, and to consider their tectonic development histories, controlling dynamics, and resultant structural architecture. Because transform margins evolve through the continental–oceanic stage, a discussion of ridge transform faults and associated oceanic fracture zones is also required. This overview aids understanding of the structural architecture of the oceanic side of the continental–oceanic transform fault zone, its development history, its controlling dynamics, and the way they affect the evolution of the adjacent continental side, which subsequently evolves into the future transform margin.

1.2 Classification of Strike-Slip Faults

Strike-slip faults are faults with the dominant component of the slip vector being parallel to the fault strike (Le Pichon et al., 1973; Bates and Jackson, 1987). Serving as more-or-less restraining structures, continental strike-slip faults have a geometry related to the controlling stress field; that is, their structural architecture is controlled by the evolving hosting mechanical stratigraphy and local stresses (e.g., Gerya, 2016).

Strike-slip fault classification represents a problem, because the continental examples do not function as steady-state features (e.g., Gerya, 2016). Instead, they progressively evolve, and adjust their location and geometry with time (e.g., Norris and Toy, 2014). As discussed in Chapter 5, on top of changing their tectonic position and geometry, strike-slip faults can progressively increase their lateral and vertical extent to the point where they involve lithospheric layers other than the one where they nucleated. This is the main reason why most older classifications, which divide strike-slip faults based on their extent, do not work very well, classifying strike-slip faults based on snapshots and not on their entire development history.

If we want to use currently available strike-slip classifications (e.g., Wilson, 1965; Sylvester, 1988; Twiss and Moores, 1992), we can try to edit them with the understanding that some of their categories do not necessarily describe fully mature strike-slip faults but their earlier evolutionary stages. For example, based on their interplate versus intraplate extents, strike-slip faults can be divided into transform faults (Wilson, 1965), which are cut through the entire lithosphere in their fully developed stage, and transcurrent faults, which remain inside the lithosphere even in their fully mature stage (Sylvester, 1988; Table 1.1; Figure 1.1). This approach will ensure that the classification we use honors a relatively new understanding that the structural architecture of continental transforms develops gradually, and that these faults tend to utilize preexisting lithospheric anisotropy during their propagation (Norris and Toy, 2014). This approach will also honor the new concept (see Gerya, 2010, 2013a, 2016) that the spontaneous development of ridge transforms in numerous spreading systems needs a several-million-year time period of gradual development to reach a steady state.

Even such an edited classification is still problematic, because continental transforms and some oceanic transforms have controlling dynamics, development history, and structural architecture different from each other. Therefore, before we discuss characteristic features of individual strike-slip fault categories and typical natural examples of these (Table 1.1), we need to look at these differences.

https://doi.org/10.1017/9781108686631.002

Table 1.1 Strike-slip fault classification (modified from Wilson, 1965; Bally, 1982; Bosworth, 1985; Rosendahl et al., 1986; Woodcock, 1986; Mascle and Blarez, 1987; Rosendahl, 1987; Sylvester, 1988; Versfelt and Rosendahl, 1989; Morley et al., 1990; Ratschbacher et al., 1991a; Twiss and Moores, 1992; Detrick et al., 1993; Younes and McClay, 2002; Destro et al., 2003; Bonatti et al., 2005; Govers and Wortel, 2005; Sclater et al., 2005; Escalona and Mann, 2006; Nemčok et al., 2006a; Gregg et al., 2007, 2009; Roland et al., 2010; Ben-Avraham et al., 2012; Géli et al., 2014; Maia et al., 2016; Morrow et al., 2016; Kolandaivelu et al., 2017; Burg, 2018).

Transform faults (cut through entire lithosphere, in some cases at least in their fully developed stage)	
Transform faults linking ridge with ridge (Figures 1.1, 1.2a)	Relatively dynamically stable transforms that displace segments of oceanic lithosphere accreted under similar spreading vectors and most likely different spreading rates (the term oceanic fracture zones describes their two inactive portions beyond the transform intersections with neighbor ridges) Present-day active examples: Atlantis, Charlie Gibbs, Hayes, Kane, Oceanographer, Pico and Vema transforms, slow-spreading Mid-Atlantic Ridge region Clarion, Discovery, Garrett, Gofar, Orozco, Quebrada and Siqueiros transforms, fast-spreading East Pacific Ridge region Blanco transform separating Juan de Fuca and Gorda ridges, offshore Oregon Large-offset Romanche and St. Paul slowly slipping transforms of the Equatorial Atlantic Andrew Bain, Du Toit, Marion and Prince Edward transforms, slow Southwest Indian Ridge region Menard transform, Pacific-Antarctic Ridge region Guamblin transform, Chile Rise Ecuador transform separating Costa Rica and Ecuador rifts
Transforms evolved from the continental transform stage, through the oceanic–continent transform stage, into the transform margin stage (Figures 1.1, 1.6a)	Transforms that cut through the continental lithosphere linking two nucleated spreading centers, which subsequently evolve to oceanic–continental transforms as two continental blocks clear each other and continental sides are juxtaposed with laterally passing oceanic crust and its associated spreading center. Their subsequent inactive portions are transform margins juxtaposed with progressively cooling oceanic lithosphere. Examples: Romanche (Figure 1.6b) and St. Paul transforms of the Equatorial Atlantic that underwent their ocean–continent stages during the Albian–Campanian and Albian–Cenomanian, respectively Zenith–Wallaby–Perth and Cape Range transforms in West Australia that underwent their ocean–continent stages during the Barremian–Albian and Valanginian–Barremian, respectively
Transforms linking ridges with convergent plate boundary (Figures 1.1, 1.7a). The two subtypes of this category include transforms that link the ridge with overriding versus subducting plates of the subduction zone.	Transforms with tendency to change their length Examples: the eastern portion of the northern boundary of the Caribbean Plate; i.e., transform fault zone linking the spreading center in the Cayman Trough with the accretionary wedge at the eastern front of the Caribbean Plate (Figure 1.8a) The San Andreas Transform linking the subduction zone, where the North American Plate overrides the Pacific Plate, with a system of spreading centers in the Gulf of California (Figure 1.7a) The Dead Sea Transform linking the spreading ridges of the Red Sea with the overridden plate of the Arabia–Eurasia collisional zone (Figure 1.12) The Sagaing Transform linking the spreading center of the central Andaman Basin with the overridden plate of the India–Eurasia collisional zone (Figure 1.9) The Queen Charlotte Transform linking the spreading ridge with the subducting plate of the subduction zone

https://doi.org/10.1017/9781108686631.002

Table 1.1 (cont.)

Transforms linking convergent plate boundaries (Figure 1.2a). The two subtypes of this category include transform faults that link either two overriding or overridden plates. The third subtype includes a linkage of the overriding one with overridden one. Further combinations arise when we divide convergence zones into subduction and collision zones.	Transforms with tendency to change their length Examples: the Alpine Transform in New Zealand, linking a combination of overriding and overridden plates The fault system forming the southern boundary of the Caribbean Plate, linking the overriding Caribbean Plate of the subduction zone with the overriding plate of the Nazca–South America subduction zone (Figure 1.8a) The Chaman Transform linking a combination of the overriding Eurasian Plate with the Makran Range and overridden Indian Plate of the India–Eurasia collisional zone (Figure 1.12) The North Anatolian Fault linking the overriding plate of the Arabia–Eurasia collision zone with the overriding plate of the Hellenic subduction zone (Figure 1.12) The East Anatolian Fault linking the overriding plate of the Arabia–Eurasia collision zone with the overriding plate of the Anatolia–Africa subduction zone (Figure 1.12)
Trench-linked strike-slip faults (Figure 1.1)	Strike-slip faults that accommodate the horizontal component of oblique subduction Examples: Atacama Fault, Chile, South Japan Sea Fault Zone and Median Tectonic Line, Japan, Sumatran Fault (Figure 1.9)
Transcurrent faults (reside inside lithosphere even in their fully developed stage)	
Indent- and lateral extrusion-linked strike-slip faults (Figure 1.1)	Strike-slip faults that separate continental blocks that move with respect to each other in the convergent plate setting Examples: Red River Fault, Steinberg Faults and Farské, Schrattenberg-Bulhary, and Central Hungarian Fault zones in the Western Carpathian–Pannonian region (Figure 1.10), Moesian Platform Faults in front of the Carpathians (Figure 1.11)
Transfer faults	Strike-slip faults that transfer horizontal slip component from one set of faults to another set of faults. They include: accommodation zones, transfer zones and interference accommodation zones Examples: Jeremboabo Fault in the Jatobá–Tucano–Reconcavo Rift Zone, NE Brazil, Rukwa Transfer Zone between Malavi and Tanganyika Rift Zones, East African Rift System The Garlock Fault separating the Central Basin and Range Province with the larger amount of extension and the Mojave Block with the smaller amount of extension Kala Bagh and Jhelum faults bounding the Potwar Plateau on its east and west sides (Figure 1.15a), Pakistan Faults along the east and west sides of the Sulaiman Range, Pakistan (Figure 1.15b)
Tear faults	Strike-slip faults that accommodate differential displacement within a specific allochthon or between allochthon and its adjacent structural units Examples: Jacksboro and Russell Fork Faults bounding the Pine Mountain thrust sheet from SW and NE, respectively, in the Appalachians A dense system of tear faults deforming the frontal portion of the northern Variscan orogenic belt in Southern Wales, UK (Figure 1.16a)
Small-scale conjugate strike-slip fault systems in individual thrust sheets	Strike-slip faults with a role to accommodate for the coeval strike-parallel stretching and orthogonal shortening. Examples: small-scale conjugate strike-slip faults in individual frontal anticlines of thrust sheets in the Eastern Carpathians, Romania, Makran and Sulaiman Ranges (Figure 1.17), Pakistan, Jura fold and thrust belt, Switzerland

https://doi.org/10.1017/9781108686631.002

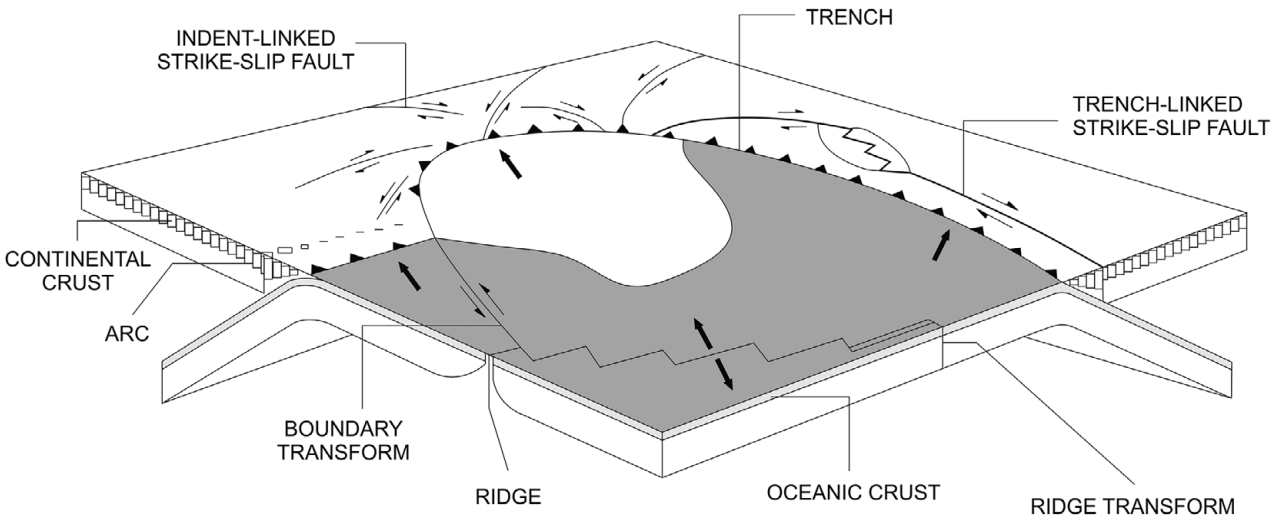

Figure 1.1 Schematic diagram showing different types of strike-slip faults (Woodcock and Fischer, 1986).
Reprinted from the *Journal of Structural Geology*, 8, Woodcock, N. H. and Fischer, M., Strike-slip duplexes, 725–735. ©1986, with permission from Elsevier.

While continental transforms are plate deformation structures (see Norris and Toy, 2014 and references therein), transforms linking spreading ridges in intermediate, fast, and some slow spreading systems are plate growth structures once they reach their steady-state development (Gerya, 2012, 2013a).

The structural architecture of continental transforms develops gradually and tends to utilize pre-existing lithospheric anisotropy during transform propagation (Norris and Toy, 2014). Plate boundary localization in the case of continental transforms requires a significant perturbation of composition, stress, or temperature in the lithosphere or the underlying asthenosphere (Molnar and Dayern, 2010; Burov and Gerya, 2014). Evidence from numerous continental transforms discussed in Chapter 5 indicates that all of them started their development as broad deformation zones, where a dominant fault zone developed subsequently (e.g., Atwater, 1970; Şengör, 1979; Sutherland, 1995; Yue and Liou, 1999; Norris and Toy, 2014). They try to establish Andersonian geometry with respect to their controlling stress field (see Anderson, 1951), but deviation from the Andersonian geometry is caused by both the effect of pre-existing zones of weakness (e.g., Wallace, 1951), as discussed in Chapter 6, and adjustment to the required plate boundary geometry.

Observations and modeled scenarios indicate that oceanic transforms in ultra-fast, fast, intermediate-fast, and some slow spreading systems in their mature stages are not plate deformation structures like continental transforms. Rather, they are plate growth structures (Gerya, 2010, 2013a, 2016). They serve as lubricants for displacement of segmented plates undergoing coeval divergence and accretion. They do not have Andersonian geometry (Anderson, 1951) with respect to their controlling stress field. Instead, they are parallel to the σ_3 direction. They represent features promoted by dynamic instability controlled by the asymmetric lithospheric accretion enabled by strain-weakening faults (Gerya, 2010). This instability is most distinct in model runs at spreading rates of 38–57 mmy^{-1}, which is in accordance with observations of orthogonal transform patterns less typical for spreading systems that are faster and slower than this range of spreading rates (e.g., Naar and Hey, 1989; Dick et al., 2003; Kriner et al., 2006; Gerya, 2010; Puthe and Gerya, 2014).

While transform seismicity is characterized by magnitudes smaller than those of subduction and collision settings (Gerya, 2016), there is a difference between continental and oceanic transforms.

Continental transforms are characterized by more-or-less diffuse active faulting and, frequently, only a fraction of the plate displacement is accommodated by seismoactive faulting (e.g., Sibson, 1983; Field et al., 2009; Carpenter et al., 2011). The San Andreas Fault, for example, indicates a phyllosilicate-rich foliated and fluid-saturated fault core, which is considerably weaker than the host rock and is unable to frictionally heal (e.g., Moore and Rymer, 2007; Collettini et al., 2009), controls fault displacement by aseismic creep along most of its segments (Carpenter et al., 2011). Seismoactive faults of continental transforms are not continuous, but are divided into segments separated by step-like discontinuities (Wesnousky, 2006).

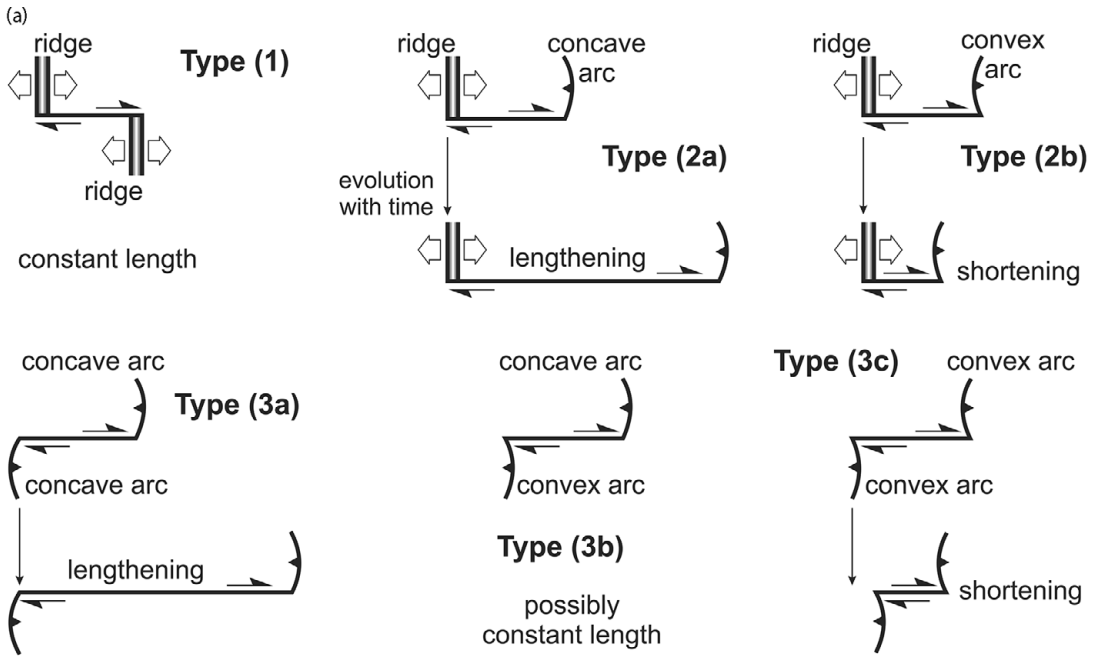

Figure 1.2 (a) Basic types of transforms based on the possible configurations of neighbor plate boundaries (Wilson, 1965). Reprinted by permission from Springer Nature: *Nature*. Wilson, J. T. A new class of faults and their bearing on continental drift. 207, 343–347. ©1965.

Oceanic transforms are characterized by more-or-less concentrated faulting and most of the plate displacement is accommodated by aseismic creep (Brune, 1968; Davies and Brune, 1971; Kanamori and Stewart, 1976; Frohlich and Apperson, 1992; Okal and Stewart, 1992; Okal and Langenhorst, 2000; Bird et al., 2002; Boettcher and Jordan, 2004). Mature oceanic transforms are distinctively weak (Gerya, 2010, 2013a; Allken et al., 2012). The weakness is interpreted to be caused by deep hydration and serpentinization (e.g., Escartín et al., 2001; Hilairet et al., 2007; Korenaga, 2007). Faults composing the oceanic transform tend to be linear and their earthquake magnitudes are small (Gerya, 2016). The few larger magnitudes characterize either new transform propagation (e.g., Delescluse et al., 2012; McGuire and Beroza, 2012) or the reactivation of oceanic fracture zones (Robinson, 2011) in some cases.

1.3 Interplate Strike-Slip Faults

1.3.1 Transform Faults Linking Ridge with Ridge

This type of transform (Figure 1.2a) separates blocks of oceanic lithosphere in intermediate and some fast and some slow spreading systems, where the described spreading rate categories are using criteria from Small (1998), Dick et al. (2003), and Kriner et al. (2006). The structural architecture in this case can be characterized as an orthogonal pattern of transforms (e.g., Freund and Merzer, 1976; Figures 1.2b, 3.2a, and 3.2e; S3 architecture in Figure 1.2c). This pattern evolves in the following different lithospheric settings:

1) some slow spreading systems that develop a new oceanic lithosphere by magma-assisted spreading; and
2) intermediate and fast systems that develop a new oceanic lithosphere by magma-assisted spreading.

It needs to be emphasized that the structural architecture is rather different in spreading systems that are either faster or slower than the aforementioned systems (Figure 1.2c). For example, observations and modeling indicate that ultra-slow and some slow spreading systems do not develop well-pronounced transforms, but rather curved spreading centers (Shemenda and Grocholsky, 1994) or oblique amagmatic spreading sections (Dick et al., 2003; Puthe and Gerya, 2014) instead of transforms (S1 architecture in Figure 1.2c). Oblique shear zones were described, for example, from some segments of the slow spreading Mid-Atlantic Ridge (Schouten and White, 1980; Sempere et al., 1993). This tectonic setting evolves in pre-existing lithosphere affected by stretching.

In the case of some modeled fast spreading systems, transforms are initially possible but do not represent a

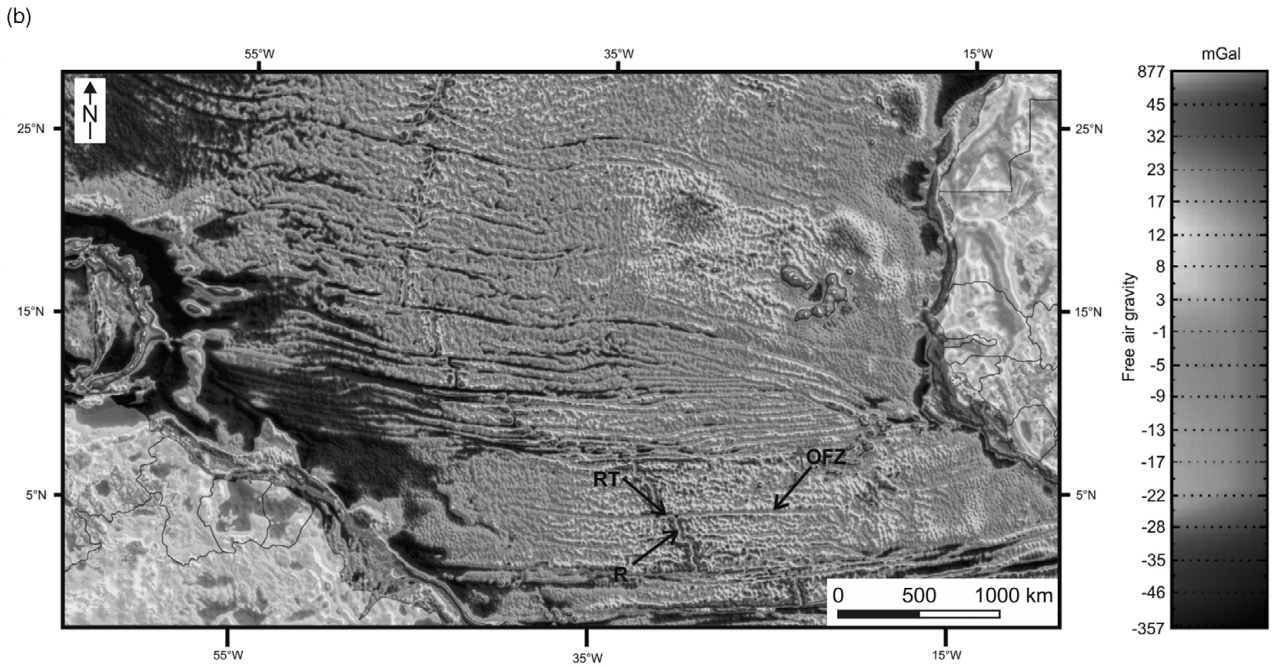

Figure 1.2 (b) Free-air gravity anomaly map of the southern Central Atlantic and western Equatorial Atlantic imaging a system of Mid-Atlantic Ridge segments and linking ridge transforms (modified from Nemčok et al., 2015a). Abbreviations: OFZ – oceanic fracture zone, R – spreading ridge segment, RT – ridge transform.

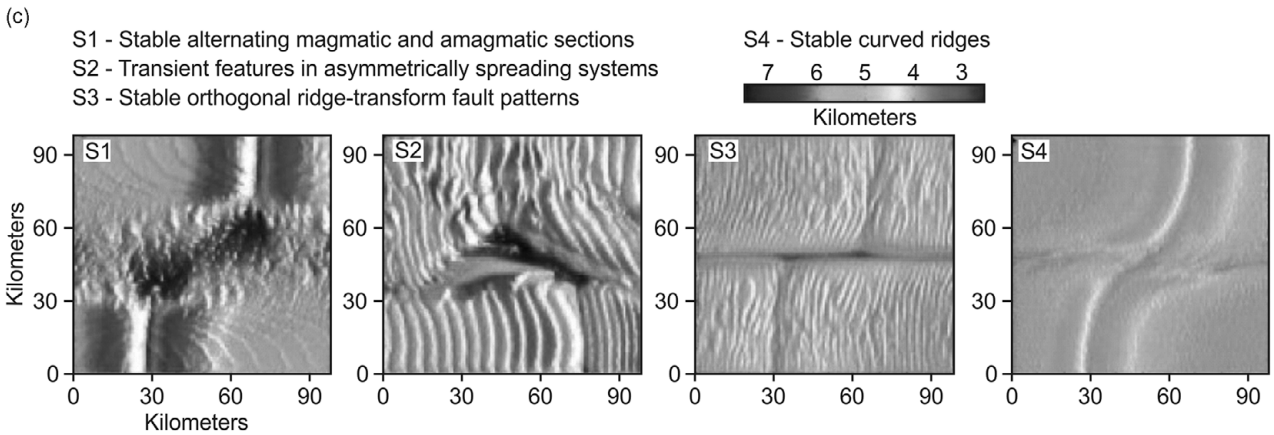

Figure 1.2 (c) Dependence of structural architecture of the spreading system on the spreading rate as indicated by numerical modeling (Puthe and Gerya, 2014). Architectures S1, S2, S3, and S4 represent rates of 10 mmy^{-1}, 20 mmy^{-1}, 40 mmy^{-1}, and 80 mmy^{-1}, respectively. See text for further explanation.

Reprinted from *Gondwana Research*, 25. Puthe, C. and Gerya, T. Dependence of mid-ocean ridge morphology on spreading rate in numerical 3-D models. 270–283. ©2014, with permission from Elsevier.

steady-state feature, because they become replaced by curved ridge sections after a few million years (Gerya, 2016; S4 architecture in Figure 1.2c). Furthermore, the models of ultra-fast systems are characterized by the absence of transforms at rates exceeding 140 mmy^{-1} (Naar and Hey, 1989; Kriner et al., 2006). Ridge offsets are accommodated by microplates, propagating rifts, and overlapping spreading centers (Kriner et al., 2006). Overlapping centers are described, for example, from some segments of the fast spreading East Pacific Rise (Macdonald and Fox, 1983; Lonsdale, 1985). Both fast and ultra-fast systems evolve in magma-assisted crust and lithospheric mantle affected by dominating buoyancy forces and subordinate stretching.

https://doi.org/10.1017/9781108686631.002

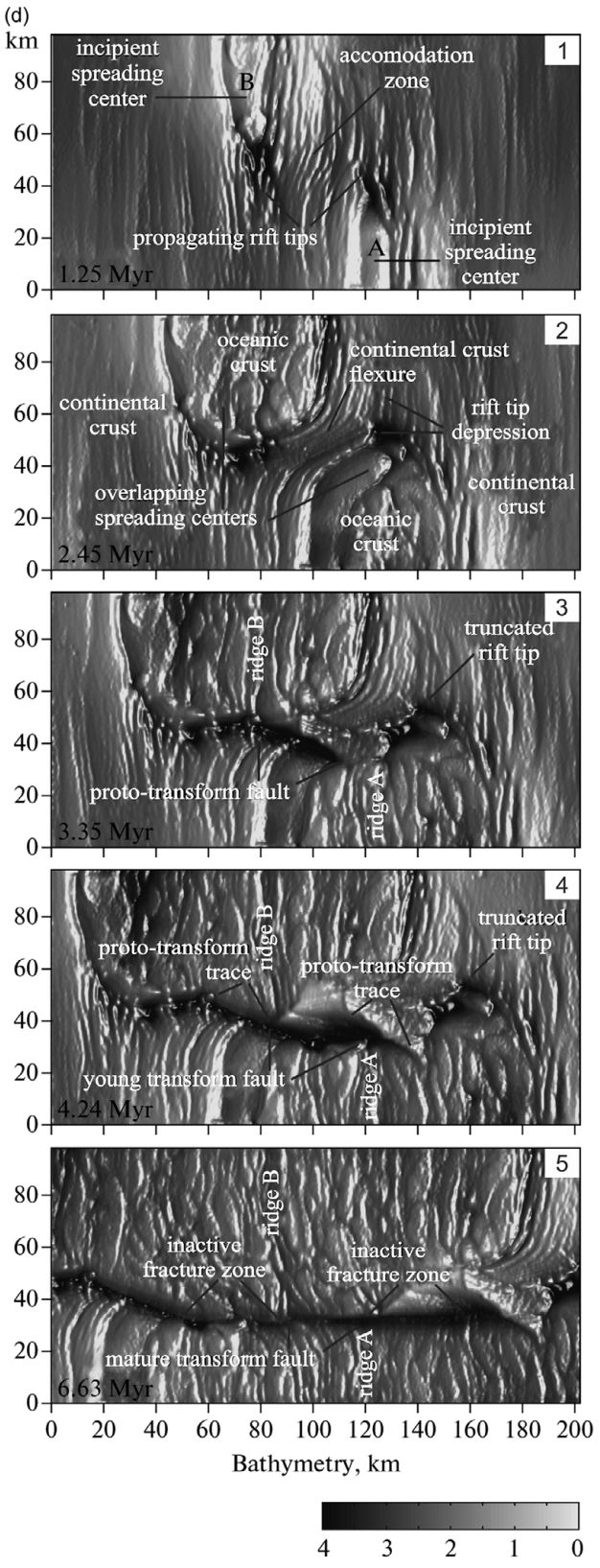

The aforementioned non-transform discontinuities from both very slow and very fast spreading systems can be characterized as follows. Those not exceeding a length of a few tens of kilometers are short-lived and known to be able to migrate along the strike of the spreading system (Macdonald et al., 1991). The longer ones are more stable, able to last several million years. Unlike ridge transforms, their outboard extensions do not form small circles reflecting the pole of relative motion (Detrick et al., 1993).

A steady-state transform representing intermediate, some fast and some slow spreading systems is composed of a zone of distinct troughs and ridges, which can be more than several tens of kilometers wide (Figures 3.5c, 3.13a–c, 3.16, and 7.23). Their elevation difference from the top of the undeformed oceanic crust can reach several kilometers (Figures 3.13a, 3.13c, 7.23). Individual strike-slip faults of the transform represent a narrow fault zone along which oceanic plate segments are passing each other horizontally (Detrick et al., 1993). It is relatively stable for millions of years. Ridge transform faults of intermediate, fast and some slow spreading systems are commonly perpendicular to the spreading ridge segments and parallel to the spreading–controlling extension (Oldenburg and Brune, 1972; Gerya, 2016; Figure 1.1) once they reach the steady-state development (Figure 1.2d). They play an important role in affecting the thermal regime, mantle flow, melting, and crystallization at mid-oceanic ridges (Fox and Gallo, 1984; Parmentier and Forsyth, 1985; Phipps Morgan and Forsyth, 1988). Active, ridge-connecting transforms, which are usually tens to hundreds of kilometers long, extend further out from between the spreading ridges as inactive oceanic fracture zones of similar geometry (Detrick et al., 1993; Gregg et al., 2007; Figures 1.2b and 1.3). These extensions, represented either by zones of weakness or locked fault systems, can be occasionally reactivated in cases of spreading vector and rate changes, and main plate motion changes (Gomes et al., 2000; Robinson, 2011).

Figure 1.2 (d) Numerically simulated development of the ridge transform fault (Gerya, 2013a), representing (1) propagating spreading centers reaching each other, (2) overlapping centers, (3) proto-transform development stage, (4) transform nucleation stage, and (5) transform growth stage. Republished with permission of Springer Nature from Initiation of transform faults at rifted continental margins: 3D petrological–thermomechanical modeling and comparison to the Woodlark Basin. Gerya, T., *Petrology*, 21(6), 550–560. ©2013. Permission conveyed through Copyright Clearance Center, Inc.

https://doi.org/10.1017/9781108686631.002

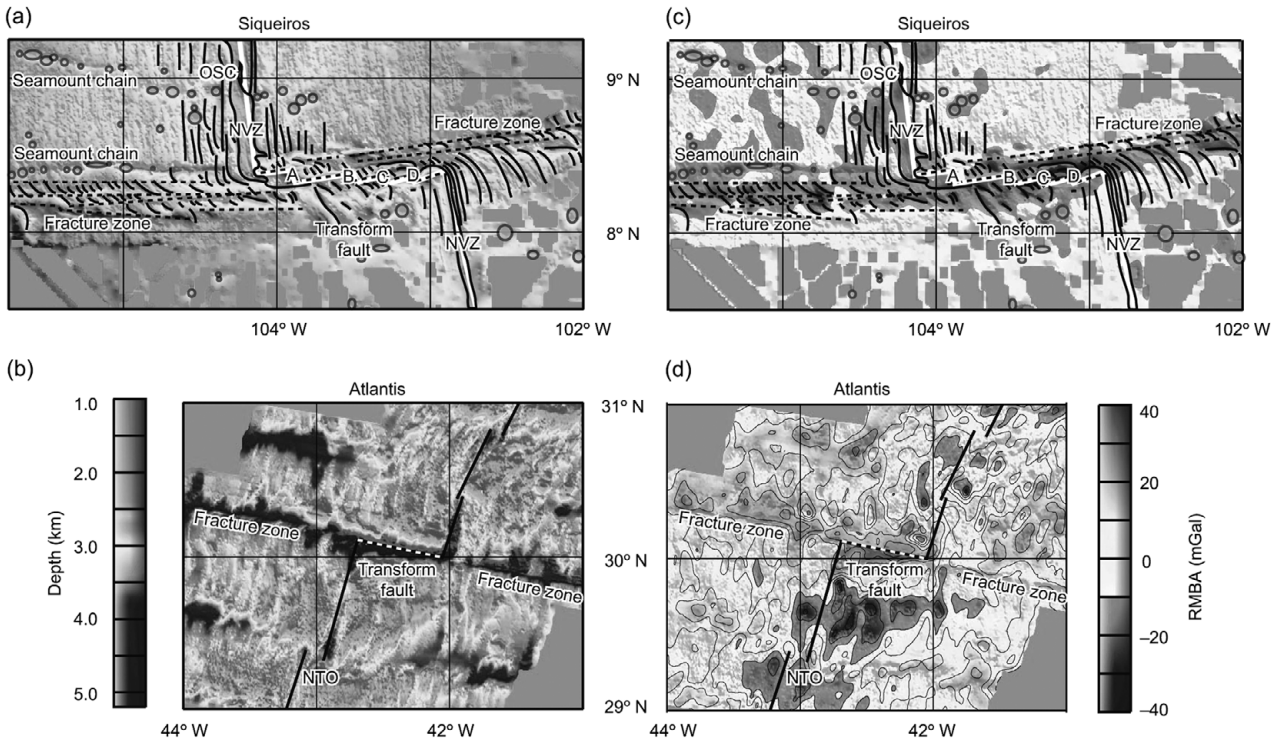

Figure 1.3 Bathymetric and residual mantle Bouguer anomaly maps of fast slipping Siqueiros and slow slipping Atlantis ridge transforms (Gregg et al., 2007). (a) Bathymetric map of the Siqueiros Transform. Solid black lines – structural architecture of oceanic crust, dashed black lines – transform and oceanic fracture zone locations, circles – seamount locations, white line – plate boundary. NVZ – neo-volcanic zone, OSC – overlapping spreading center. (b) Bathymetric map of the Atlantis Transform. Black and white lines indicate transform and spreading centers. NTO – non-transform offset. (c) Residual mantle Bouguer anomaly map of the Siqueiros Transform. (d) Residual mantle Bouguer anomaly map of the Atlantis Transform.

Furthermore, because the thermal contraction continues as the oceanic lithosphere drifts away from the spreading ridge, some dip-slip displacement can be expected along oceanic fracture zones. In these cases, the older lithosphere forms the hanging wall. In most cases oceanic fracture zones are aseismic. They can be traced for thousands of kilometers (Figure 1.2b) onto the ridge flanks as small circles reflecting both the direction of plate motion and the divergence of plates on either side of the ridge, as a function of rotation around an Euler Pole (Menard and Chase, 1970).

In contrast to continental strike-slip faults, the ridge transforms may show opposite displacement sense within a pattern characterized by the same strike. Furthermore, the displacement sense of the ridge transform can be opposite to what is apparent from the spreading ridge offset.

The thermal regime and mechanical behavior of ridge transforms are distinctively different from those of continental transforms. This is due to heat conduction and advection from the warmer, younger plate into the older, colder plate (Louden and Forsyth, 1976; Roland et al., 2010; Kolandaivelu et al., 2017) and the elastic layer development, which both cause ridge transforms to have unusual topographic and gravimetric structure (Sandwell and Schubert, 1982; Sandwell, 1984; Pockalny et al., 1996).

As documented by submersible studies of the Oceanographer and Vema ridge transforms (OTTER Scientific Team, 1985; Auzende et al., 1989), the walls of both transform faults and their oceanic fracture zones represent steep outcrops of basaltic, gabbroic, and ultramafic rocks. Furthermore, the crustal architecture of ridge transform faults and their oceanic fracture zones differ from that of normal oceanic crust (Detrick et al., 1993, and references therein). Slow slipping Atlantic Transforms and their fracture zones cut the oceanic crust, which is thinner than normal (Figure 1.4). Mantle Bouguer anomaly images of these transforms are represented by anomalies that are more

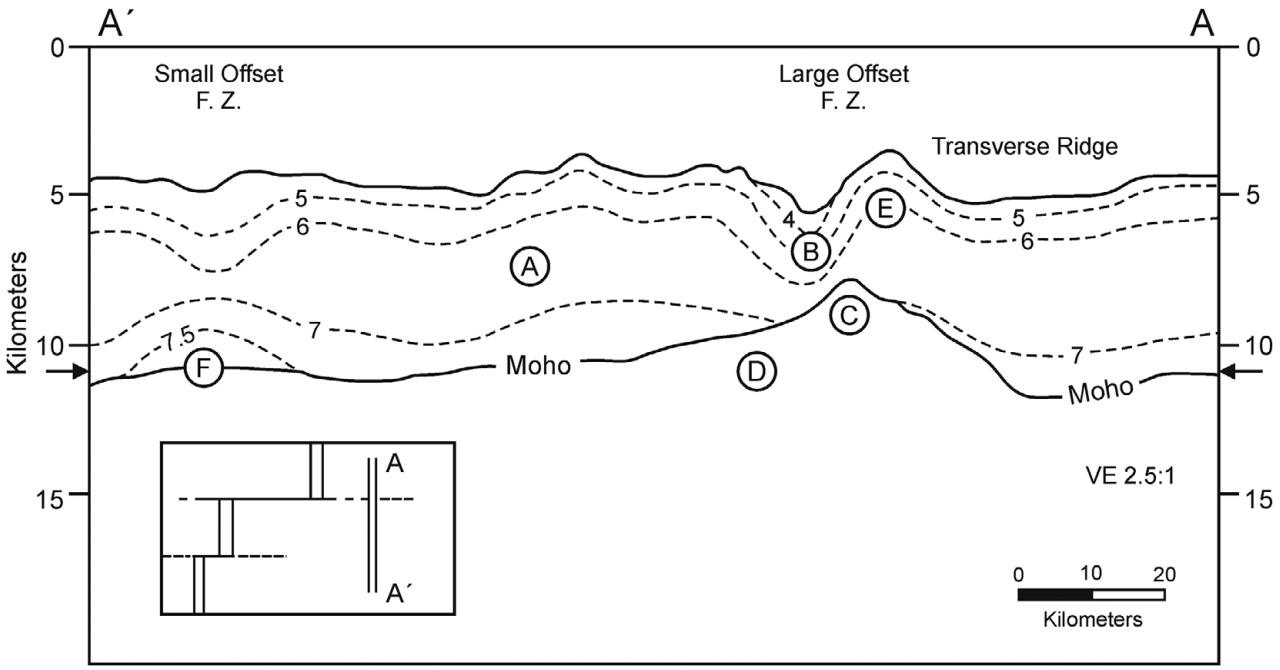

Figure 1.4 Schematic cross section across a typical North Atlantic oceanic fracture zone (Detrick et al., 1993). A – normal oceanic crust. B – thin crust of the oceanic fracture zone, lacking the seismic layer representing the gabbro layer and characterized by unusually low compressional wave velocities. C – the thinnest crust underlying the transform valley. D – gradually thinning crust up to 20 km from the oceanic fracture zone. E – transverse ridge bordering the oceanic fracture zone, characterized by relatively normal compressional wave velocities, relatively normal crustal thickness, and Moho upwarping. F – partially serpentinized upper mantle underlying some oceanic fracture zones. Reprinted with permission from John Wiley and Sons. Detrick, R. S., R. S. White, and G. M. Purdy (1993), Crustal structure of North Atlantic Fracture Zones, *Rev. Geophys.*, 31(4), 439–458.

positive than anomalies of neighboring spreading centers (Kuo and Forsyth, 1988; Lin et al., 1990; Lin and Phipps Morgan, 1992; Detrick et al., 1995).

Mantle Bouguer anomaly maps of the slow spreading Mid-Atlantic Ridge indicate a significant crustal structure asymmetry at ridge transform intersections, characterized by thinner and thicker crust at inside and outside corners, respectively (Detrick et al., 1993). The inside corners frequently contain oceanic core complexes exhumed in footwalls of upward convex detachment faults (e.g., Cann et al., 1997; Cannat et al., 1997; Ranero and Reston, 1999; Tucholke et al., 2001; MacLeod et al., 2002; Escartín et al., 2003). Typically, the crust of these oceanic fracture zones (Figure 1.4):

1) is very thin;
2) is characterized by very low compressional wave velocities;
3) is characterized by rather high velocity gradients;
4) lacks a gabbro layer;
5) is sometimes thinnest underneath the deepest trough, sometimes underneath the trough flanks;
6) thins very abruptly between the normal oceanic crust and oceanic fracture zone; and
7) contains transverse ridges with relatively normal crustal thickness that represent distinct topographic highs and are underlain by upwarped Moho.

The thinner crust of transform faults and nontransform offsets at slow spreading systems (see also Kuo and Forsyth, 1988; Lin et al., 1990; Blackman and Forsyth, 1991; Lin and Phipps Morgan, 1992; Tolstoy et al., 1993) is interpreted as the result of reduced magma supply at the ends of individual spreading segments due to mantle upwelling targeting segment centers (Fox and Gallo, 1984; White et al., 1984; Phipps Morgan and Forsyth, 1988; Lin et al., 1990; Sparks and Parmentier, 1993; Canales et al., 2000) and stretching dominating in the inside corners of their intersections (Mutter and Karson, 1992).

Furthermore, a transform-controlled juxtaposition of the older, colder lithosphere to a warm spreading center causes an important perturbation of the thermal regime and affects the extruded lava composition (Bender et al., 1978, 1984; Langmuir and Bender, 1984; Reynolds et al., 1992; Reynolds and Langmuir, 1997; Gregg et al., 2009).

https://doi.org/10.1017/9781108686631.002

In contrast to slow slipping ridge transforms, fast slipping Pacific Transforms and their fracture zones cut the oceanic crust, which is thicker than normal, while the thickness can vary from transform segment to transform segment (Fox and Gallo, 1984; Macdonald et al., 1988; Canales et al., 2003). Mantle Bouguer anomaly images of these transforms are represented by anomalies that are more negative than anomalies of neighboring spreading centers (Gregg et al., 2007, 2009). Apart from the subordinate effect of increased fracture-related porosity and mantle serpentinization on the aforementioned gravity image, local crustal thickness changes play the dominant role (Gregg et al., 2007). The increased crustal thickness can be explained by a combination of (Menard and Atwater, 1969; Fornari et al., 1989; Perfit et al., 1996; Begnaud et al., 1997; Karson et al., 2002; Gregg et al., 2009):

1) lateral magma transport from the spreading ridge into the transform fault zone;
2) magma-rich accretion of oceanic crust at intra-transform spreading centers;
3) lava pooling in transform troughs; and
4) general leaky magmatic accretion along the entire transform length.

Numerical simulations by Gregg et al. (2009) indicate that the key control of the crustal thickness variations associated with a specific pattern of intra-transform spreading centers and linking transform faults is the volume of mantle over which melt is pooled. The longer the intra-transform center length, the greater the extent of melting and the smaller the average melting pressure.

The Atlantis Transform, which offsets the Mid-Atlantic Ridge at about 30°N, is an example of a slow slipping transform (24 mmy^{-1}) (Figure 1.3). Its structural architecture is represented by a single strike-slip fault zone (Figure 1.5a). This is analogous to other slow slipping transforms, although exceptions, such as the slow slipping Romanche and Andrew Bain Transforms in the Equatorial Atlantic and Southwest Indian Ocean, respectively, are characterized by wide complex deformation zones resembling those of continental transforms (Ligi et al., 2002; Sclater et al., 2005). The calculated depth of serpentinization at the Atlantis Transform reaches mantle levels (Gregg et al., 2007).

An example of a transform affected by a hotspot is seen in the north of Iceland. Here the extensional transform zone links the sub-aerially exposed neo-volcanic zone of northeast Iceland with the Kolbeinsey Ridge, located to the north in the Norwegian–Greenland Sea, in a left-lateral step (Figure 8.2a). The Tjörnes Fracture Zone is a 75 km wide zone of extensional grabens and strike-slip faults (Hannington et al., 2001). Its structural architecture is complex, resembling that of fast slipping transforms, yet its strike is at a low angle to the σ_3

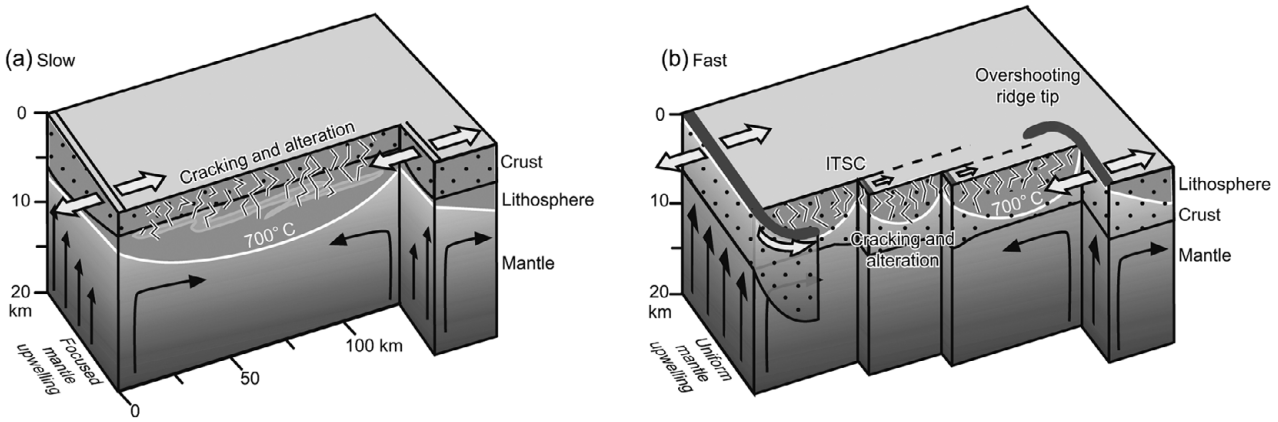

Figure 1.5 Models of oceanic crust accretion, fracturation, and serpentinization at ridge transform intersections together with structural architecture of ridge transform faults (Gregg et al., 2007). White arrow – spreading vector, black arrow – mantle flow trajectory, gray – lithosphere defined by the basal temperature of 700°C, dotted pattern – crust, wiggly black-white lines – zone of fractured lithosphere, light grey polygons – rock volumes affected by serpentinization. (a) Model of the slow spreading ridge, characterized by mantle upwelling focused at spreading ridge segment centers. This results in thinner oceanic crust at segment ends and transforms. (b) Model of the fast spreading ridge, characterized by relatively homogeneous mantle upwelling. The magma-rich character of ridge segments even at their ends is the likely cause of the overshooting ridges and dyke emplacement into the neighboring portion of the transform. Note crustal thickness variations along the transform caused by the crustal accretion at all individual intra-transform ridges. Reprinted by permission from Springer Nature: *Nature Letters*. Gregg, P. M., Lin, J., Behn, M. D. and Montesi, L. G. J. Spreading rate dependence of gravity anomalies along oceanic transform faults. *Nature Letters*, 448, 12, 183–187. ©2007.

https://doi.org/10.1017/9781108686631.002

direction. The reason for its anomalous architecture is that it links an ultra-slow but hotspot-affected Kolbeinsey Ridge, with a spreading rate of 15.8 mmy^{-1} (Pálmason, 1973; DeMets et al., 1994), with the strongly hotspot-affected North Iceland rift zone, rifting at an average rate of about 20 mmy^{-1}, where a single fissure swarm, such as the Krafla swarm, can episodically reach an extension rate of 60 mmy^{-1} (Árnadóttir et al., 2008). Due to the hotspot influence, the linked spreading centers are magma-rich, which results in a potential for overshooting ridges. One example is the Manareyjar Ridge (Figure 8.4), which occurs inside the Tjörnes Transform zone, between its two major internal strike-slip faults. Being connected to the Theistareykir fissure swarm of the Northern Iceland rift zone, it does not follow the strike of the transform zone but is located at a high angle to the boundary strike-slip faults. Its location is most likely affected by the normal faults and sinistral strike-slip faults bounding the crustal blocks moving by a bookshelf mechanism, being bounded by three major dextral strike-slip faults dividing the Tjörnes ridge transform into three parallel internal zones (e.g., Rongvaldsson et al., 1998; Riedel et al., 2001; Stefansson et al., 2008). Volcanic activity along the entire transform zone is indicated by volcanoes located inside pull-apart basins.

The Siqueiros Transform, which offsets the East Pacific Rise, is an example of a fast slipping transform (118 mmy^{-1}) (Figure 1.3). Its structural architecture is markedly different from that characterizing slow slipping transforms (Figure 1.5b). It contains five individual faults separating four intra-transform spreading centers (Fornari et al., 1989), analogous to other fast transforms (Menard, 1967; Menard and Atwater, 1969; Searle, 1983; Fox and Gallo, 1984; Gregg et al., 2006). The intersections of its bounding faults with neighboring spreading ridge segments contain overshooting ridge tips typical for magma-rich fast spreading systems (Fornari et al., 1989; Figure 1.5b). The curved geometry of ridges can be interpreted as a result of either local perturbation of the stress field at ridge transform intersections or preferential dyke propagation along the pre-existing transform-related fracture systems (Gregg et al., 2007). Fresh basalt samples and spreading-related magnetic anomalies at this transform and several others in the East Pacific region, such as the Quebrada, Discovery, Gofar, and Garrett Transforms, indicate active accretion taking place at intra-transform spreading centers (Fornari et al., 1989; Carbotte and Macdonald, 1990; Hekinian et al., 1992, 1995; Perfit et al., 1996; Nagle et al., 2007). With regard to estimated depth extent of the serpentinization along fast slipping transforms, the calculated 500°C isotherm, which represents the upper limit of serpentine stability (Ulmer and Trommsdorff, 1995), does not reach down to mantle depths and remains within the crust (Gregg et al., 2007).

There has been much debate about the influence of pre-breakup continental fault zones on post-breakup ridge transform faults. Some studies interpret the ridge transform faults as being predisposed by the locations of the pre-existing continental zones of weakness (e.g., Wilson, 1965; Mascle, 1976; Wright, 1976; Sibuet and Mascle, 1978; Rosendahl, 1987; Bellahsen et al., 2013; Gibson et al., 2013). Our experience with long transforms that underwent an oceanic–continental stage of development, such as the Zenith–Wallaby–Perth (Figures 3.2d–e), Romanche (Figures 2.6a–b, 2.10b, 2.17, 3.5c, and 4.9), St Paul (Figures 2.6a–b, 2.10b, 3.5c, and 4.9), and Coromandal (Figures 2.12a, 6.9a–b, and 6.15) transforms, indicates that they went through the interaction of Andersonian (see Anderson, 1951) or modified Andersonian faulting on their continental side with non-Andersonian faulting on their oceanic side. This interaction must, to some extent, have controlled the propagation trend of the ridge transform segment located immediately outside of the most external continental–oceanic segment.

Other studies interpret ridge transform fault propagation as unaffected by pre-existing anisotropy (e.g., Taylor et al., 2009; Basile, 2015). They document that the initial spreading offsets are often of a non-transform type, and that transform faults develop either after or during spreading nucleation. Natural examples of this stage are observed in the Woodlark Basin (Taylor et al., 2009). It seems that such a propagation mode can characterize the portion of the post-breakup system, which either contains relatively short oceanic–continental transforms or none at all.

Additional support for transform fault propagation being unaffected by pre-existing anisotropy comes from three-dimensional numerical modeling simulating advanced slow spreading and initial intermediately fast spreading systems (Gerya, 2013a), which suggests that (Figure 1.2d):

1) spreading segments nucleate in an en echelon pattern in overlapping rift units at the start of the initial disorganized spreading stage;
2) subsequently, still during the disorganized spreading stage, proto-transforms sometimes nucleate as oblique to a spreading vector rather than parallel to a spreading vector;
3) subsequently, still during the disorganized spreading stage, the initially oblique proto-transforms rotate into ridge-perpendicular position; and

https://doi.org/10.1017/9781108686631.002

4) subsequently, during the organized spreading stage, the spreading vector-parallel transform direction becomes a rule governed by space accommodation during the mature ridge transform spreading that is reached after about the first five million years of spreading.

Further modeling support for spontaneous oceanic transform development comes from Gerya (2016).

The proto-transform rotation is controlled by the long-lasting weakness of proto-transforms (Gerya, 2016). It is the main reason for the continuously maintained kinematic linkage between the two sea-floor spreading ridges. This rotation can be described by the function (Gerya, 2016):

$$\tan\alpha = \tan\alpha_o[1 - v_s(t - t_o)/L], \quad (1\text{-}1)$$

where α is the deviation angle of the proto-transform from the spreading direction, α_o is the initial deviation angle of the proto-transform from the spreading direction, v_s is the spreading rate, t is the time at which the deviation angle is calculated, t_o is the time of the proto-transform nucleation, and L is the spreading center offset. Function 1-1 indicates that the spreading–parallel proto-transform orientation is reached at $t = t_o + L/v_s$.

The aforementioned model indicates that the orthogonal transform spreading center pattern is controlled by the 180° rotational symmetry for open-space occupation for coevally acting accretion and sliding of new plate material (Gerya, 2016). This pattern represents the only steady-state pattern that is thermo-mechanically consistent.

As already indicated, transforms that connect ridges typically develop only in advanced slow and initial intermediately fast spreading systems. Using the same modeling approach as used by Gerya (2010, 2013a), Puthe and Gerya (2014) published modeling results that indicate that spreading center patterns depend on the spreading rate. Based on modeling results, they can be divided into four scenarios (Figure 1.2c):

1) a stable system developing alternating new magmatic and amagmatic plate zones (S1 in Figure 1.2c) in the case of ultra-slow spreading;
2) an asymmetrically spreading system developing transient features – that is, proto-transforms (S2 in Figure 1.2c) – in some cases of slow spreading;
3) a stable orthogonal spreading system (S3 in Figure 1.2c) in the case of some slow and some intermediate spreading; and
4) a stable system developing curved ridges (S4 in Figure 1.2c) in the case of fast and some intermediate spreading.

Oceanic fracture zones in the fully oceanic domain – that is, where they traverse only oceanic crust far away from continents – are essentially unprospective for hydrocarbons. However, where these fractures approach continental margins at acute angles, they can have significant relevance for petroleum. A prime example occurs in offshore Guyana, where the recent spate of oil discoveries in Cretaceous turbidites, including Liza and related fields such as Yellowtail and Payara, appear to have a close relationship with fracture zones. The fields occur where the thick, primarily Cretaceous sedimentary wedge oversteps the Guyana continental margin and drapes several ridges of the oceanic fracture zone. The fields lie where thick continental crust is juxtaposed against normal oceanic crust. Farther outboard, normal oceanic crust is juxtaposed with the zone of prominent ridges and troughs representing the oceanic fracture zone. The fields also seem to coincide with areas where the transforms are "leaky" and associated with volcanism. The association between fracture zones, volcanism, and stacked hydrocarbon plays is interesting and merits further research. It is plausible that, in this area, turbidite sands were deposited by the small changes in gradient created by the fracture zones. Compaction over buried ridges associated with fracture zones also nucleated later normal faulting in the sediments, which may have aided vertical migration. Further discussion of this field complex may be found in Chapter 15.

1.3.2 Transforms Evolving from the Continental Transform Stage, Through the Oceanic–Continental Transform Stage, into the Transform Margin Stage

This type of transform represents a fault zone along which different plates, microplates – or at least portions of plates with different accretion age – are passing each other horizontally (Figure 1.6a). Some of them can be exceptionally long and active for a distinctly long time period. Their interesting feature is that they evolve from continental transforms into transforms separating different types of lithosphere.

The kinematic development of such a transform, which helps to break up the continent and subsequently accommodates the lateral clearance of the drifting-away daughter continents, may consist of three stages (e.g. Mascle and Blarez, 1987; Figure 1.6a):

1) active continental stage;
2) active continental–oceanic stage; and
3) passive margin stage.

The time spans and the termination of individual stages vary along the strike of the transform margin. The

https://doi.org/10.1017/9781108686631.002

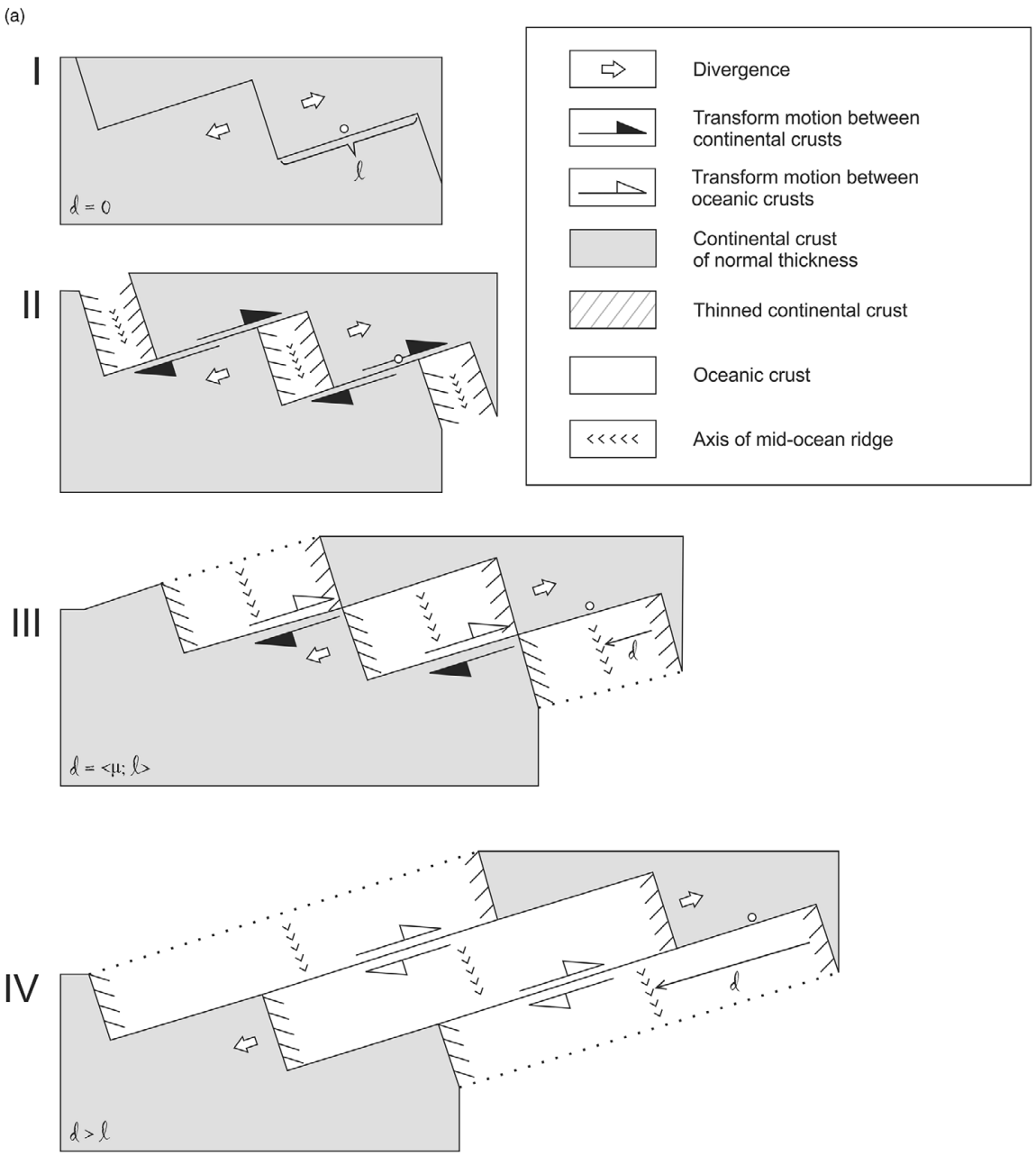

Figure 1.6 (a) Sketch of the strike-slip fault zone with pull-apart terrains evolving into the ocean (Nemčok et al., 2016a). A checkpoint is indicated by a small circle. Stages: I, rifting of continental lithosphere and the checkpoint situated at the dextral transform fault. II, the checkpoint still adjacent to continental lithosphere but a landward portion of the future transform margin adjacent progressively to normal continental crust, then thinned continental crust and then oceanic crust. III, the checkpoint adjacent to the spreading ridge. IV, the checkpoint adjacent to oceanic crust and an inactive transform fault. d is the distance traveled by the spreading center and l is the total length of the transform. $d = \mu/2 + t$, where μ is the half spreading rate and t is the time length of ridge traveling.

termination of the continental stage in a specific area of the future transform margin depends on the time required for the adjacent continent to clear this area and for the juxtaposition of this area to laterally clearing oceanic crust (Figure 1.6a). The passive margin stage begins in specific area once the spreading center clears this area.

Examples of transforms that evolved from the continental stage to passive margin stage include those of the African Equatorial Atlantic (Figure 1.6b) and West

https://doi.org/10.1017/9781108686631.002

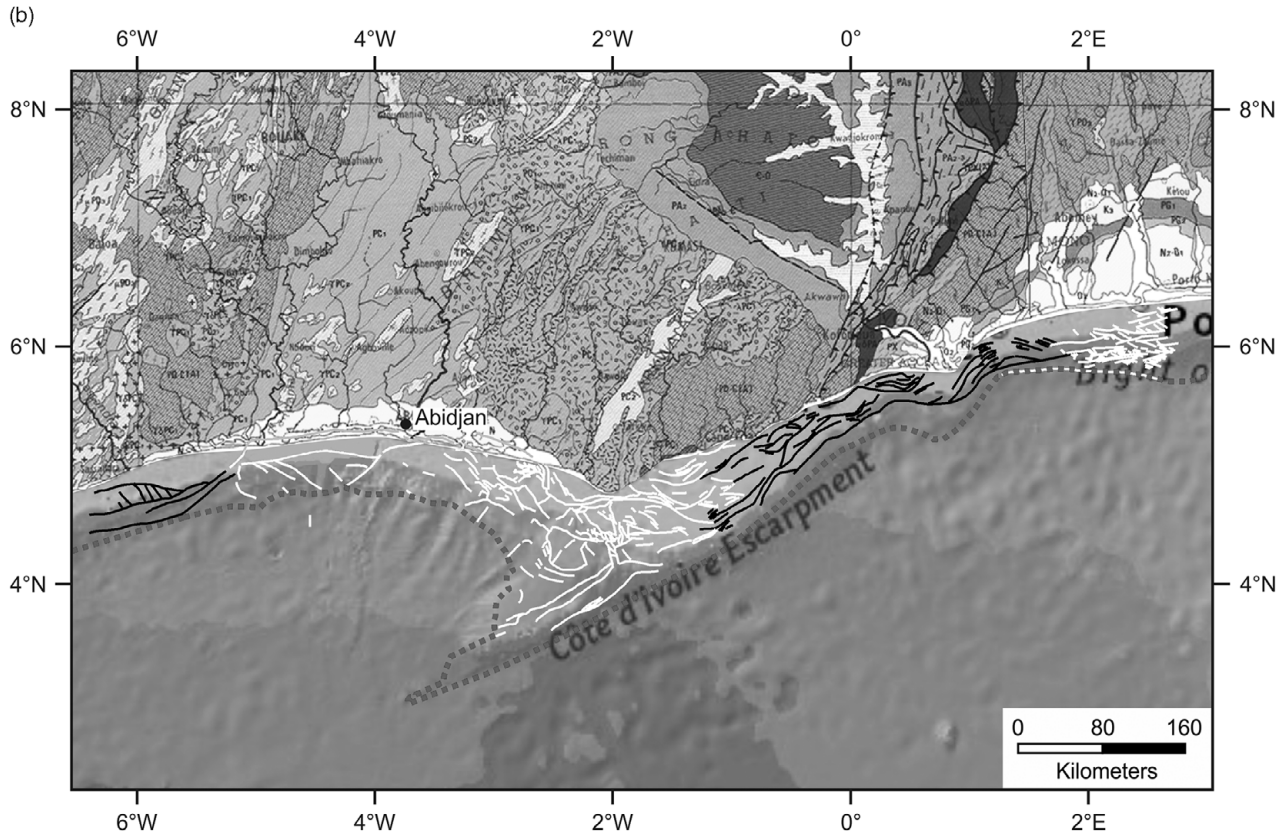

Figure 1.6 (b) Structural architecture of the Romanche Transform margin of the Ivory Coast, Ghana, and Togo, which evolved from the continental transform stage and the subsequent ocean–continent stage into the transform margin development stage (modified from CGMW, 1990; Antobreh et al., 2009; Nemčok et al., 2012a, 2016b). Republished with permission of Elsevier from Rift-shear architecture and tectonic development of the Ghana margin deduced from multichannel seismic reflection and potential field data. Antobreh, A. A., Faleide, J. I., Tsikalas, F. and Planke, S. *Marine and Petroleum Geology*, 26, 345–368. ©2009. Permission conveyed through Copyright Clearance Center, Inc. International Geological Map of Africa at scale 1:5 M, 3rd edition (1985–1990). Coordination: G. Choubert and A. Faure-Muret, cartographic synthesis: P. Chanteux, copyright: CGMW-UNESCO, Paris, 1990.

Australian margins. The largest transforms of these two example margins, and most other large transform margins worldwide, provide evidence that continental transforms that evolved into continent–ocean transform faults were affected by pre-existing continental zones of weakness (Nemčok et al., 2021a). Such evidence comes from either transforms dividing segments of the ocean with different accretion time spans, or transforms dividing different plates and microplates. Some of these bound large marginal plateaus with breakup ages different from those of neighboring margin segments (e.g., Demerara, Guinea, and Exmouth plateaus; Marinho et al., 1988; Stagg et al., 2004; Nemčok et al., 2015a). Some of them link orthogonal margins with different ages of breakup (e.g., Davie, Romanche, Coromandal, Gettysburg–Tarfaya and Cobequid–Chedabucto–Gibraltar Transforms; Nemčok et al., 2005a, 2012a; Schettino and Turco, 2009; Sinha et al., 2016).

Evidence on the post-breakup kinematic adjustments of large continental–oceanic transforms (Nemčok et al., 2021a) indicates that these faults can undergo different kinematic regimes through time.

Hydrocarbon discoveries in this setting are found, for example, on the African side of the Equatorial Atlantic, although not all of them are commercial fields (Figure 1.6c). Some fields occur in pull-apart margin segments located between two transform margin segments. Typical examples are the Akasa, Banda, Belier, Eland, Enyenra, Gazelle, Ibex, Jubilee, Kudu, Makore, Ntomme, Odum, Okure, Orca, Sankofa, Seme, Teak, Tweneboa, and Wava fields in offshore Benin, Ghana, and Ivory Coast. Other fields come from the transform margin segments, such as the Acajou, Baobab, Espoir,

https://doi.org/10.1017/9781108686631.002

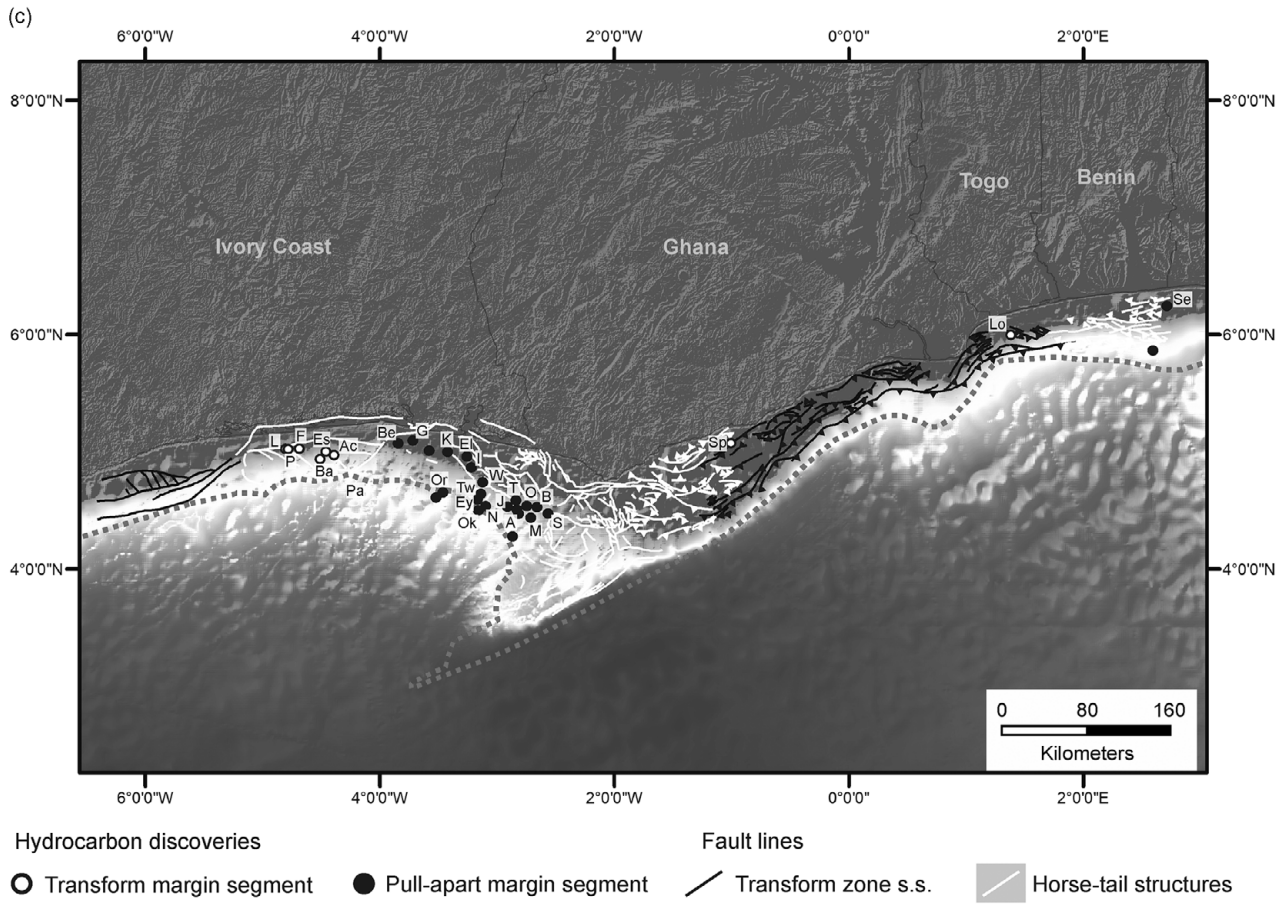

Figure 1.6 (c) Fault map from Figure 1.6(b) together with hydrocarbon field locations. Hydrocarbon discoveries: A – Almond, Ac – Acajou, B – Beech, Ba – Baobab, Be – Belier, El – Eland, Es – Espoir, Ey – Enyenra, F – Foxtrot, G – Gazelle, J – Jubilee, I – Ibex, K – Kudu, L – Lion, Lo – Lome, M – Mahogany, N – Ntome, O – Odum, Ok – Okure, Or – Orca, P – Panthere, Pa – Paon, S – Sankofa, Se – Seme, Sp – Saltpond, T – Tano, Tw – Tweneboa, W – Wawa. Background topography and bathymetry maps are from GEBCO (2019). Republished with permission of Elsevier from Rift-shear architecture and tectonic development of the Ghana margin deduced from multichannel seismic reflection and potential field data. Antobreh, A. A., Faleide, J. I., Tsikalas, F. and Planke, S. *Marine and Petroleum Geology*, 26, 345–368. ©2009. Permission conveyed through Copyright Clearance Center, Inc. International Geological Map of Africa at scale 1:5 M, 3rd edition (1985–1990). Coordination: G. Choubert and A. Faure-Muret, cartographic synthesis: P. Chanteux, copyright: CGMW-UNESCO, Paris, 1990.

Foxtrot, Lion, Lome, Panthere, Paon, Saltpond fields in offshore Ghana, Ivory Coast, and Togo.

1.3.3 Transforms Linking Ridge with Convergent Plate Boundary

The best-known example of a transform that links a ridge with a convergent plate boundary and deforms mostly continental lithosphere is the San Andreas Fault (Figures 1.7a–b). The fault is located between the Mendocino triple junction and the East Pacific Rise spreading system of the Gulf of California (Elders, 1979; Elders et al., 1972; Elders and Sass, 1988; Figure 1.7a). Its structural architecture is complex. It contains segments with different deformation regimes, including locked segments, aseismically creeping segments, and transitional segments between the aforementioned two end members.

The Carrizo Plain in central California is an example of a locked segment. It experiences a transpressive regime and, therefore, has some associated thrust faults. The last rupture of this section was the M7.9, 1857 Fort Tejon earthquake. Limited micro-seismicity has been recorded since the advent of modern instrumentation (Hill et al., 1990). Although it does not represent the total depth extent of brittle fracturing along this fault

https://doi.org/10.1017/9781108686631.002

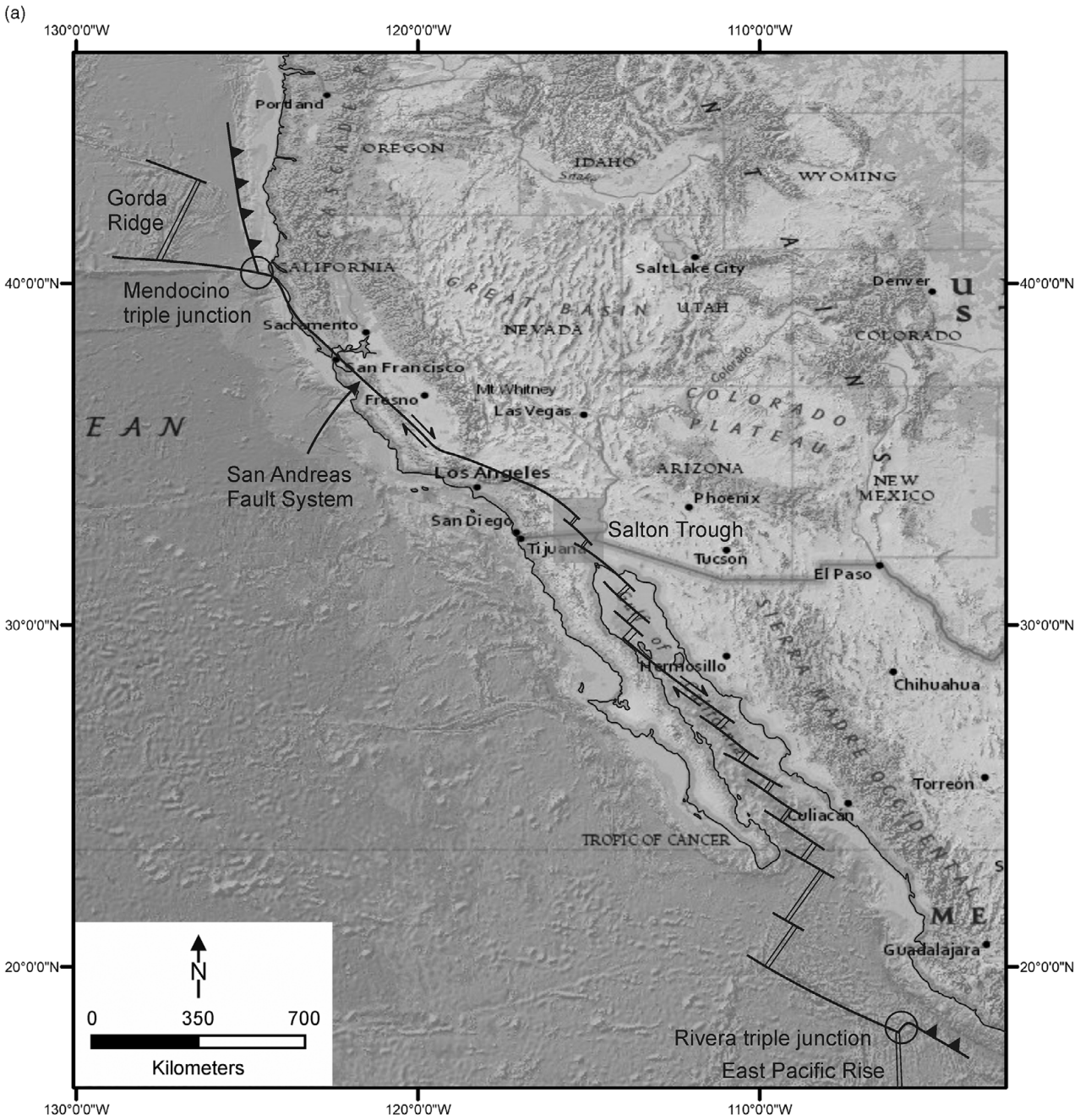

Figure 1.7 (a) Simplified map of the San Andreas Transform linking the system of spreading centers in the Gulf of California with the subduction zone to the north of the Mendocino triple junction (Elders et al., 1972; Elders, 1979; Elders and Sass, 1988). Reprinted with permission from John Wiley and Sons. Elders, W. A. and Sass, J. H. 1988, The Salton Sea Scientific Drilling Project: *Journal of Geophysical Research, B, Solid Earth and Planets*, v. 93, no. 11, p. 12953–12968.

segment, magnetotelluric imaging allows one to interpret a 4–5 km depth extent of the increased fracture porosity zone (Unsworth et al., 1999; Figure 8.7).

A creeping segment example is seen in the area near Hollister, California, where the fault creeps aseismically at a rate of about 10–15 mmy^{-1} (Burford and Harsh, 1980; Evans et al., 1981). A combination of seismic velocity distribution and magnetotelluric imaging allows one to interpret a 10 km depth of the increased fracture porosity zone (Thurber et al., 1997; Bedrosian et al., 2004; Figures 8.8 and 8.9). Synthetic fault zone trapped waves allow estimation of the width of the

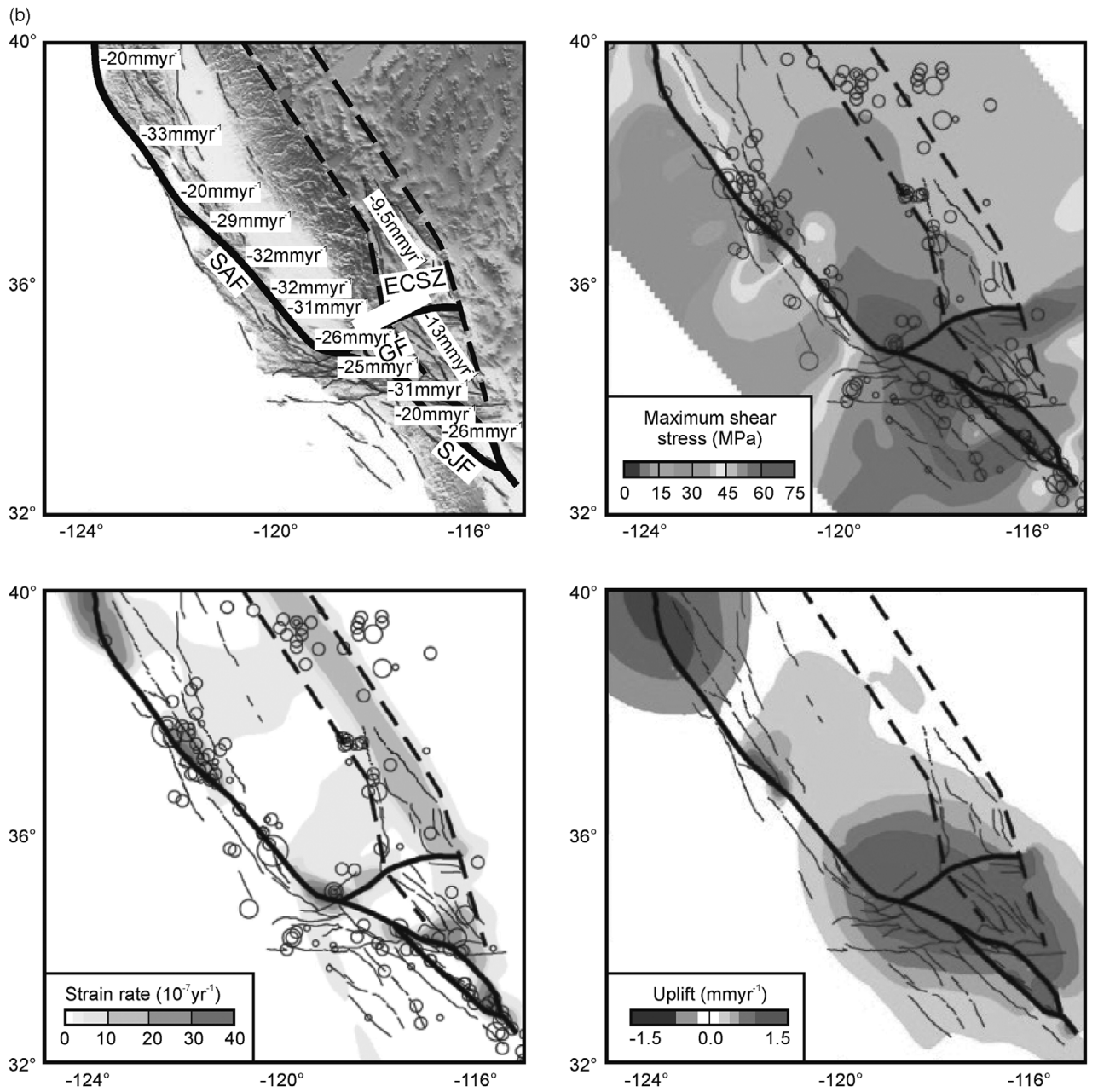

Figure 1.7 (b) Present-day characteristics of the San Andreas Transform (Gerya, 2016). Abbreviations: ECSZ – Eastern California Shear Zone, GF – Garlock Fault, SAF – San Andreas Fault, SJF – San Jacinto Fault. (a) Predicted slip rates. (b) Predicted maximum shear stress. (c) Predicted plastic strain rate outside the GF, SAF, and SJF. (d) Predicted uplift rate. Circles document seismicity. Reprinted with permission from John Wiley and Sons. Gerya, T. 2016. Origin, evolution, seismicity, and models of oceanic and continental transform boundaries. In: Duarte, J. C. and Schellart, W. (Eds), *Plate Boundaries and natural hazards. Geophysical Monograph*, 219, pp. 39–76.

shallow portion of this San Andreas segment to be about 120 m (Li et al., 1997). However, the entire zone of increased fracture porosity indicated by magnetotelluric data is about 7 km wide. It occurs between the San Andreas and Calaveras Faults (Bedrosian et al., 2002, 2004; Figure 8.8).

A transitional segment is observed in the Parkfield area in California, located between the aforementioned

locked and creeping segments. This section of the San Andreas Fault experiences moderate earthquakes of about M6 about every 22 years, and extensive microearthquake activity at about 3 km depth (Bakun and Lindh, 1985). Magnetotelluric imaging combined with seismic velocity distribution allows one to interpret a 4–5 km depth extent of the increased fracture porosity zone (Unsworth and Bedrosian, 2004; Figure 8.10). This zone is about 600 m wide on the surface.

Continental transforms can be associated with important hydrocarbon reserves (Harding, 1974, 1990; Christie-Blick and Biddle, 1985; Harding et al., 1985; Lowell, 1985). The San Andreas Transform provides a series of examples. For example, a system of anticlines in its southern San Joaquin Basin hosts a number of fields (Wilcox et al., 1973; Harding, 1976; Namson and Davis, 1988; Medwedeff, 1989, 1992; Hardy et al., 1996; Mueller and Suppe, 1997; Figure 1.7c). Another prolific region, the Los Angeles Basin, is located further south. It can be roughly described as an irregular Late Miocene–Early Pleistocene pull-apart basin that underwent an important compressional event, responsible for hydrocarbon trapping in anticlines and faulted anticlines (Yerkes et al., 1965; Biddle, 1991).

1.3.4 Transforms Linking Convergent Plate Boundaries

An example illustrating this transform type is the dextral transform fault zone forming the southern boundary of the Caribbean Plate (Figure 1.8a). In fact, the characteristic portion of this zone is only its extent to the east of Puerto Cabelo in Venezuela – that is, the portion that contains the San Sebastian Fault, El Pilar Fault, and other strike-slip faults further east toward the Barbados accretionary prism, all with more-or-less

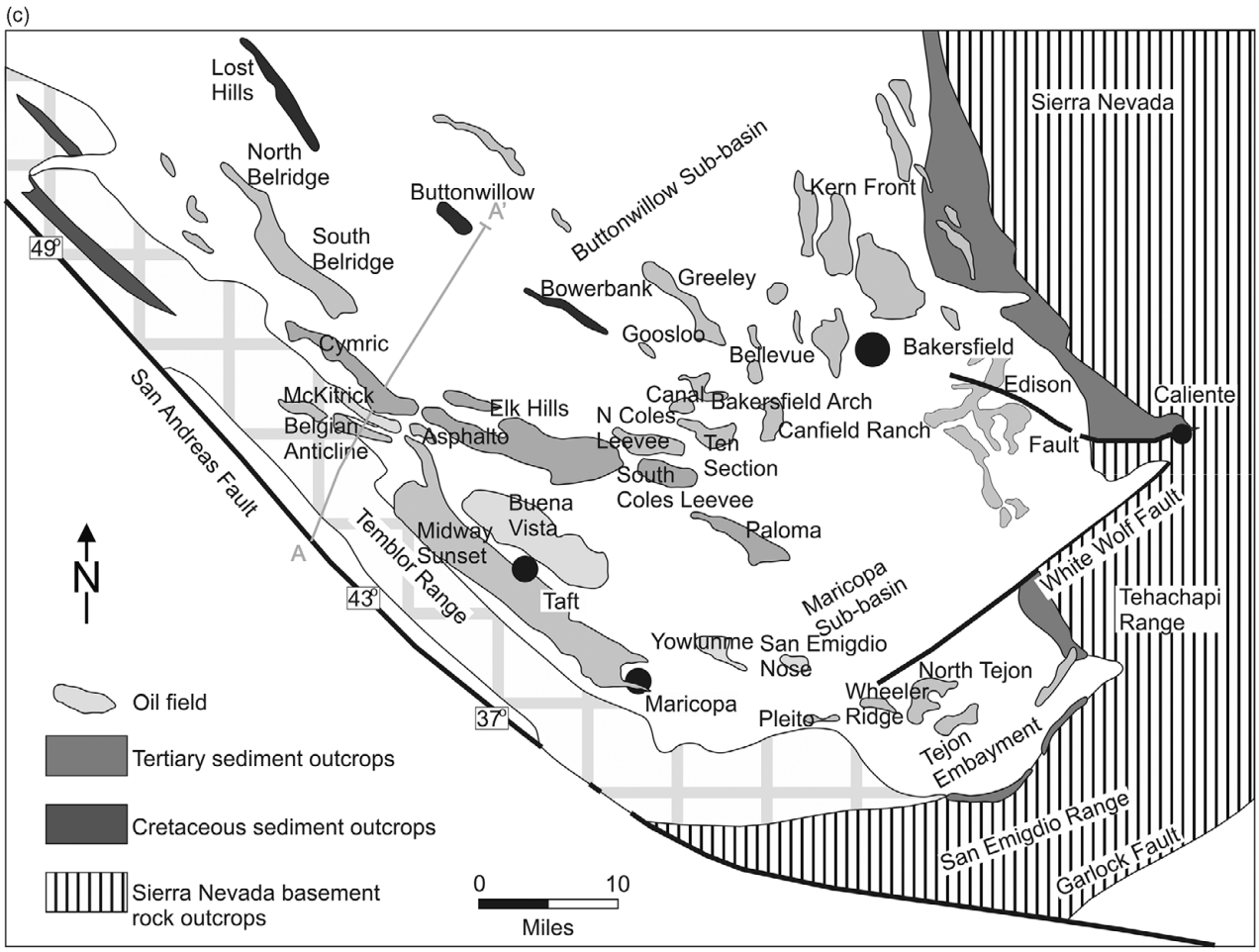

Figure 1.7 (c) San Andreas Fault together with hydrocarbon fields hosted by its anticlines in the southern San Joaquin Basin (modified from Namson and Davis, 1988). Modified from Namson, J. S. and Davis, T. L. 1988. Seismically active fold and thrust belt in the San Joaquin Valley, central California. *Geological Society of America Bulletin*, 100, 257–273.

https://doi.org/10.1017/9781108686631.002

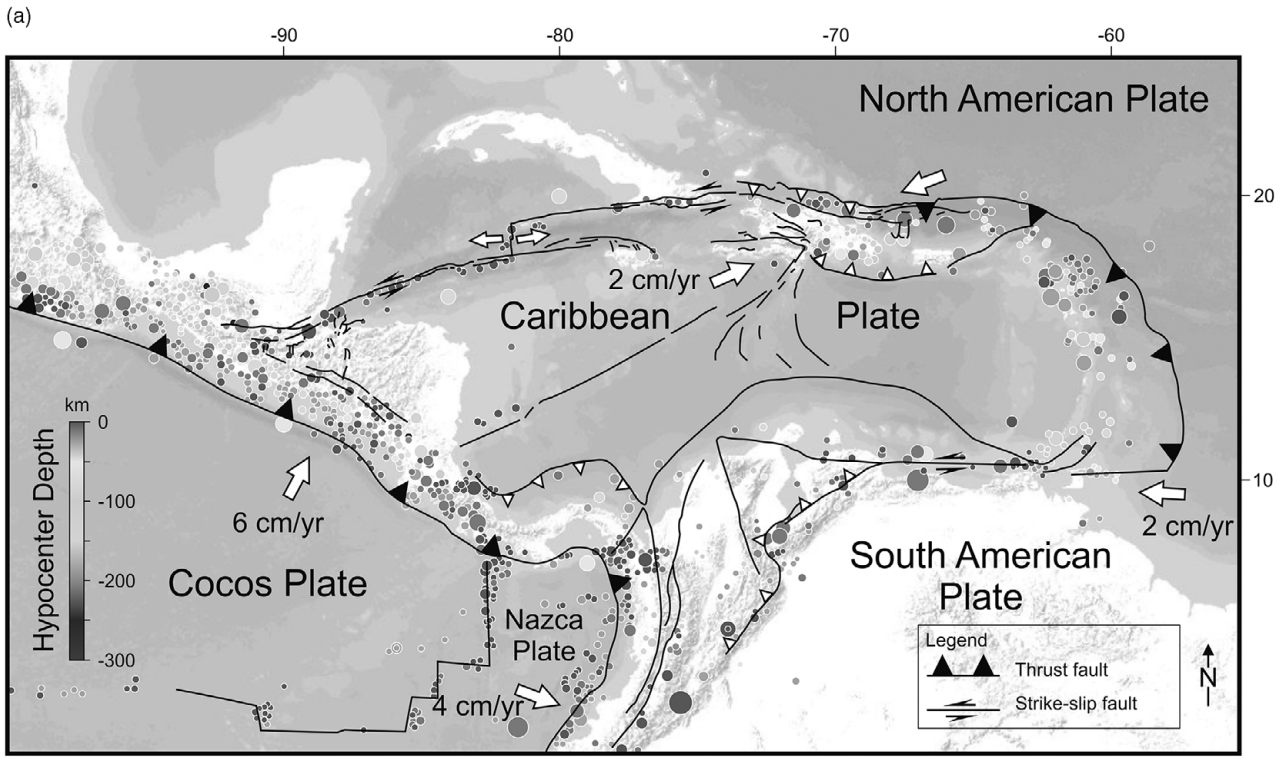

Figure 1.8 (a) Seismotectonic map of the Caribbean Plate (Calais, 2018).

E–W strikes. This is because the western, North Andean portion of this transform fault zone bends around the westward-moving South American Plate, and, as a result, gained transpressional character.

The North Andean dextral transpression is a result of the interaction of five different plates (Cortés and Angelier, 2005; Figure 1.8a). The Cocos Plate moves northeastward at a rate of 71 mmy^{-1}. The Nazca Plate near Colombia, central Peru, and northern Chile moves eastward, east–northeastward, and east–northeastward at rates of 54, 22, and 32 mmy^{-1}, respectively. Bayona (2011, pers. com.) also characterizes the Colombian segment of the Nazca Plate by the east–northeastward movement. On the contrary, the North American Plate moves to the west–southwest. The South American Plate moves to the west and represents an important resistance against the eastward advance of the North Andean retro-wedge. Its movement rates are 47 and 48 mmy^{-1} in central Peru and northern Chile, respectively (Moretti, 2011, pers. com.). This westward movement is associated with an intra-Middle Miocene increase in Mid-Atlantic Ridge sea-floor spreading rate (Cobbold, 2011, pers. com.). The increased rate controls a large-scale buckling recognized in platform areas of the South American Plate, which is under horizontal loading (Moretti, 2011, pers. com.).

The aforementioned eastern portion of the transform zone is rather wide and composed of numerous dextral strike-slip faults and their associated fault families (e.g., Audemard et al., 2005; Figure 1.8b).

1.3.5 Trench-Linked Strike-Slip Faults

Trench-linked strike-slip faults form yet another group of strike-slip faults that cut through the entire lithosphere (Figure 1.1), and result from oblique subduction or accommodate changes in subduction direction. They represent fault zones parallel to the trench (Sylvester, 1988) and located:

1) inside the magmatic arc, such as the Sumatran Fault (McCaffrey et al., 2000; Figure 1.9) and the Philippine Fault (Barrier et al., 1991); or
2) inside the fore-arc, such as the Hawkey Ridge Fault in the Aleutians (Scholl, 1999), faults of the southern Ryukyu arc (Lallemand and Chemenda, 1999), and the Atacama Fault in Chile (McCaffrey, 1996); or
3) along the boundary between the fore-arc and hinterland plates, such as the South Japan Sea Fault Zone (Itoh et al., 2002).

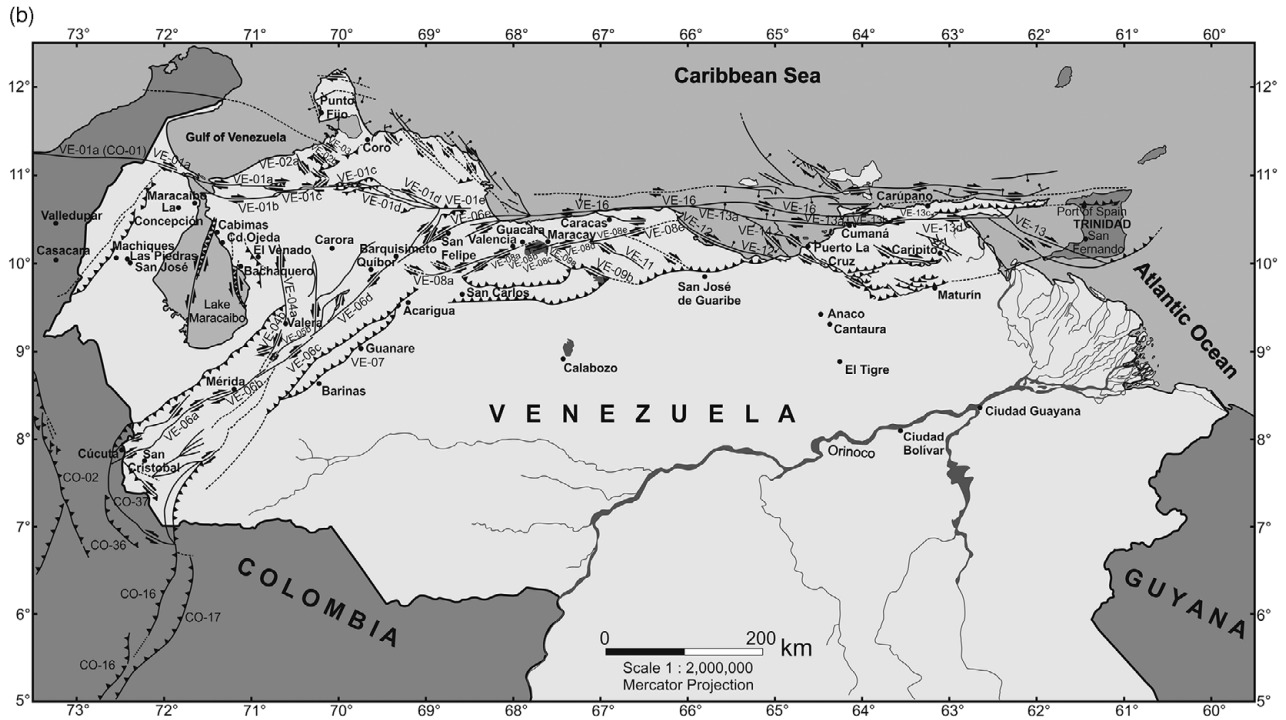

Figure 1.8 (b) Map of the Quaternary faults of the Venezuelan portion of the deformation zone representing the boundary between the Caribbean and South American Plates (Audemard et al., 2005). Colombian faults: 2 – Santa Marta-Bucaramanga, 16 – Guaicaramo Thrust, 17 – Cusiana-Yopal thrust system, 36 – Soata, 37 – Cobugon. Venezuelan faults: 1 – Oca-Ancon, 2 – Lagarto, 3 – Urumaco, 4 – Rio Seco, 5 – Matapalo, 6 – Western Paraguana, 7 – Cumaraguas, 8 – Cabo San Rona-Puerto Escondido, 9 – Adicora, 11 – Taima-Taima/Chuchure, 12 – Carrizal, 13 – El Hatilo, 14 – La Soledad, 16 – Araurima.

Reprinted from *Earth-Science Reviews*, 69, Audemard, F. A., Romero, G., Rendon, H. and Cano, V. Ramprasad. Quaternary fault kinematics and stress tensors along the southern Caribbean from fault-slip data and focal mechanism solutions, 181–233. ©2005, with permission from Elsevier.

Trench-linked strike-slip faults can accumulate displacements of several hundred kilometers, accommodating portions of the deformation of the overriding plate behind the trench (Woodcock, 1986). These faults are commonly short-lived features. Similarly to the previous transform category, they frequently reactivate pre-existing faults and become subsequently reactivated by other tectonic events.

For example, the recently active dextral South Japan Sea Fault Zone is associated with oblique Quaternary subduction of the Philippine Sea Plate under the Eurasian Plate (Itoh et al., 2002). It reactivated a lithospheric weak zone, the development history of which started with Early Miocene back-arc rifting at the southern margin of the Japan Sea (Otofuji et al., 1985; Tamaki et al., 1992) and continued with Late Miocene–Early Pliocene inversion (Itoh and Nagasaki, 1996).

In the case of the Atacama Fault, the earliest, Jurassic–Early Cretaceous, deformation was a system of both dip and sinistral strike-slip ductile shear zones in the magmatic arc, developing under amphibolite metamorphic conditions (Mpodozis and Ramos, 1990; Scheuber and Andriessen, 1990; Brown et al., 1993). These conditions developed in a transtensional trench-linked fault zone (Reutter et al., 1991).

This deformation was overprinted by brittle sinistral strike-slip faulting of the trench-linked strike-slip fault zone, which was located oceanward of the magmatic arc because this arc has migrated eastward since the Jurassic–Early Cretaceous (Arabasz, 1971; Brown et al., 1993). The fault zone was subsequently reactivated by late Oligocene–Early Miocene contraction (Olson, 1989) and the Quaternary extension (Arabasz, 1971; Naranjo, 1987; Gonzáles et al., 2006).

The development of trench-linked strike-slip faults is related to strain partitioning from obliquely converging plates. Their kinematics are determined from systematic studies of earthquake slip vectors (Fitch, 1972; Jarrad, 1986), GPS-derived displacement vectors (Bock et al., 1990; McCaffrey et al., 1990), plate convergence vectors estimated from poles of rotation, paleostresses calculated from outcrop fault-striae data (Nemčok, 1993; Gayer

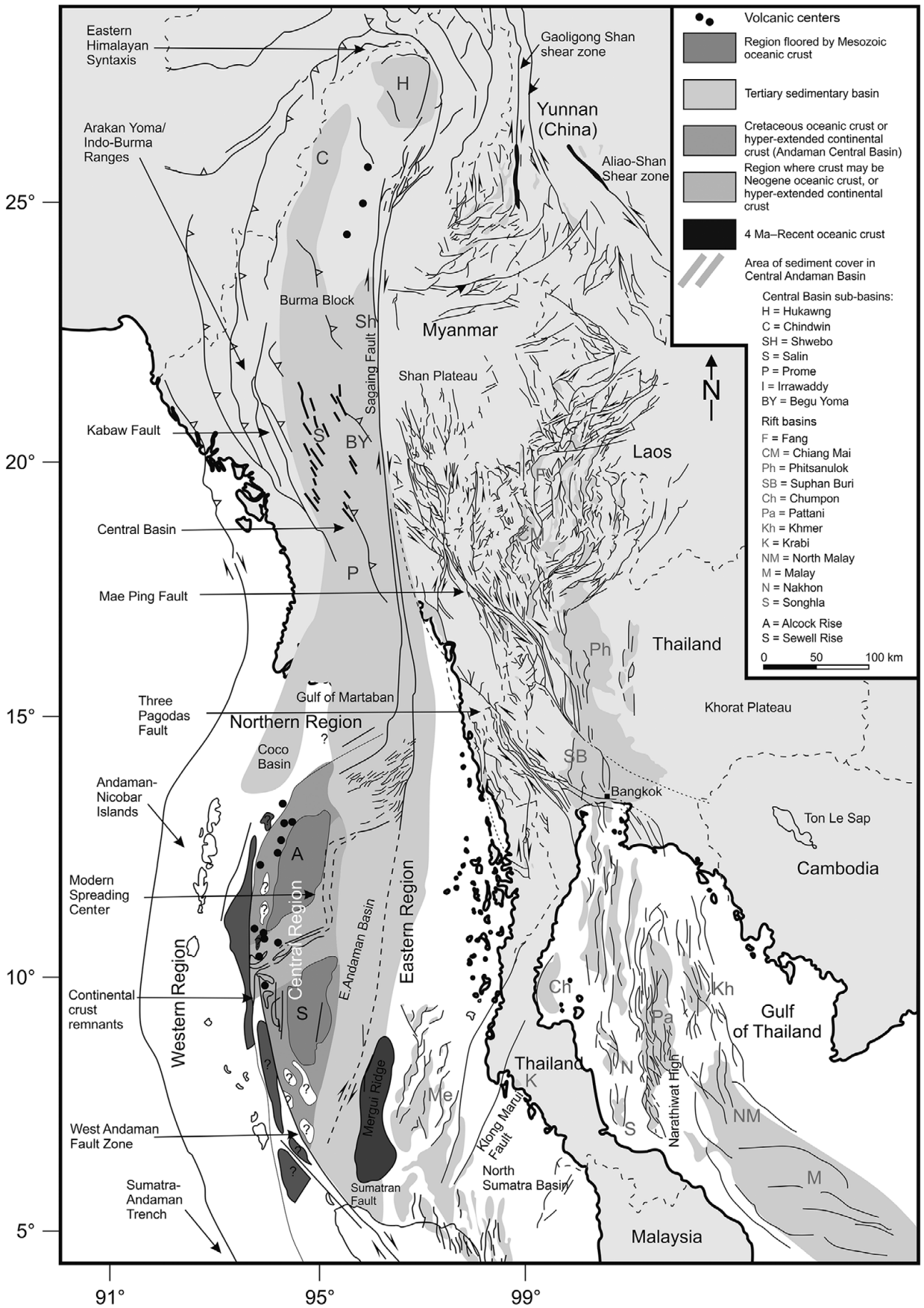

Figure 1.9 Tectonic map of the Andaman Sea region showing the Sagaing Transform linking the Eastern Himalayan syntaxis of the India–Eurasia collisional zone with spreading centers of the Central Region of the Andaman Sea (Morley, 2015).

https://doi.org/10.1017/9781108686631.002

et al., 1998), and finite-element modeling (McCaffrey et al., 2000). They are primarily controlled by the stress distribution along the interface between upper and lower plates (McCaffrey et al., 2000). Considering the upper plate as being sufficiently heterogeneous to approach a material continuum, the most typical location for trench-linked strike-slip faults should be the upper plate above the down-dip boundary of the largest interplate stress. When such a system evolves, it should develop multiple strike-slip faults further oceanward (McCaffrey et al., 2000). Secondary localization controls of trench-linked strike-slip faults include weak crustal and mantle zones related to the magmatic arc, and suitably oriented pre-existing weak deformation zones (McCaffrey et al., 2000; Itoh et al., 2002).

In the case of strongly arcuate convergent systems, such as the Carpathians advancing onto the European Platform, in which the subduction vector changed from SW-, to WSW-, to W-directed (e.g., Nemčok et al., 1998a), trench-linked strike-slip faults change their location inside the overall complex fault pattern in relatively short time intervals (Figure 1.10).

Examples of hydrocarbon fields in this transform setting are found in the Central Sumatran Basin (Williams and Eubank, 1995), including the Balam, Beruk, Damar, Duri, Hitam, Kotabatak, Libo, Lingai, Minas, Pematang, Petapahan, Pungut, Suram, Tandun, Topaz, and Waduk oil and gas fields. They are usually associated with basin-dividing structural highs, and anticlines along their flanks, charged from lacustrine source rocks in surrounding structural lows.

1.4 Intraplate Strike-Slip Faults

1.4.1 Indent- and Lateral Extrusion-Linked Strike-Slip Faults

Indent- and lateral extrusion-linked strike-slip faults (Figure 1.1) are represented by strike-slip faults separating crustal blocks escaping from high to low potential energy conditions. They usually form complex fault arrays. They undergo geometric changes as the escaping block evolves.

Lateral extrusion-related strike-slip fault examples come from the Carpathian–Pannonian region. They were coeval with late Oligocene–Early Miocene large-scale lateral, west-to-east-directed material movement from the Eastern Alps into the remnant Carpathian Flysch Basin (Ratschbacher et al., 1991a, b), which was affected by both extrusion from the west and subduction rollback from the northeast and east (Nemčok et al., 1998a; Sperner et al., 2002).

The Carpathian orogen developed by northeastward and eastward migration of an accretionary wedge in front of the ALCAPA and Tisza–Dacia microplates (Csontos et al., 1992). Extrusion-related faults accommodated separate movements of both microplates and their various internal crustal blocks (Figure 1.10). Their characteristic feature is their constant rearrangements into different regional patterns accompanied by changes of kinematics during the late Oligocene–Early Miocene time interval (Figure 1.10a), and their subsequent rearrangements and reactivation when Carpathian development was progressively dominated by subduction rollback during the Karpatian–Sarmatian time period (Nemčok et al., 2006a; Figure 1.10b). Some of them were active during the Karpatian–Sarmatian time period as trench-parallel strike-slip faults. As the subduction kept changing into collision from west to east along the arc, and accretionary wedge large-scale advance kept ceasing from west to east, earlier strike-slip faults were undergoing reactivation as normal faults (Figures 1.10c–d).

Indented by the bend between the Eastern and Southern Carpathians, the Carpathian foreland underwent late Sarmatian–Meotian sinistral strike-slip (Figure 1.11), accompanied by subordinate thrusting (Matenco et al., 2003). Its development was relatively short-lived because the subduction–collision transition there was accompanied by subducting oceanic slab breakoff (e.g., Nemčok et al., 1998a).

Former pull-apart basins located on both sides of the ALCAPA microplate, the Vienna and Danube Basins along its northwestern side, and Drava and Sava Basins along its southeastern side (e.g., Nemčok et al., 1998a), serve as examples of hydrocarbon-hosting basins in this type of strike-slip setting (e.g., Szalay and Koncz, 1993; Pogácsás et al., 1994; INA, 2000a, b; Tari and Horváth, 2006). Because the pull-apart basins were short-lived features, subsequently disrupted by normal faulting (Nemčok et al., 2006a), their source rocks reside in both syn- and post-pull-apart strata, and both are known to charge syn- and post-pull-apart reservoir rocks, as documented in the Danube Basin. Most typical fields, such as Beničanci, Mosti, and Šandrovac fields in the Drava Basin, and Dugo Selo, Jamarica, Mramor Brdo, Stružec, Žutica fields of the Sava Basin are hosted by faulted blocks, faulted anticlines, and anticlines.

Further examples of lateral extrusion-related faults must have been initial stages of the development of the Northern and Eastern Anatolian faults that were needed for the separation of the westward escaping Anatolian wedge from the rest of the collisional zone developing between Eurasia and the Arabian indenter. Here, one can see the interplay of both tectonic escape of crustal blocks from the collisional site to its lateral margins (e.g., Molnar and Tapponier, 1975) and

https://doi.org/10.1017/9781108686631.002

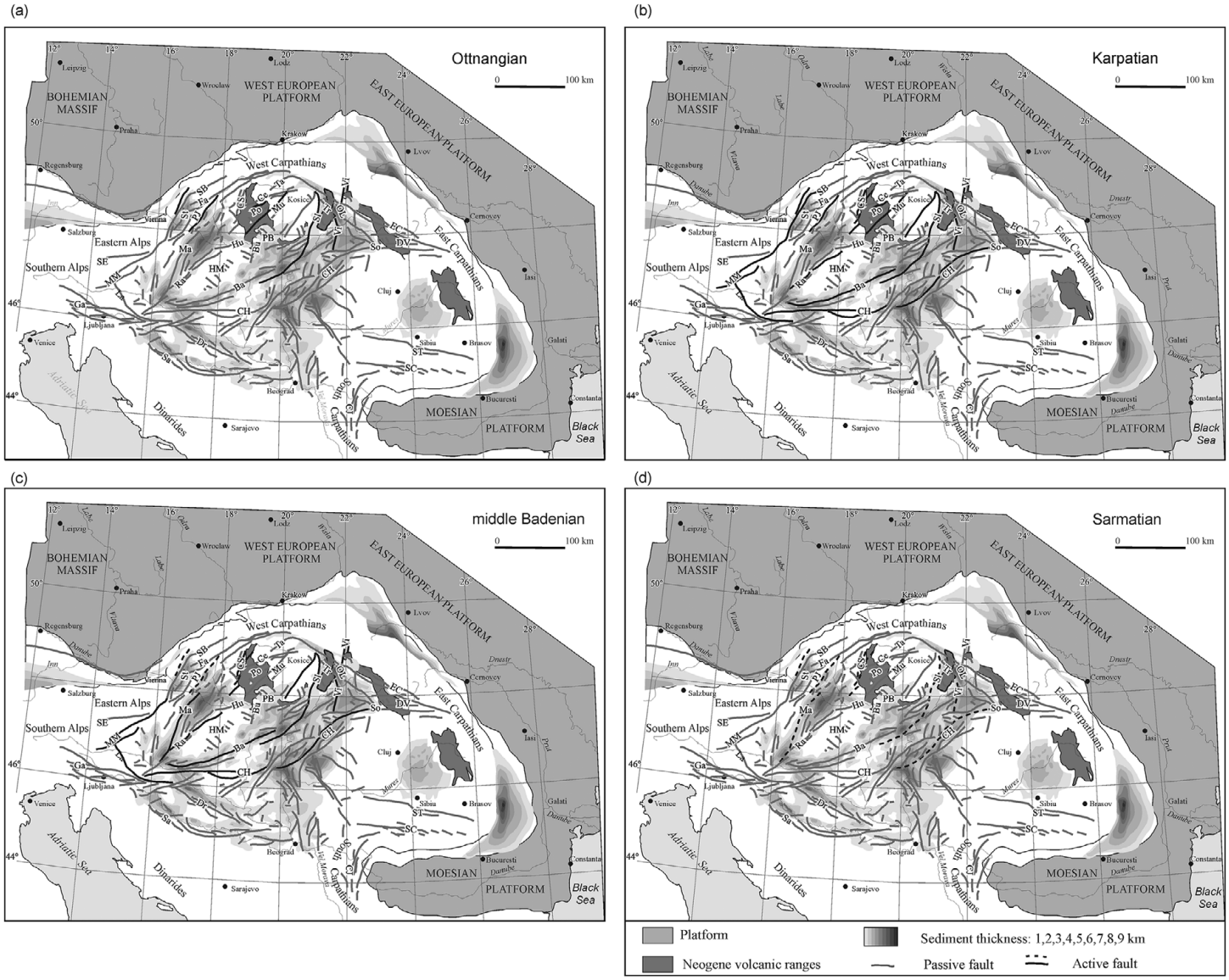

Figure 1.10 Fault kinematics and timing in the ALCAPA microplate of the Carpathians for (a) Ottnangian, (b) Karpatian, (c) middle Badenian, and (d) Sarmatian (Nemčok et al., 2006a). Thick black solid lines indicate main strike-slip faults, and thick black dashed lines indicate main normal faults active during their respective period. Ba – Balaton Fault Zone, Bu – Buda Fault Zone, Ce – Čertovica Fault Zone, CH – Central Hungarian Fault Zone, CJ – Cerna–Jiu Fault, CS – Central Slovakian Fault System, Da – Darnó Fault Zone, Dr – Drava Fault Zone, DV – Dragos–Voda Faults, EC – fault contact of External and Internal Flysch in the Eastern Carpathians, Ga – Gailtal Fault, HM – fault zones of the Central Hungarian Mountains, Hu – Hurbanovo Fault, La – Lavanttal Fault Zone, Ma – Malé Karpaty marginal faults, MM – Mur–Murz Fault Zone, Mu – Muráň Fault, OL – Ondava–Laborec Fault System, PB – faults of both Matra Mountains and north of the Pannonian Basin, PJ – Pottendorf–Jablonica Fault Zone, Po – Pohorelá Fault, Ra – Rába Fault Zone, Sa – Sava Fault Zone, SB – Schrattenberg–Bulhary Fault Zone, SC – Southern Carpathian Fault, SE – Salzachtal–Ennstal–Mariazell–Puchberg Fault System, Sl – Slánske Vrchy Fault System, So – Somes Fault, St – Steinberg Fault, Fa – Farské Fault Zone, ST – South Transylvanian Fault, Ta – Tatry Fault, Tr – Trebišov Fault System, Vi – Vihorlat Fault Zone.

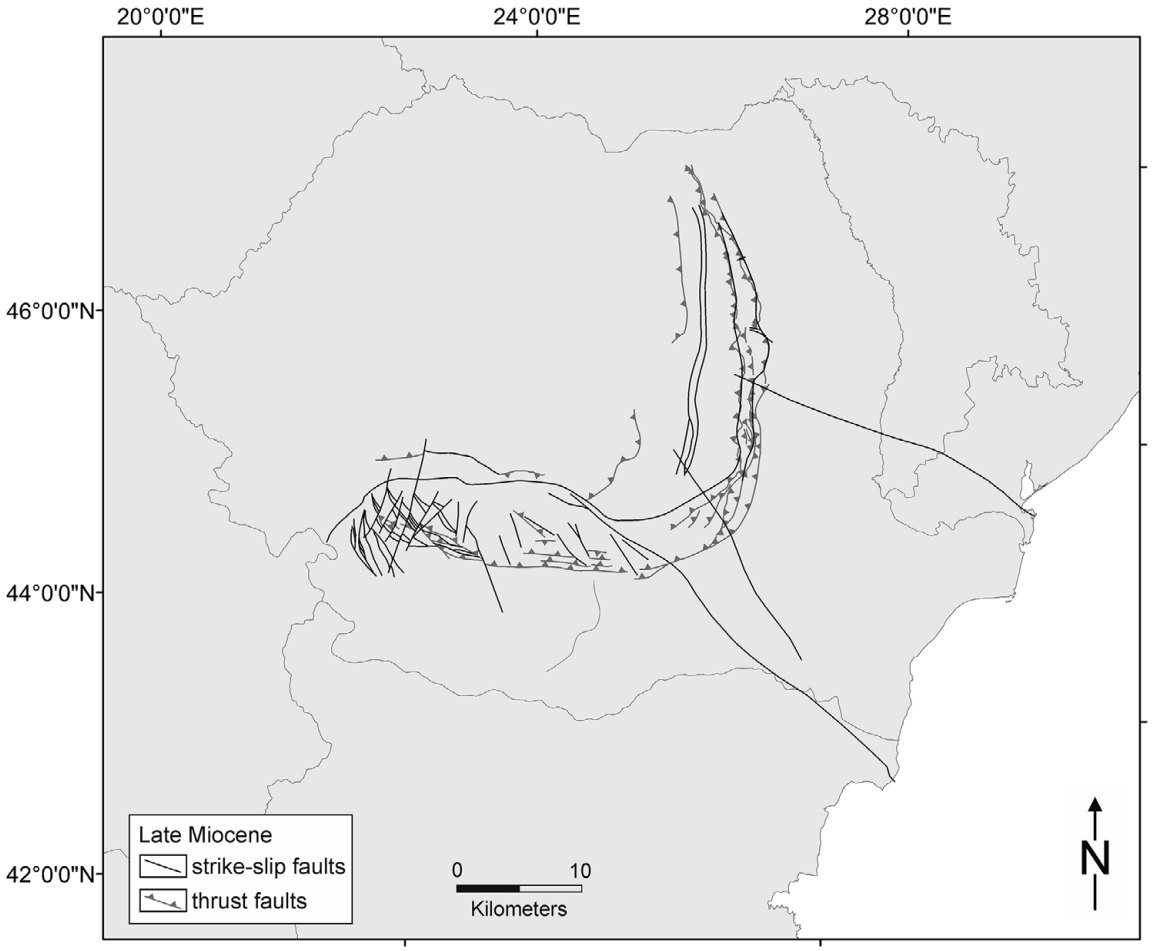

Figure 1.11 Late Miocene faults of the Carpathian orogen and its indented foreland (modified from Matenco et al., 2003). Reprinted from *Sedimentary Geology*, 156, Matenco, L., Bertotti, G., Cloetingh S., and Dinu, C. Subsidence analysis and tectonic evolution of the external Carpathian–Moesian Platform region during Neogene times 71–94. ©2003, with permission from Elsevier.

extensional collapse, which causes thickened, topographically elevated, and, thus, gravitationally unstable continental crust to flow toward lower levels (e.g., England and Houseman, 1988).

The North and East Anatolian Faults do not qualify as intraplate faults in their present-day stage. Despite the gravity collapse of the overthickened collisional zone between Eurasia and the Arabian indenter representing a significant component of their controlling dynamics, they are both interpreted to be transforms. While the North Anatolian Fault represents a northern boundary of the escaping Anatolian Block, separating it from Eurasia, the East Anatolian Fault represents a segment of the boundary between Eurasia and Arabia (Figure 1.12).

The Northern and Eastern Anatolian Faults accommodated the switch from the north-northwestward thrusting to the westward lateral escape of the Anatolian wedge (McKenzie, 1972; Şengör and Yılmaz, 1981; Dewey et al., 1986). Timings for the escape quoted in the literature include Late Miocene (i.e. Sarmatian, 12–13 Ma) (Dewey and Şengör, 1979; Şengör et al., 1985; Hempton, 1987; Le Pichon et al., 1995), Early Pliocene (5 Ma) (Tatar, 1975; Barka and Hancock, 1984; Barka and Kadinsky-Cade, 1988; Koçyiğit, 1989; Barka, 1992; Westaway, 1994) and Late Pliocene (2.5 Ma) (Şaroğlu, 1988). Our interpretation of the last thrusting at the Pontides front in the Black Sea (see also evidence for Late Miocene sediments sealing the frontal thrusts in Kaymakci et al. (2010)), and analysis of timing constraints from the literature, points toward escape in the Sarmatian.

In the middle Neogene, portions of the northern and southern orogenic systems located to the east of the Black Sea were approaching each other, until their fronts met in Georgia and the collisional zone between Eurasia and

https://doi.org/10.1017/9781108686631.002

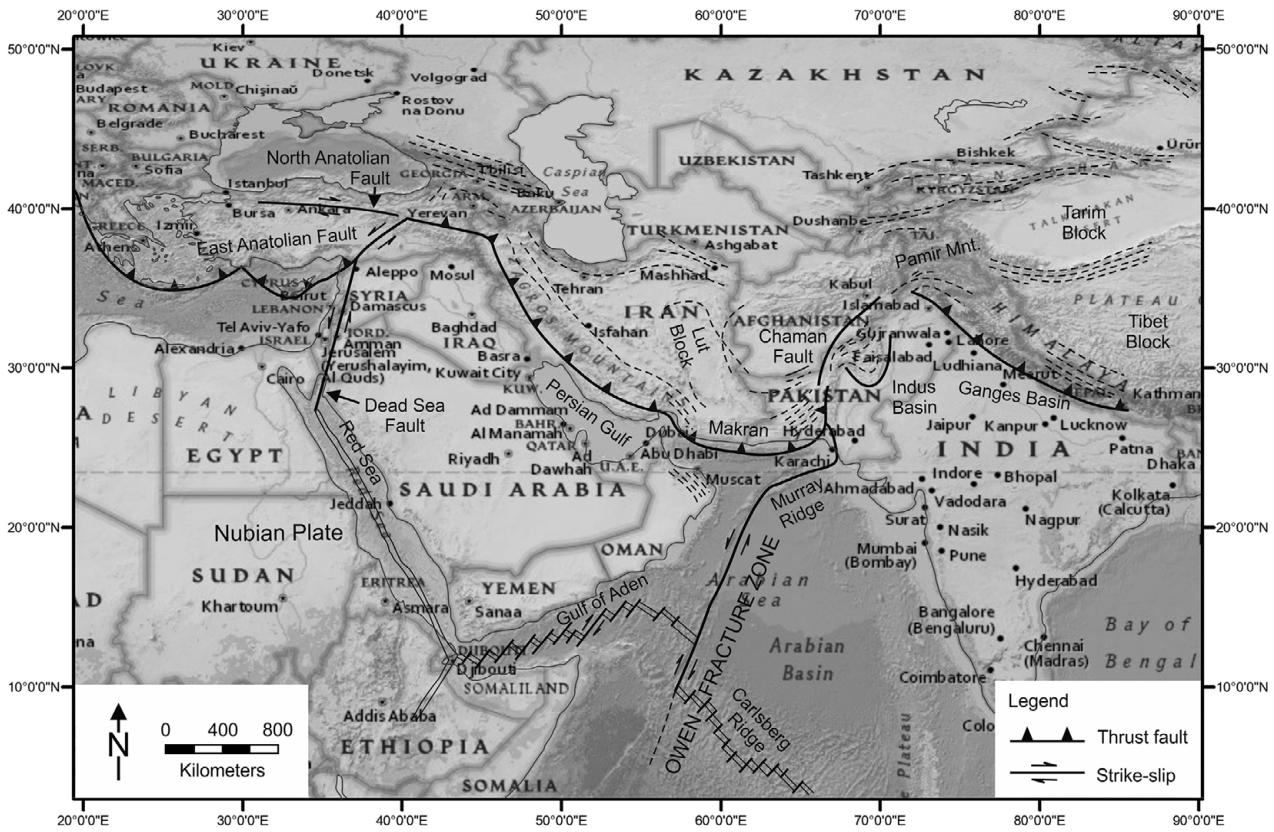

Figure 1.12 The Chaman Transform fault linking the overridden plate of the collision zone with the overriding plate of the subduction zone, North Anatolian Fault representing a boundary between Anatolia and Eurasia, and East Anatolian Fault representing the boundary between Anatolia and Arabia (modified from Khan et al., 2009).

Arabia progressively developed a considerably thickened continental crust. The Middle and Late Miocene fault activity maps (Nemčok et al., 2009) indicate that the crust in the future Anatolian region must have been overthickened because it started to undergo extension. The extension first appeared in the easternmost portion of the future Anatolian wedge during the Middle Miocene (Figure 1.13a). It was accommodated by the NNE–SSW striking system of normal faults. The nucleation and development of these faults progressively extended toward the west until they deformed the whole present-day Anatolian region, their strikes varying aerially between NE–SW, NNE–SSW, and NW–SE (Figure 1.13b). During the Late Miocene, the normal faults formed a regional pattern located among the progressively developing strike-slip fault segments of the future Northern and Eastern Anatolian strike-slip zones separating the Anatolian wedge from its surroundings. This "preparation" of the overthickened crust for the lateral escape ended between the Sarmatian and Pliocene.

Strike-slip faults bounding the laterally extruding lithospheric or crustal blocks are typically characterized by a displacement increase from the indentation point to the free interface. The Anatolian wedge serves as a good example. While the GPS-derived horizontal movement components in its eastern portion next to the Arabian indenter are about 18 mmy^{-1}, they are about 40 mmy^{-1} in its western portion moving into the free interface (see Yilmaz, 2011).

The example of the Korudag Anticlinorium in this setting documents how this petroleum-bearing anticlinorium was shaped by multiple tectonic events. Some of them were related to the lateral extrusion-linked fault propagation. The subduction- and collision-related Early Miocene anticlinorium was further modified by the Middle Miocene propagation of the oldest splay of the North Anatolian Fault and Quaternary deformation along the North Anatolian Fault (Sen and Yillar, 2008). Both the anticlinorium and parallel anticlines around it host the Cayirdere, Degirmenkoy, Karacali,

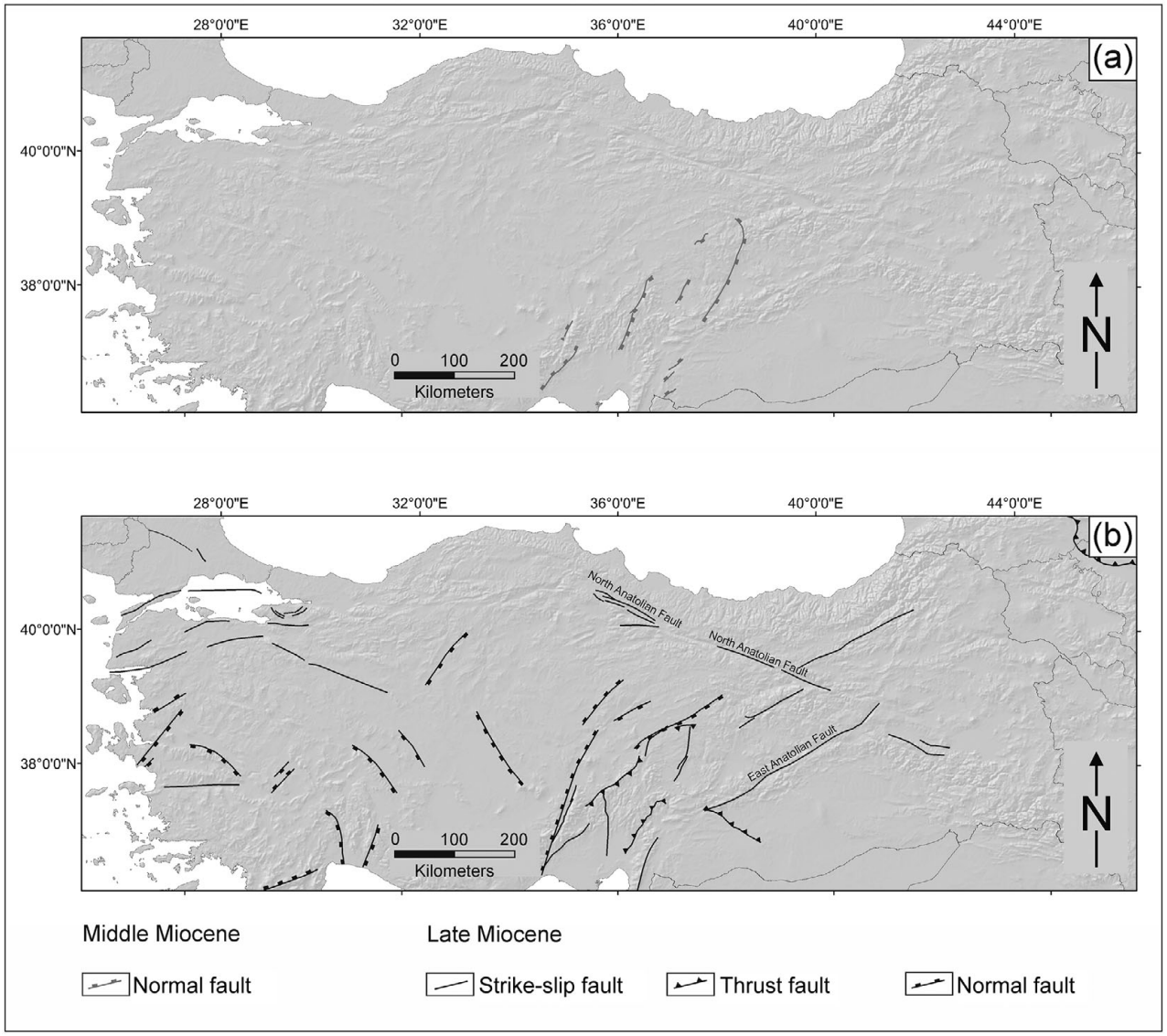

Figure 1.13 Middle Miocene (a) and Late Miocene (b) faults of the future Anatolian wedge region (Nemčok et al., 2009).

North Marmara, Sevindik, Seymen, Terkirdag, Vakiflar, and Yulafli fields.

1.4.2 Transfer Faults

Transfer faults offset extensional, contractional, or strike-slip structures. They have larger extent than tear faults, accommodating the transfer of slip between two neighboring similar structures. Transfer faults are the hard-linked version of more diffuse transfer structures, which include features such as relay ramps, linking transfer faults, en echelon step faulting, tilted fault blocks, and zigzag fault arrays in extensional terrains (Moustafa, 2002).

When residing in an extensional terrain, strike-slip transfer faults provide a hard linkage of rift units of the same or opposite polarity and entire rift zones (Bosworth, 1985). Their role is to accommodate differences in structural styles and strain amounts along the strike of the extensional system or the direction of extension (e.g., Gibbs, 1984; Lister et al., 1986; Bosworth, 1995; McClay and Khalil, 1998). Depending on their geometry with respect to the controlling stress regime, they can be divided into pure

strike-slip, transtensional, and transpressional (Gibbs, 1984; Lister et al., 1986).

The reason these faults have such variable kinematic regimes is that their propagation is frequently affected by pre-existing zones of weakness (Versfelt and Rosendahl, 1989). Examples of such propagation come from the Gulf of Suez–Red Sea rift system (Younes and McClay, 2002; Figure 1.14a). Detailed interpretation of these faults has been performed on outcrops of pre-rift granites and foliated metamorphic rocks around the Darag, October, Zeit, and Duwi half-graben basins.

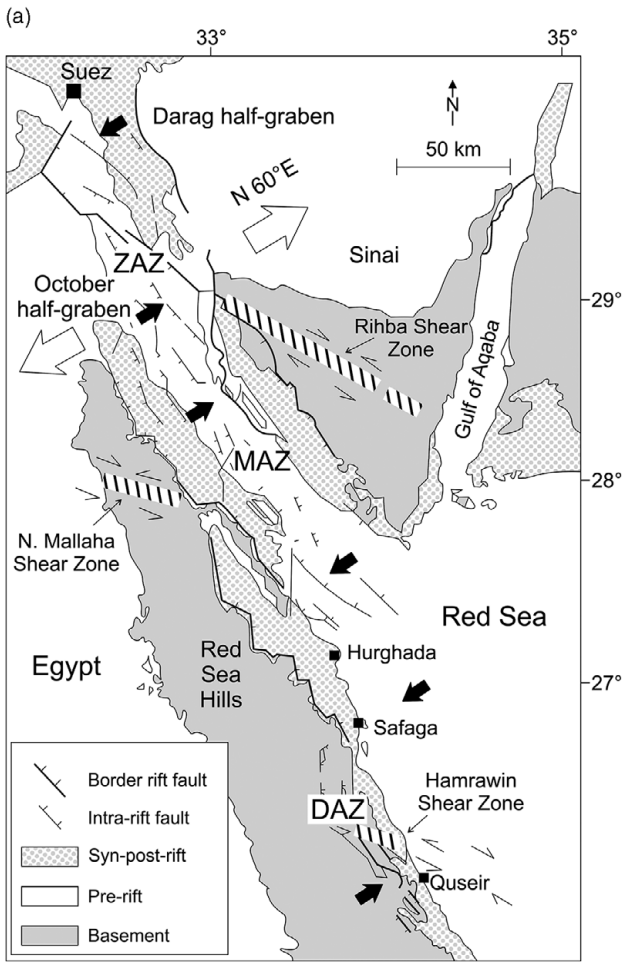

Figure 1.14 (a) Location map of the Darag, October, Zeit, and Duwi half-graben basins of the Gulf of Suez–Red Sea rift system (Younes and McClay, 2002). Black bold arrows indicate dip direction of half-grabens. Large white arrows indicate the direction of late Oligocene–Early Miocene extension. Solid lines are normal faults. Major Precambrian shear zones are shown in stippled lines. AZA – Zaafarana accommodation zone, MAZ – Morgan accommodation zone, DAZ – Duwi accommodation zone.

As rifting in this area evolved, fault patterns propagated from pre-rift rocks to syn-rift sediments. North–south to northwest–southeast striking faults, which were perpendicular to the regional extension, had normal fault displacements (Angelier, 1985; Steckler et al., 1988; Khalil, 1998). Most of them were not affected by the pre-existing anisotropy. Northeast–southwest and WNW–ESE striking faults were characterized by sinistral and dextral oblique-slip displacements (Prat et al., 1986; Chorowicz, 1989; Abu El Karamat and Fouda, 1990). Their development started with reactivation of the weak zones in the basement (Lybéris, 1988; Jarriage et al., 1990; Younes, 1996) prior to or coeval with propagation of the rift-bounding faults, and finished with arrest of the border faults and transfer of displacement (Younes and McClay, 2002). The arrest of the propagating rift-bounding faults is documented by a diagram showing their decreasing throws as they approach the Hamrawin transfer fault from both sides (Younes and McClay, 2002; Figure 1.14b). Both normal faults eventually die out at this fault.

The interaction of propagating rift-bounding faults with propagating transfer faults depends on the geometries and kinematics at their intersection (Younes and McClay, 2002; Figure 1.14c). If their slip components were divergent, tensile stresses at the intersection become magnified, allowing the rift-bounding fault to kink or jog. The kinks have potential to evolve into transfer faults linking the main intersecting faults. If the slip components are convergent, the propagation of the rift-bounding fault either terminates abruptly at the reactivated shear zone or cuts through it.

The Gulf of Suez–Red Sea examples show that transfer faults that reactivated pre-existing weak zones can have various kinematic characters that depend on the relationship of their controlling stress field and geometry of weak zones. However, transpressional transfer faults are relatively rare in nature.

An example of such a fault is the Jeremboabo sinistral transpressional fault in the failed Late Jurassic–Early Cretaceous Jatobá–Tucano–Recôncavo rift zone of northeast Brazil (Destro et al., 2003). The fault is located on the flexural side of the rift zone, where it links smaller rift-bounding faults. Its displacement sense, determined from striated faults in outcrops of Berriasian–Valanginian syn-rift sediments, is consistent with the displacement sense of linked bounding faults on both sides. Its displacement was sinistral oblique, with a strong reverse component. The transfer character of the Jeremboabo Fault is further documented as based on its linkage with the major dextral Caritá transfer fault, located between rift units of the Jatobá–

https://doi.org/10.1017/9781108686631.002

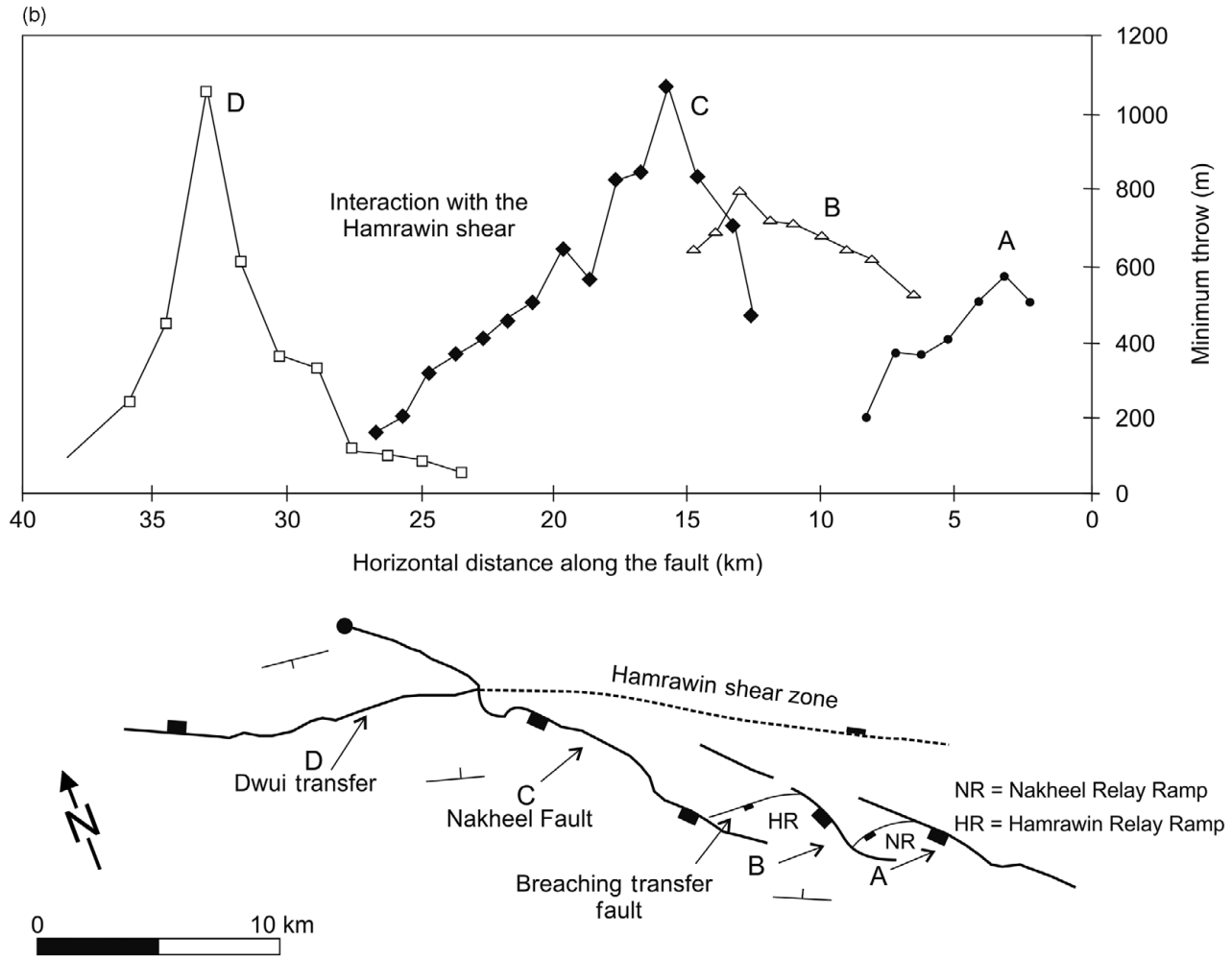

Figure 1.14 (b) Fault displacement profile along the main fault system of the Duwi accommodation zone (Younes and McClay, 2002). The shaded area indicates an overlap area between the Duwi transfer zone and the northernmost tip of the Hamrawin shear zone. Displacement is measured from cross sections, taking into account the thickness variation of pre-rift strata and slope of the top of the basement. Note that these are minimum values, as in most places the pre-rift sedimentary section has been eroded from the footwall.

Tucano–Recôncavo rift zone that have opposite polarity. The reason for its relatively unusual transpressional character is the transfer fault reactivation of the pre-existing zone of weakness.

Transfer faults can be represented by single faults, such as those from the Gulf of Suez–Red Sea rift region (Younes and McClay, 2002) or they can be represented by wide zones of strike-slip faults with pull-apart basins among them, as in those of the Gettysburg–Tarfaya transfer zone on US and Moroccan Central Atlantic margins (Nemčok et al., 2005a and references therein). A further well-documented case is the Garlock Fault in southern California, which functions as a transfer between the extended Basin and Range province in the north and the unextended Mojave Desert area in the south (Sylvester, 1988).

When residing in contractional terrains, strike-slip transfer faults provide a hard linkage of thrust units of the same or opposite polarity, and can bound entire orogenic salients and reentrants. The Potwar Plateau in Pakistan, with its dextral Jhelum and sinistral Kala Bagh strike-slip faults, represents the first example (Figure 1.15a). The primary function of these two faults is to accommodate the south-southeastward advance of the orogenic salient, which is more than 100 km in front of the frontal thrusts of its neighbor thrust belt segments.

The Sulaiman Range in Pakistan is a second example. The range is an orogenic salient, which

https://doi.org/10.1017/9781108686631.002

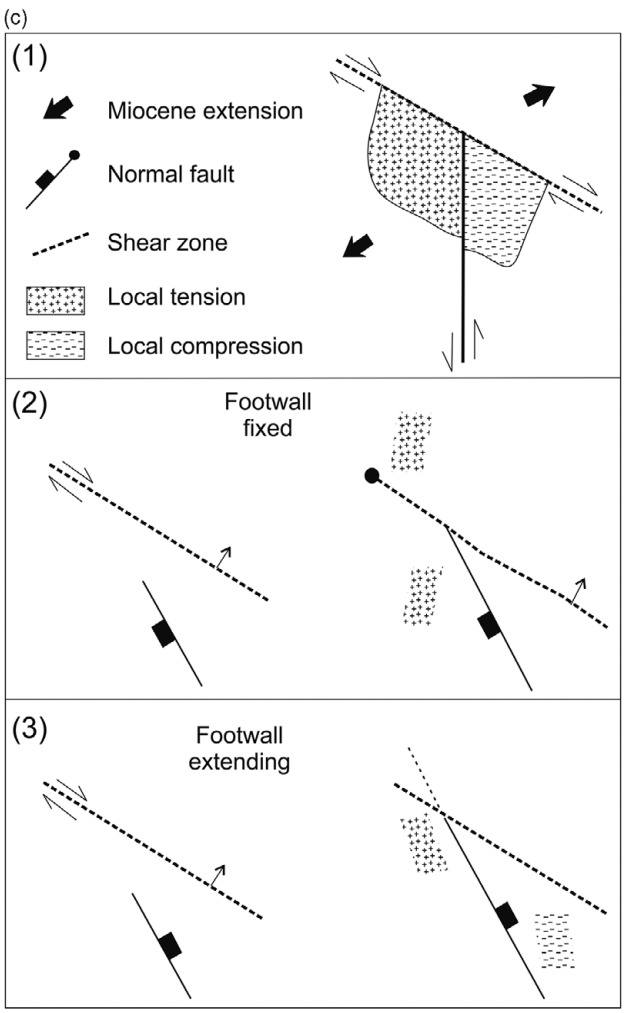

Figure 1.14 (c) Kinematics of the reactivation of pre-existing Precambrian shear zones during late Oligocene–Early Miocene rifting in the Gulf of Suez–Red Sea region (Younes and McClay, 2002). Obtuse angles between rift-bounding faults and reactivated shear zones promote extension, acute ones contraction. See text for explanation.

required a relatively simple dextral strike-slip accommodation along its western side. However, its eastern side is much more complex and wider, represented by an entire system of sinistral strike-slip faults, oblique-slip faults, and thrusts. Various transpressional structures among these faults host a variety of condensate fields (Figure 1.15b). The largest strike-slip fault at the eastern side is the NNE–SSW striking fault that extends from the Savi Ragha field to the south of the Giandari well. Another important fault is the Kingri Fault, which has a NNW–SSE strike. The former separates the Zindapir Folded Zone – represented by gas-producing or oil-and-gas-producing anticlines such as Zindapir, Afiband, Rodho, and Dhodak – from the rest of the Sulaiman thrustbelt. Its southern compressional horsetail structure is formed by a system of splaying-off anticlines, including the Loti and Sui gas fields and the dry Giandari anticline.

Other examples of hydrocarbon fields in this setting come from the northwest–southeast striking diffuse transfer zones that segment the Faroe–Shetland Basin. These zones include the Judd Fault and its smaller analogs. They help to set up some of the Paleocene fields. Farther north in the Barents Sea, a northwest–southeast striking transfer zone, generally considered to be a reactivated offshore extension of the Paleozoic Trollfjord–Komagelv Fault, provides a hard linkage between two different hydrocarbon provinces, the Hammerfest and Nordkapp Basins (e.g., Gabrielsen and Færseth, 1989).

1.4.3 Tear Faults

Tear faults represent the third group of strike-slip faults that are crustal deformational features. They represent relatively small-scale faults accommodating either inhomogeneous shortening or inhomogeneous extension along systems of primary faults and folds (Twiss and Moores, 2007). They are usually steep and parallel to the regional displacement vector.

Good natural examples of this type of fault come from thin-skinned thrust belts, such as the Jacksboro and Russel Fork Faults bordering the Pine Mountain thrust sheet in the Appalachians (Mitra, 1988a), multiple unspecified tear faults in the Jura Mountains (Laubscher, 1972), multiple unspecified tear faults in the frontal thrust sheets of the southwestern British Variscan orogen in South Wales (Figure 1.16a), and multiple unspecified tear faults in the frontal portion of the Western Carpathians (Mahel', 1973).

Tilting is typical of tear faults inside thrust sheets, together with tilting of the thrust sheet they segment. Examples include the sinistral strike-slip fault that segments the Forebalkan Unit of the Eastern Balkans (Figure 1.16b). A similar relationship characterizes tear faults segmenting hanging walls of listric normal faults.

As the hosting thrust sheet or hanging wall becomes inactive, tear faulting stops and these faults can passively rotate together with the sheet or hanging wall, resulting in unusual geometries, especially if the thrust sheet occupies the rear of the accretionary wedge where the thrust sheets passively rotate to vertical and even overturned positions.

Tear faults can have a significant modifying presence on petroleum systems in foreland fold-and-thrust belts. An excellent example of this role is seen in the southern sub-Andean fold-and-thrust of Bolivia (Pereira et al., 2018). Tear faults in this region are shown to act as both

https://doi.org/10.1017/9781108686631.002

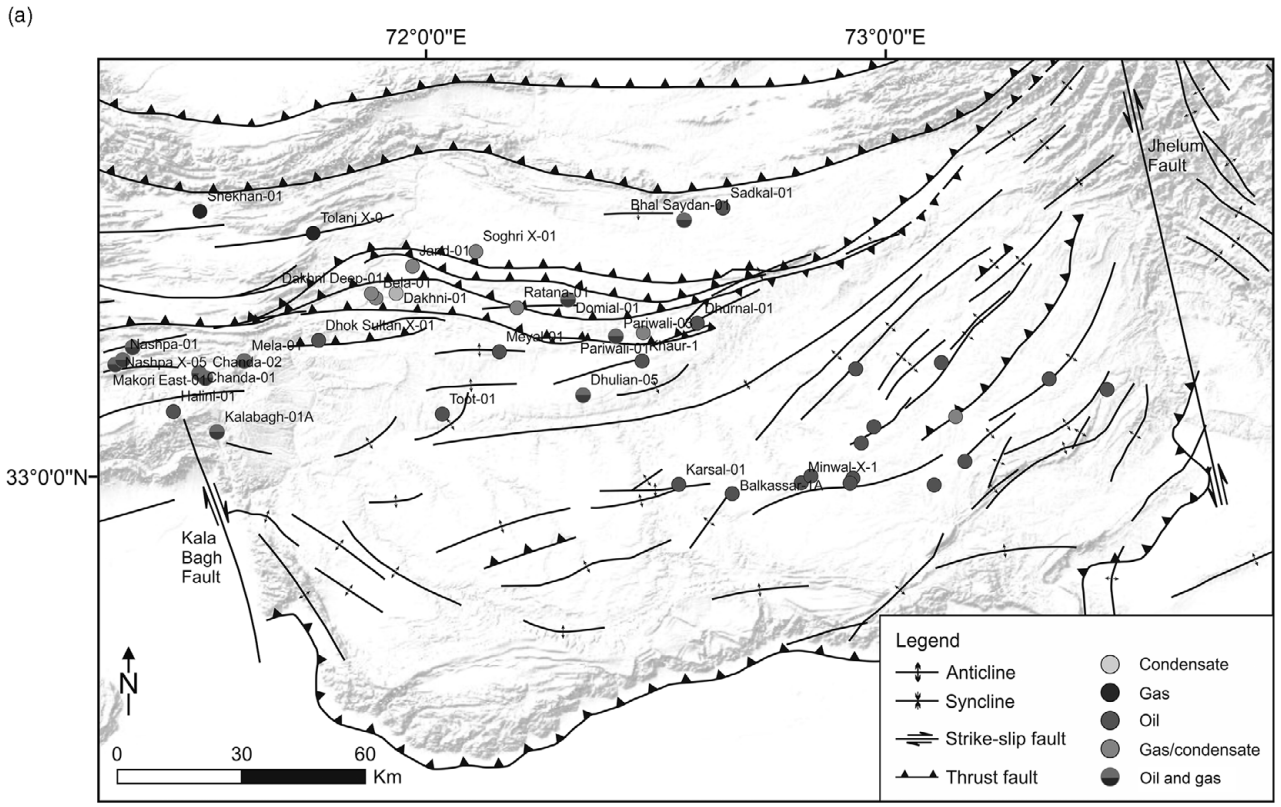

Figure 1.15 (a) Transfer faults bounding the Potwar Plateau, Pakistan (modified from Khan et al., 1986; Quadri and Quadri, 1996; Jaswal et al., 1997; Aamir and Siddiqui, 2006; Moghal et al., 2007). Republished with permission of AAPG from Geology of Petroleum in Kohat-Potwar Depression, Pakistan. Khan, M. A., Ahmed, R., Raza, H., Arif, K. *The American Association of Petroleum Geologists Bulletin*, 70, 396–414. ©1986. Permission conveyed through Copyright Clearance Center, Inc. Republished with permission of AAPG from Structure and Evolution of the Northern Potwar Deformed Zone, Pakistan. Jaswal, T., Lillie, R. and Lawrence, R. *The American Association of Petroleum Geologists*, 70, 396–414. ©1997. Permission conveyed through Copyright Clearance Center, Inc. Republished with permission of the Society of Exploration Geophysicists from Interpretation and visualization of thrust sheets in a triangle zone in eastern Potwar, Pakistan. Aamir, M. and Siddiqui, M. M. *The Leading Edge*, 2206, 24–37. ©2006. Permission conveyed through Copyright Clearance Center, Inc.

barriers and conduits for secondary migration. In some cases, they appear to control remigration of reservoired hydrocarbons from leaky thrust sheets to shallower levels in the Cenozoic succession, as seen for example in the Tajibo gas field, some 15 km west of the thrust-induced Charagua Range. The role of tear faults and other fractures that cut across the thrust belt is particularly interesting at this location, since most of the source rocks in the region reached their critical generation moment before the Andean orogeny, and remigration is, therefore, required to charge the newly developed structures.

1.4.5 Small-Scale Conjugate Strike-Slip Fault Systems in Individual Thrust Sheets

This type of strike-slip fault represents the fourth group of strike-slip faults that are crustal deformational features. Being relatively common in anticlines of thrust belts, they are Andersonian conjugate faults (Anderson, 1951) that accommodate coeval strike-parallel stretching and orthogonal shortening. Examples from the Sulaiman Range in Pakistan are shown in Figure 1.17.

1.5 Structural Architecture of Key Elements of Strike-Slip Terrains and Transforms

1.5.1 Structural Architecture of Strike-Slip Faults

Comparing results of numerous natural case studies and analog material experiments (Cloos, 1928; Riedel, 1929; Hills, 1963; Tchalenko, 1970; Tchalenko and Ambraseys, 1970; Sylvester and Smith, 1976; Harding and Lowell, 1979; Bartlett et al., 1981; Christie-Blick and Biddle, 1985; Naylor et al., 1986), a list can be made of structural elements of strike-slip fault zones (Figure 1.18). It includes the following:

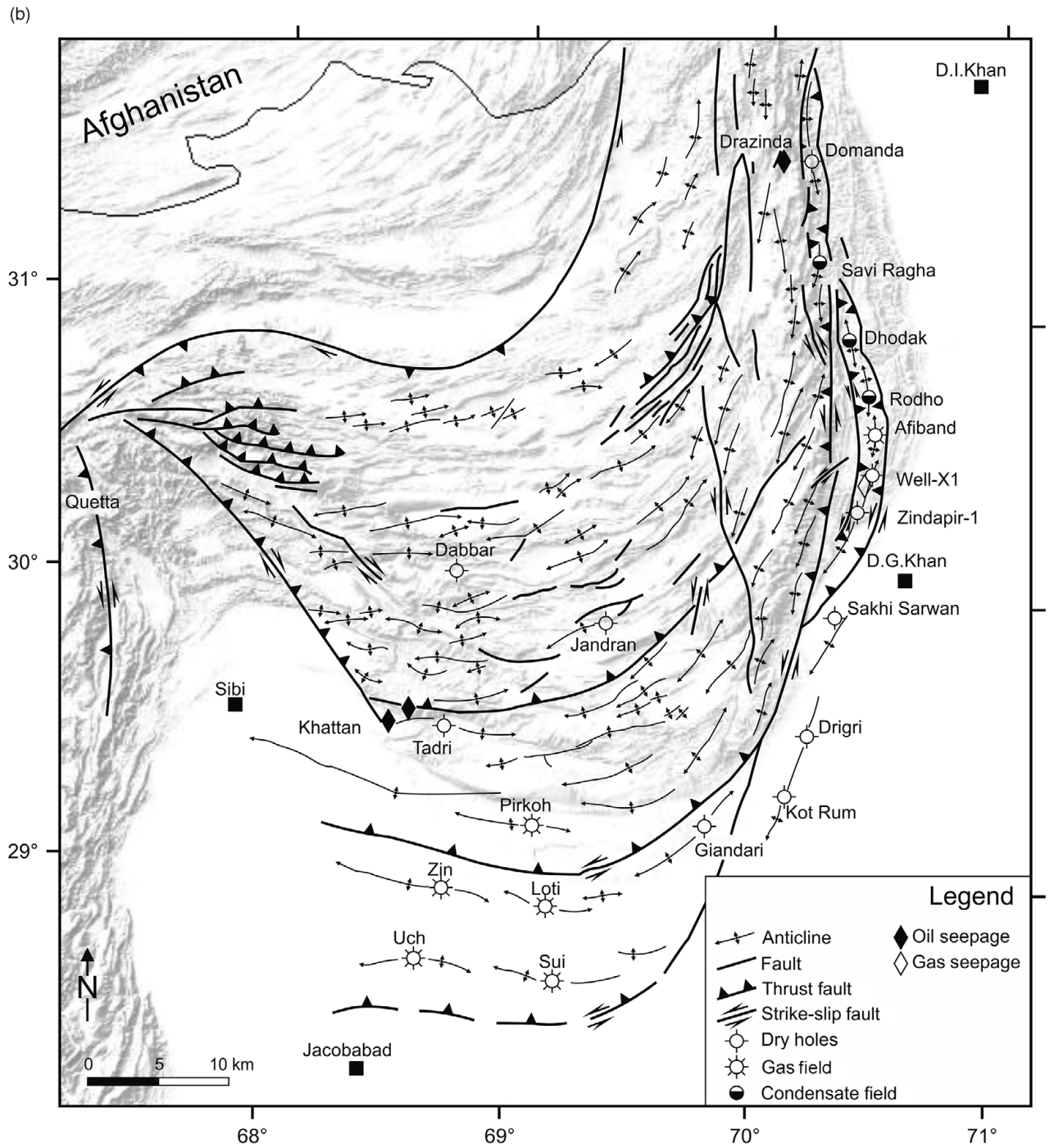

Figure 1.15 (b) Transfer faults bounding the Sulaiman Range, Pakistan (Nazeer et al., 2013).

1) synthetic strike-slip faults – R (Riedel) shears;
2) fault splays at ends of R shears;
3) antithetic strike-slip faults – R′ (conjugated Riedel) shears;
4) secondary synthetic strike-slip faults – P shears;
5) tensile fractures – T fractures;
6) normal faults;
7) folds;
8) antithetic strike-slip faults – X shears symmetric with R′ shears;
9) shear lenses having long axes parallel to principal displacement zone; and

https://doi.org/10.1017/9781108686631.002

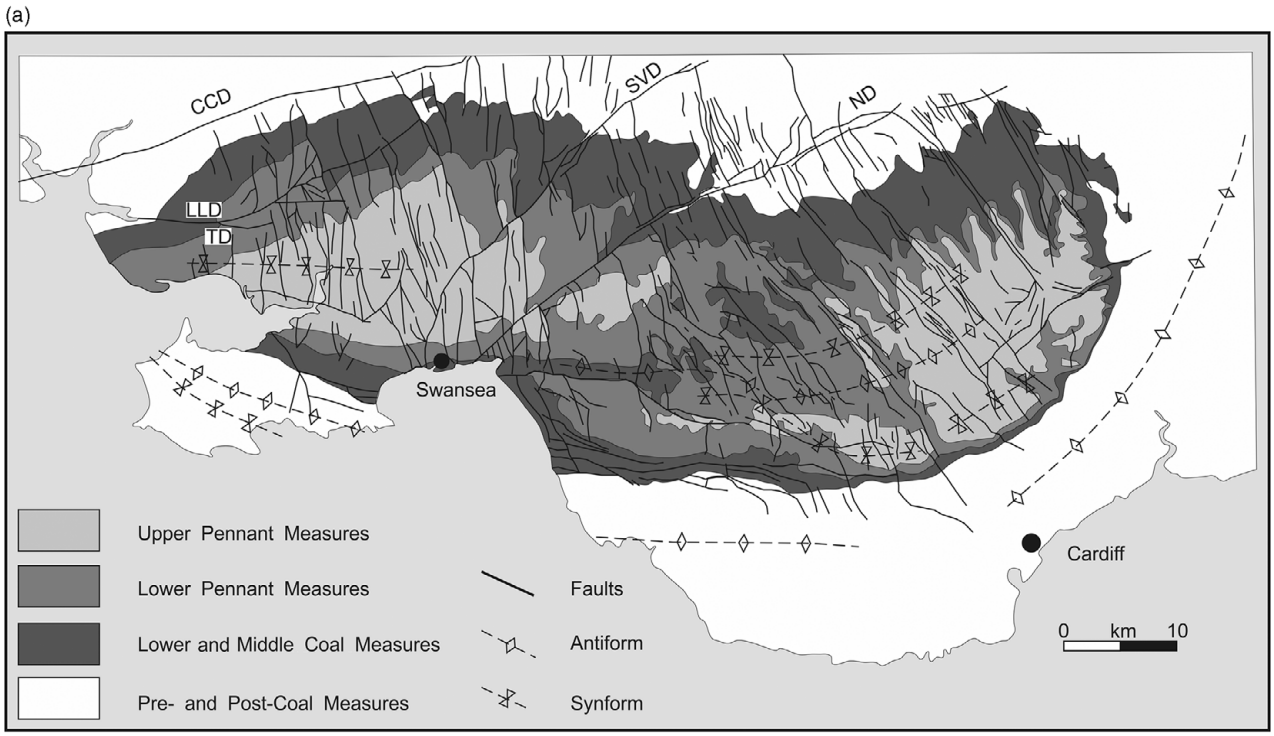

Figure 1.16 (a) Geological map of the portion of the Variscan external margin in southwestern Britain showing a system of tear faults and Variscan tectonic transport directions at numbered outcrops (Gayer et al., 1998). CCD – Careg Cennen Disturbance, LLD – Llanon Disturbance, ND – Neath Disturbance, SVD – Swansea Valley Disturbance, TD – Trimsaran Disturbance.

Figure 1.16 (b) Sinistral tear fault (dip direction/dip-trend/plunge = 105°/90°–18°/16°) deforming the Paleocene Komarevo Formation of the Forebalkan Unit near Dobromir Village, Eastern Balkans.

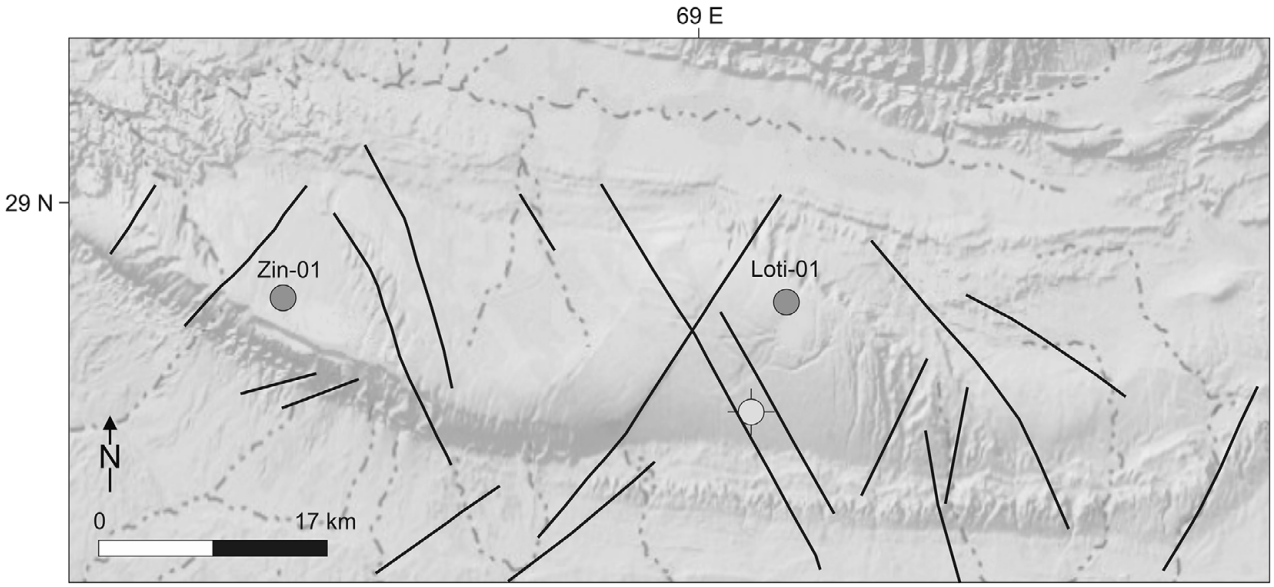

Figure 1.17 A system of small-scale conjugate strike-slip faults in the frontal Zin-Loti anticline of the Sulaiman Range, Pakistan (Khan et al., 2009).

10) strike-slip faults parallel with principal displacement zone – Y shears.

Mechanical theory for simple shear (Cloos, 1928; Riedel, 1929), using Coulomb's criterion, allows one to calculate the exact geometry of individual shears with respect to the principal displacement zone, as controlled by the angle of internal friction of the deforming material, φ. Riedel shears are located at an angle of $\varphi/2$ from the direction of movement, oriented by the acute angle toward the movement direction. R′ shears lie at an angle of $90^\circ - \varphi/2$ from the movement direction. P shears are propagated at an angle of $\varphi/2$ from the direction of movement, being symmetrical to R shears.

The aforementioned analog material experiments and case studies have documented how strike-slip faults progressively develop by a sequence of deformation events, developing different architectural elements from the list above (Figure 1.18a). Each new generation of shears is better suited for the accommodation of the involved block displacements – that is, they are capable of taking over a larger proportion of the overall displacement. Progressive linkage of architectural elements eventually results in a system of isolated lenses of passive material roughly parallel to the principal displacement zone. After this stage, the strike-slip fault zone reaches the residual deformation stage, which takes place at reduced friction, and almost all its displacements are accommodated along a single principal displacement zone. For any normal stress, the shear stress, which was at its peak at the Riedel shear development stage, has decreased to a lower value sufficient for overcoming the residual strength of the fault zone.

Folds associated with strike-slip faults are arranged in an en echelon pattern with respect to the principal displacement zone. They plunge in both directions away from the principal displacement zone, and have steeply dipping axial planes. They commonly develop in the sedimentary cover, decoupled from the basement deformed by the strike-slip fault. As the strike-slip fault propagation continues into the sedimentary cover, their two halves get cut and displaced.

A progressive addition of new generations of architectural elements in developing strike-slip fault zones is frequently affected by reactivation of pre-existing zones of weakness. Even the previously created architectural elements of the developing zone represent an anisotropy, which has a progressively growing influence on the evolution of the strike-slip fault system (Woodcock and Fischer, 1986).

Linkage of various types of shears results in upward-diverging shears linked into a relatively narrow zone toward the trace of the strike-slip fault zone at depth (Christie-Blick and Biddle, 1985). Such features are best imaged in reflection seismic profiles and are known as flower structures (Gregory in Harding and Lowell, 1979) or palm-tree structures (Sylvester and Smith, 1976; Figure 1.18b).

Because a large strike-slip fault zone grows by the nucleation and linkage of various architectural

https://doi.org/10.1017/9781108686631.002

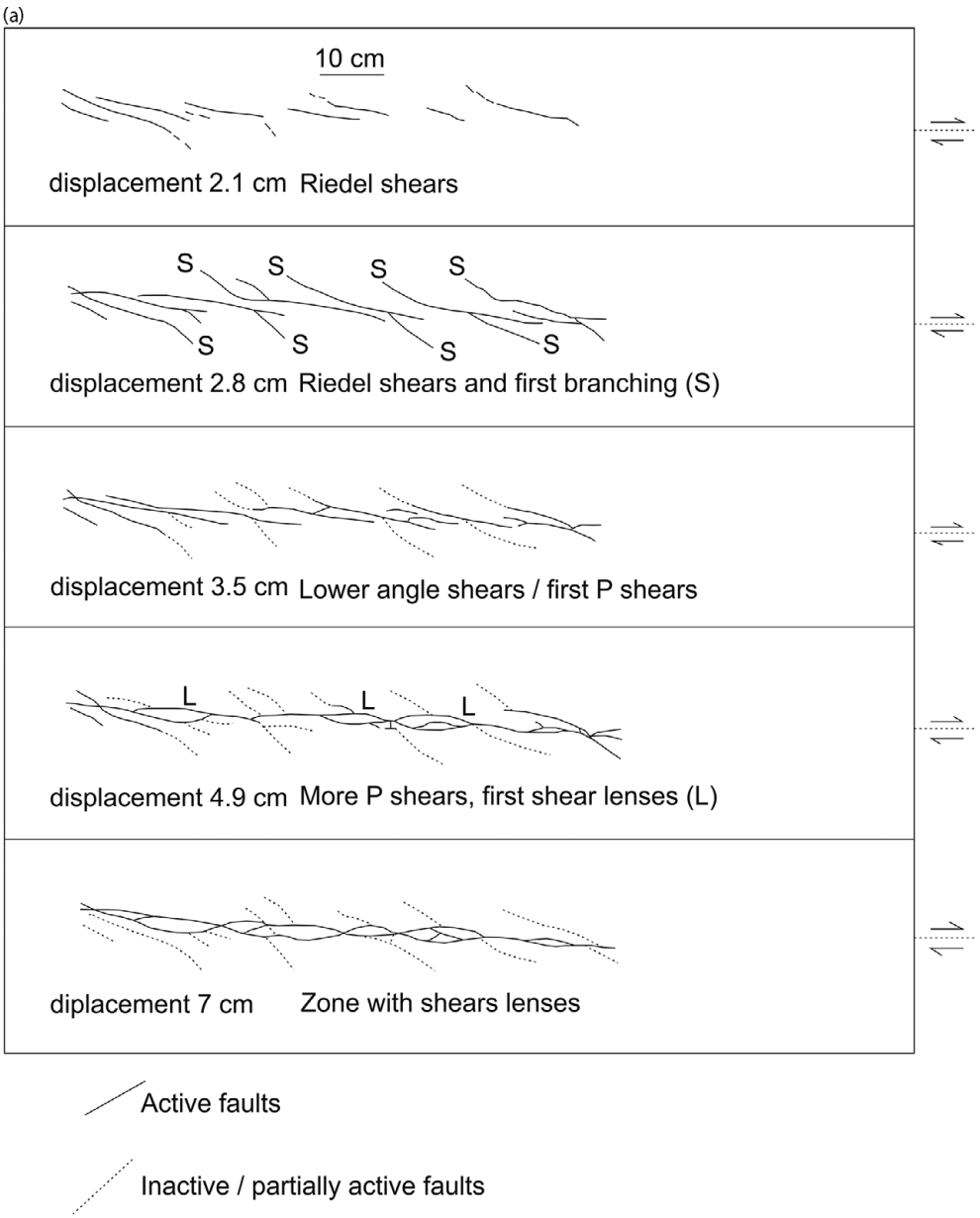

Figure 1.18 (a) Development of pure strike-slip fault (Naylor et al., 1986).
Reprinted from the *Journal of Structural Geology*, 8(7), M. A Naylor, G. Mandl, C. H. K Supesteijn. Fault geometries in basement-induced wrench faulting under different initial stress states. 737–752. ©1986, with permission from Elsevier.

elements developing at various locations along its strike, the zone usually contains multiple strike-slip fault segments. They have different relationships to the overall displacement and controlling stresses and include (Crowell, 1974; Woodcock and Fischer, 1986; Gamond, 1987; Figure 1.19a):

1) releasing bends;
2) restraining bends;
3) strike-slip duplexes;
4) strike-slip fans or horse-tail structures;
5) releasing offsets;
6) restraining offsets;
7) contractional bridges; and
8) extensional bridges.

All are characterized by a distinct vertical displacement amplitude (Woodcock and Fischer, 1986).

https://doi.org/10.1017/9781108686631.002

Figure 1.18 (b) Line drawing of the NNE–SSW striking reflection seismic profile through the Elk Hills anticline, Southern San Joaquin Basin, showing a positive flower structure (Nemčok and Schamel, 2000).

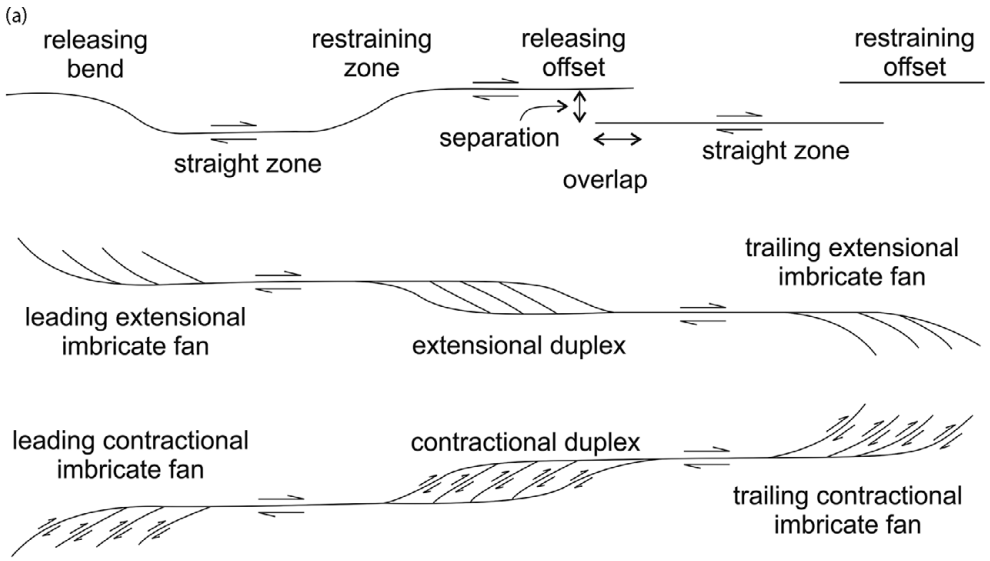

Figure 1.19 (a) Structures in the strike-slip fault (Woodcock and Fischer, 1986).
Reprinted from the *Journal of Structural Geology*, 8, Woodcock, N. H. and Fischer, M. Strike-slip duplexes. 725–735. ©1986, with permission from Elsevier.

As documented by the Dasht-e-Bayaz Fault case study (Tchalenko and Ambraseys, 1970), releasing and restraining areas are characterized by subsidence and uplift, respectively. The Transverse Ranges to the north of Los Angeles along the San Andreas Fault are an example of such a restraining bend.

Strike-slip duplexes – that is, fault-bound lenses imbricated between overlapping en echelon fault

segments – do not function like duplexes in thrust belts or extensional terrains. In the case of thrust and extensional duplexes, the plane strain is maintained in the vertical plane by the deformational reactions of the surface to the thickening or thinning of the duplex. However, in the case of strike-slip faults, the analogous maintenance of plane strain in the horizontal plane is accompanied by lateral deformation of surrounding rocks. The plane strain in this case breaks down due to the vertical response of surrounding areas. Furthermore, vertically oriented strike-slip faults lack the gravity potential perpendicular to the fault plane that influences the sequence of fault development in duplexes with vertical movement.

Duplexes of systems with vertical movements usually maintain a similar character along one main fault zone, while both types of duplexes can coexist in a strike-slip fault zone. This is because duplexes of strike-slip fault zones can be created by several different kinematic processes (Woodcock and Fischer, 1986; Swanson, 1988, 1989, 2005; Marsh et al., 1990), while duplexes of thrust terrains are usually the result of a single process – that is, progressive footwall collapse taking place in the direction of the hanging wall movement.

Because of the zero volume change, shortening of a contractional duplex must be balanced by growth of its width, and lengthening of the extensional duplex must be balanced by reduction of its width (Hempton and Neher, 1986; Woodcock and Fischer, 1986). These shape changes of growing duplexes require accommodation in surrounding rocks, represented by uplift and subsidence of adjacent blocks.

Duplexes can travel along the principal displacement zone. Extreme examples of such large displacement, exotic duplexes, are analogous to far-traveled blocks in thrust terrains (Woodcock and Fischer, 1986). The Ancenis Terrane in the Hercynian Belt of Armorica provides an example of such an exotic duplex that has traveled along the dextral northern boundary of Gondwana (Shelley and Bossiere, 2001).

Duplexes, depending on their character, are characterized by different flower structures in reflection seismic images. Restraining duplexes create a positive flower structure with upward convex reflectors among faults (Figure 1.18b) and releasing duplexes create a negative flower structure with upward concave reflectors among faults. An example of the former occurs along the Atacama fault system in northern Chile (Cembrano et al., 2005). Examples of the latter occur in the Lambertville sill in New Jersey (Laney and Gates, 1996) and in the oil field-hosting Quealy duplex (Stone, 1995).

Kinematic development of a strike-slip fault zone requires the presence of displacement dissipation structures at both ends. The most typical structural patterns are horse-tail structures, known under various names (e.g., Wilcox et al., 1973; Crowell, 1974; Christie-Blick and Biddle, 1985; Woodcock and Fischer, 1986; Sylvester, 1988; Figure 1.19a). A good example of a mesoscale horse-tail structure associated with dextral strike-slip in the Lower Jurassic section of the Bristol Channel is shown in Figure 1.19b. Large-scale examples are associated with the Lavic Lake Fault in California and several faults in offshore Guyana (Figure 1.19c).

Not all naturally occurring strike-slip fault zones have pure strike-slip displacement. Depending on the relationship of their geometry to the controlling stress field, they can be divided into (Wilcox et al., 1973; Naylor et al., 1986):

1) pure strike-slip faults;
2) transtensional (divergent) strike-slip faults; and
3) transpressional (convergent) strike-slip faults.

Analogously to the aforementioned types of strike-slip duplexes, their flower structures vary (Harding et al., 1985). Transtensional strike-slip fault zones are characterized by negative flower structures with dominating synforms. Transpressional ones are characterized by positive structures with prevalent antiforms.

Analog material experiments (Naylor et al., 1986) have shown that these three types of strike-slip faults grow by the nucleation and linkage of different combinations and sequences of architectural elements. This results in their different character, allowing one to recognize them in reflection seismic images.

In the case of a pure strike-slip fault, the principal stresses of the controlling stress field can be characterized as $\sigma_{H1} = \sigma_{H2} < \sigma_V$, where σ_{H1} and σ_{H2} are horizontal and σ_V is vertical. The resultant architecture of this type is shown in Figure 1.18a.

In the case of a transtensional strike-slip fault, the controlling stress field can be characterized by $\sigma_{HMax} > \sigma_V > \sigma_{HMin}$. In this setting, the σ_1 stress is parallel to the principal displacement zone in the initial stage of the experiment. The finite strain in this setting is partitioned between the simple shear component representing the strike-slip faulting regime along the fault and the pure shear component representing the extension perpendicular to the fault.

The transtensional strike-slip fault is characterized by the simplest and straightest fault zone (Figure 1.20). R shears in en echelon arrangement are rare. A simple, long strike-slip fault is common. It propagates soon after a small displacement of the basal plates of the experimental apparatus. Minor branching of the fault zone can occur, associated with propagation of P shears. Shears in vertical cross section

https://doi.org/10.1017/9781108686631.002

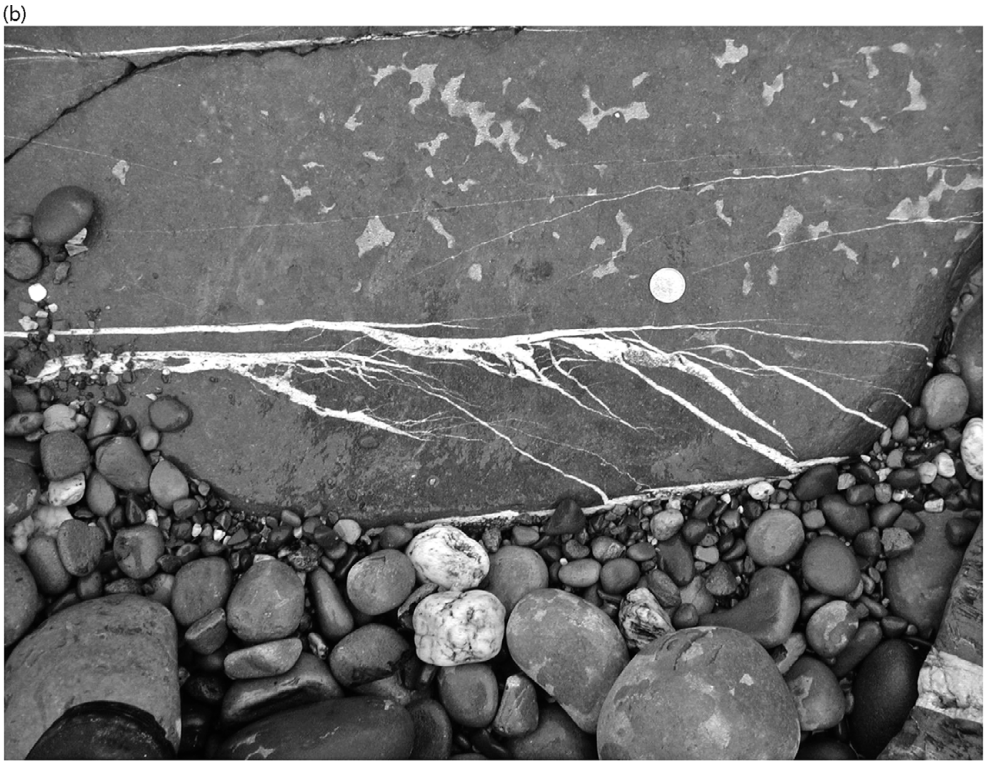

Figure 1.19 (b) Two horse-tail structures on receding sides of two dextral strike-slip faults the Liassic section in the Bristol Channel, UK.

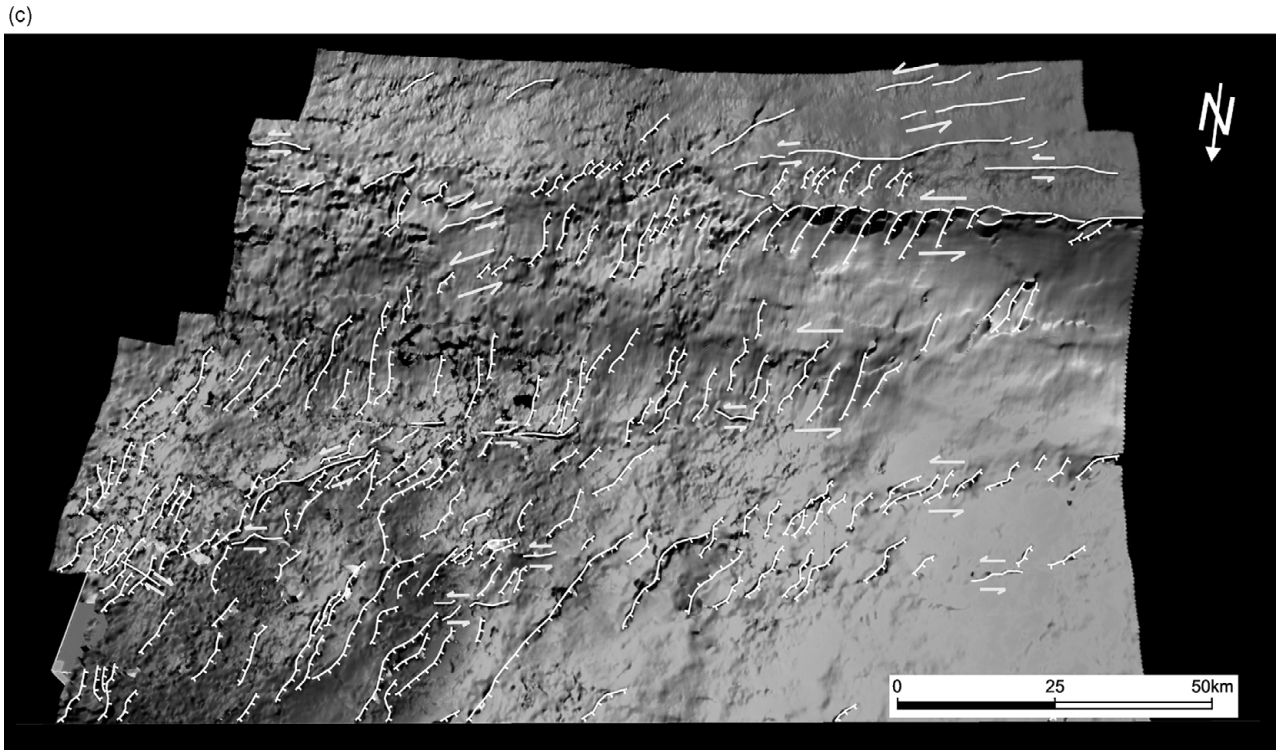

Figure 1.19 (c) Horse-tail structures on the retreating sides of sinistral strike-slip faults at Guyana Transform margin imaged by the 3D seismic volume (Nemčok et al., 2015a). Their horse-tail structures contain numerous small pull-apart basins. Mapped horizon represents the top of the strata having the age somewhere between the upper Barremian and the boundary between the Aptian and Albian. Note that most of the strike-slip faults reached only early stages of their evolution.

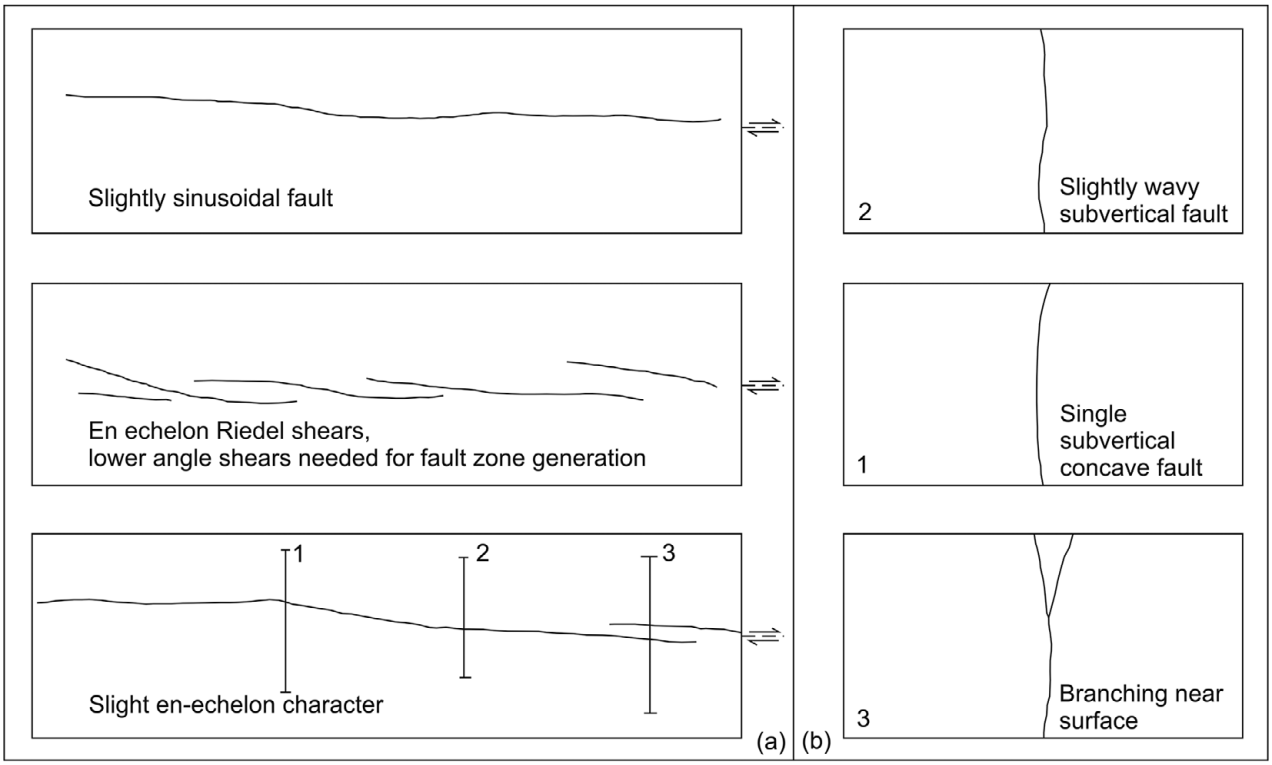

Figure 1.20 Transtensional strike-slip fault (Naylor et al., 1986), characterized by (a) map views and (b) cross sectional views. Reprinted from the *Journal of Structural Geology*, 8(7), M. A. Naylor, G. Mandl, C. H. K. Supesteijn. Fault geometries in basement-induced wrench faulting under different initial stress states. 737–752. ©1986, with permission from Elsevier.

have inclinations larger than 70°. Their traces in the section are usually straight. The cross section through the zone usually contains only a single fault or a single fault can branch into two faults in close proximity to the surface.

Transtension is also known to have caused topographic depressions parallel to the fault strike. Narrow elongated basins in the Tomales Bay north of San Francisco, and in the Buckeye and Meadow Parks in southern San Francisco, are good examples.

In the case of transpressional strike-slip faults, the controlling stress field can be characterized by $\sigma_{HMax} > \sigma_V > \sigma_{HMin}$. In this setting, the σ_1 stress is perpendicular to the principal displacement zone in the early stage of the experiment. The finite strain in this setting is partitioned between the simple shear component representing the strike-slip faulting regime along the fault and the pure shear component representing the compression perpendicular to the fault (Sanderson and Marchini, 1984).

The transpressional strike-slip fault is characterized by a wide and complex fault zone (Figure 1.21). The first R shears are at angles of more than 60° to the principal displacement zone. They can rotate around thrusts, which are parallel to the principal displacement zone. Increasing displacement sequentially generates shears oriented at progressively smaller angles to the principal displacement zone. The final zone eventually also includes P shears. The faults in cross section have dips around 25° in the vicinity of the base and 40–90° on the surface. The helicoidal aspect of R shears is, thus, very enhanced.

Transpression is also known to have caused topographic highs parallel to the fault strike. Narrow elongated pressure ridges along the San Andreas Fault in San Luis Obispo County and along the Lavic Lake Fault in California are good examples.

1.6 Structural Architecture of Pull-Apart Basins

Pull-apart basins are extensional depressions formed at releasing bends (Carey, 1958; Burchfiel and Stewart, 1966), extensional bridges (Petit, 1987), extensional oversteps (Christie-Blick and Biddle, 1985; Deng et al., 1986), releasing junctions (Crowell, 1974), and horse-tail structures of strike-slip fault systems. Their geometry is represented by rhomb-shaped graben, rhomb-shaped half-graben, series of coalescent basins (e.g., Schubert, 1980; Zak and Freund, 1981; Aydin and Nur, 1985; Sylvester, 1988; May et al., 1993) or more complex combination of fault blocks (Moore, 1969; Junger, 1976;

https://doi.org/10.1017/9781108686631.002

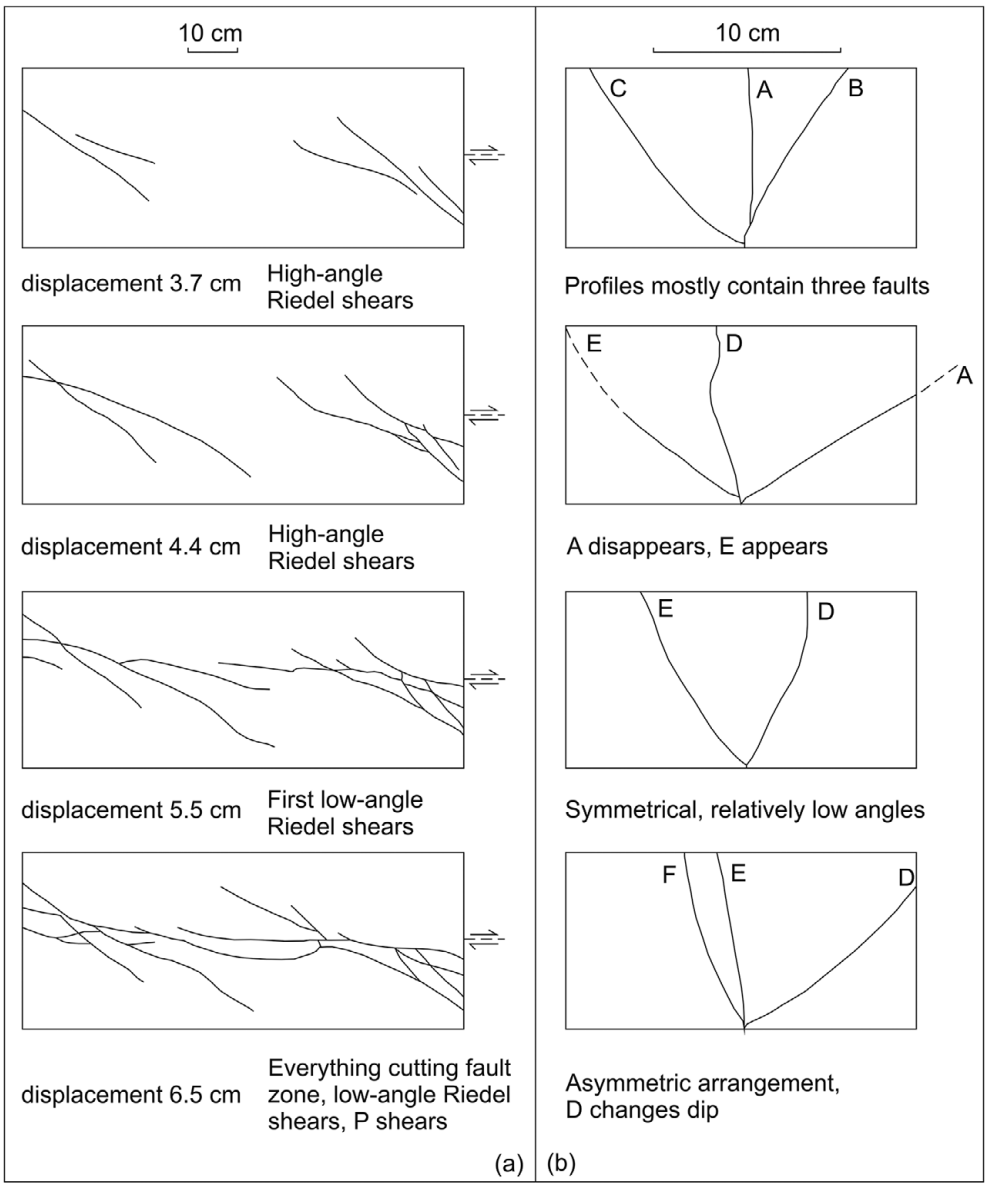

Figure 1.21 Transpressional strike-slip fault (Naylor et al., 1986), characterized by (a) map views and (b) cross sectional views. Reprinted from the *Journal of Structural Geology*, 8(7), M. A. Naylor, G. Mandl, C. H. K. Supesteijn. Fault geometries in basement-induced wrench faulting under different initial stress states. 737–752. ©1986, with permission from Elsevier.

Howell et al., 1980; Kocák et al., 1981; Royden, 1985; Fodor, 1995; Sims et al., 1999; Nemčok et al., 2005a).

Natural geometries of pull-apart basins have been successfully reproduced by analog models (e.g., Hempton and Neher, 1986; Horsfield and Naylor in Mandl, 1988; McClay and Dooley, 1995; Dooley and McClay, 1997). Modeling results indicate that basin geometry in map view is controlled by factors such as depth to basement, spacing between parallel or en echelon fault strands, and size of an overstep (Mandl, 1988; Richard et al., 1995) in accordance with interpretations made from natural examples (Sylvester, 1988). They also indicate that internal geometries and basin symmetries are controlled by displacement along the boundary faults (Faugére et al., 1986) and by relative displacement rates along them (Rahe et al., 1998).

Based on their depth of detachment, pull-apart basins can be separated into thick- and thin-skinned pull-apart basins (Royden, 1985). Examples of the former come from the Gulf of Elat in the Southern Dead Sea (Ben-Avraham and Zoback, 1992), the Gulf of Paria in Venezuela and Trinidad (Sims et al., 1999) and the Salton Trough region in the US and Mexico (e.g., Elders et al., 1972; Elders and Sass, 1988; Herzig et al.,

https://doi.org/10.1017/9781108686631.002

1988; Lonsdale, 1991). Examples of the latter come from Death Valley, California (Burchfiel et al., 1987) and the Ridge Basin, California (e.g., May et al., 1993). In certain cases, the depth of detachment within a basin can vary, making different portions thin- and thick-skinned, as is the case in the northern and southern portions of the Vienna Basin pull-apart basin (Lankreijer, 1998).

Depending on their pressure/temperature conditions and lithologic control, the detachments of pull-apart basins can have brittle or ductile deformation character. Thick-skinned types of pull-apart basins with detachment depths below the brittle–ductile transition and pull-apart basins detached along evaporites as the Gulf of Elat (ten Brink and Ben-Avraham, 1989) form the ductile detachment case, and thin-skinned pull-apart basins constitute the brittle detachment case.

The detachment character exerts an important control on the pull-apart structural architecture, as demonstrated by the series of analog material experiments made by Sims et al. (1999). The structural architecture of a pull-apart basin with brittle detachment is represented by a single basin with dominant normal faults controlling the basin geometry and subsidence. The subsidence in the basin, which is located above the brittle detachment horizon, initiates earlier than subsidence in basins developed above ductile detachments. This is because there is no ductile layer, which would take a share of the extensional deformation before the extension in the brittle rock section manages to develop faults controlling the basin subsidence. Unlike in the basin above ductile detachment, the intra-basinal high in the center of the basin is minimal (Sims et al., 1999; Figure 1.22).

Pull-apart basin development above a ductile detachment, regardless of its thickness, initiates with Riedel shears at acute angles to the main boundary strike-slip faults, which try to link them (Sims et al., 1999;

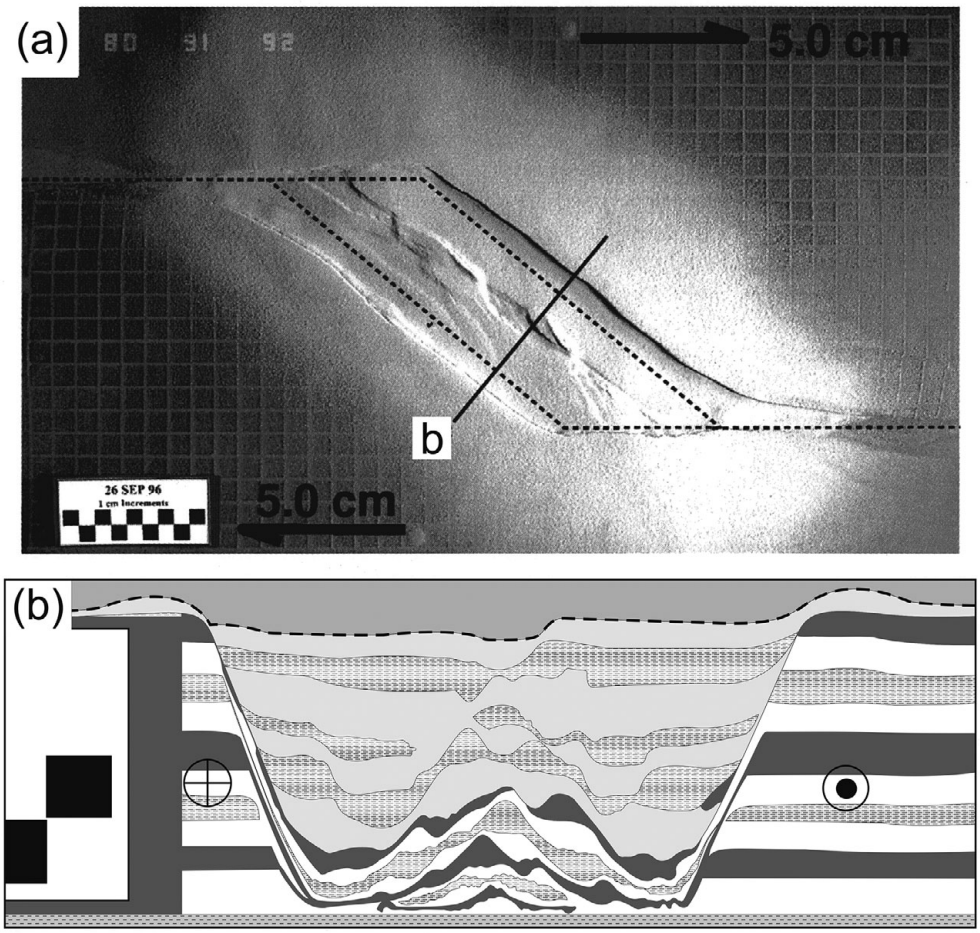

Figure 1.22 Map view (a) and vertical cross section (b) of the analog material model of the pull-apart basin detached along a brittle detachment (Sims et al., 1999).

Reprinted from the *Journal of Structural Geology*, 21(5), Sims, D., Ferrill, D. A. and Stamatakos, J. A. Role of a ductile decollement in the development of pull-apart basins; experimental results and natural examples. 533–554. ©1999, with permission from Elsevier.

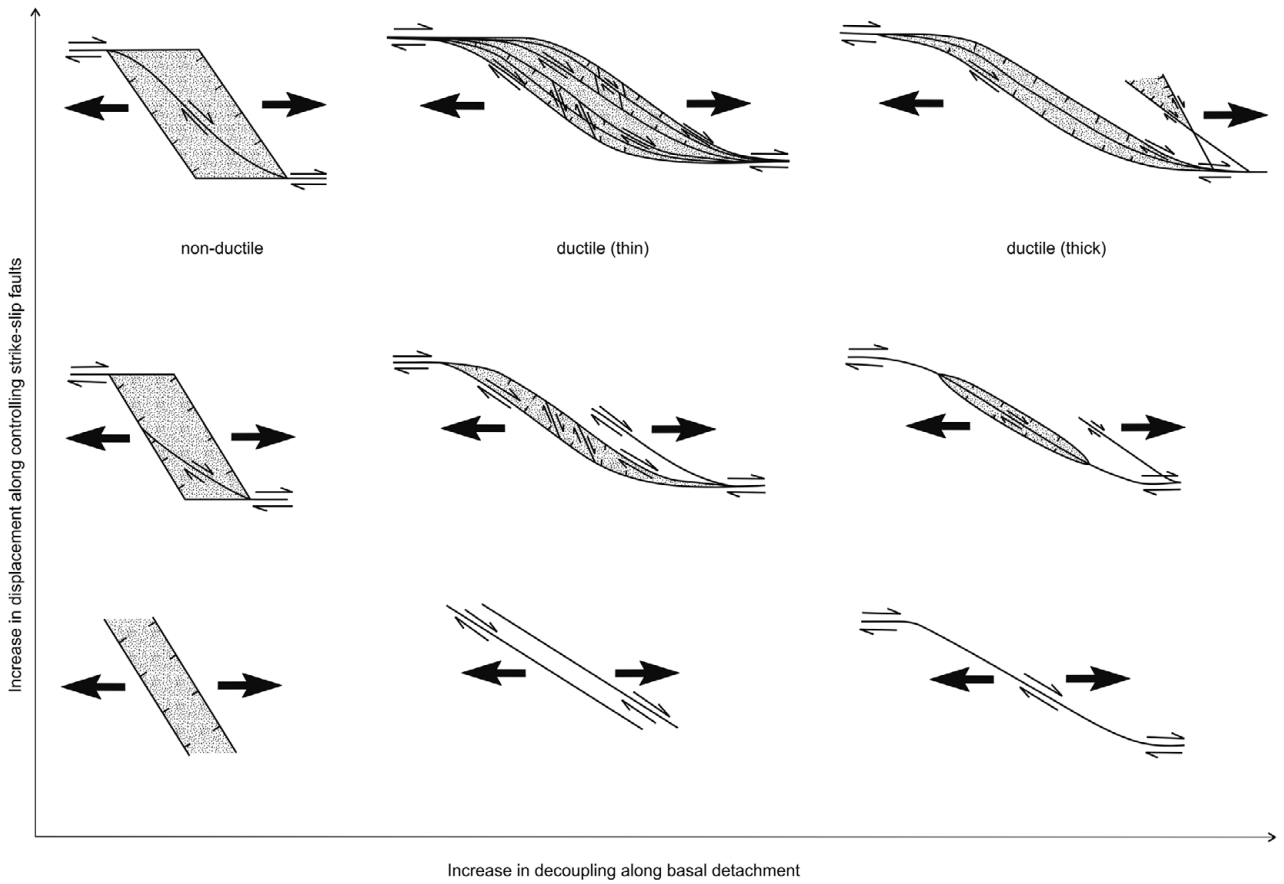

Figure 1.23 Structural architecture of modeled pull-apart basins detached along brittle, thin ductile and thick ductile detachments (Sims et al., 1999).

Reprinted from the *Journal of Structural Geology*, 21(5), Sims, D., Ferrill, D. A. and Stamatakos, J. A. Role of a ductile decollement in the development of pull-apart basins; experimental results and natural examples. 533–554. ©1999, with permission from Elsevier.

Figure 1.23). Riedel shear propagation is closely followed by propagation of both P and antithetic Riedel shears. The system with these three shear types develops a complex of strike-slip duplexes, which undergo rotations in a sense identical with the displacement sense on main bounding strike-slip faults. Later, strike-slip faults parallel to the bounding strike-slip faults develop. The basin subsidence begins with development of normal faults and initiation of a localized dip-slip component of displacement on Riedel and antithetic Riedel shears. Dip-slip displacement varies along the strike of the pull-apart basin, controlling asymmetric sub-basins with flip-flop switch along the basin strike. The pull-apart basin of this detachment scenario is represented by a complex of isolated or coalescing sub-basins having strike-slip fault-dominated geometries. The thickness of the ductile detachment horizon exerts an important control on the basin geometry in this scenario. The reason is that basin geometry is controlled by Riedel shears, which have geometries controlled by the thickness of the ductile detachment layer.

A pull-apart basin above a thick ductile detachment horizon commonly centers along a dominant Riedel shear that directly links the propagation tips of the main bounding strike-slip faults (Sims et al., 1999; Figures 1.23 and 1.24). It controls a simple flip-flop basin asymmetry. The basin is relatively shallow. Its development can be followed by development of neighbor basins divided from the initial pull-apart basin by remnant between-basin highs, which do not usually contain syn-rift sediments. Basins above a thick ductile detachment undergo subsidence later than those above a thin ductile detachment. This is because the ductile layer takes a portion of the extensional deformation before the extension in the brittle overlying rock section develops faults, which control the basin subsidence.

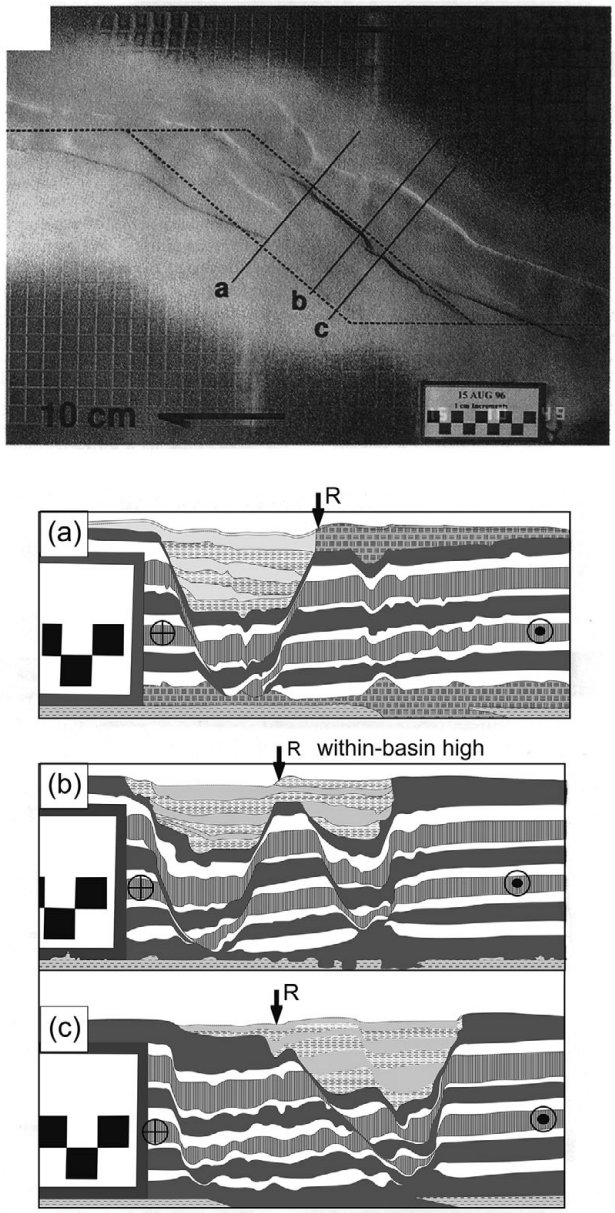

Figure 1.24 Map view and vertical cross section of the analog material model of the pull-apart basin detached along a thick ductile detachment (Sims et al., 1999).
Reprinted from the *Journal of Structural Geology*, 21(5), Sims, D., Ferrill, D. A. and Stamatakos, J. A. Role of a ductile decollement in the development of pull-apart basins; experimental results and natural examples. 533–554. ©1999, with permission from Elsevier.

A pull-apart basin developed above a thin ductile detachment horizon develops between sub-parallel en echelon Riedel shears that connect propagation tips of the main bounding strike-slip faults (Sims et al., 1999; Figure 1.23). The basin asymmetry is controlled by intra-basin strike-slip transfer zones. These transfer zones define intra-basin highs. The highs in map view are elongate and sub-parallel to the basin margins. They separate the deeper opposing ends of the elongate internal basins. These highs are covered by syn-rift sediments as they undergo a certain amount of subsidence. Basins above a thin ductile detachment undergo subsidence earlier than basins above a thick ductile detachment.

It can be concluded that a flip-flop linkage of architectural elements in a pull-apart terrain is inevitable. In order to support this claim, we can discuss the finite-element model, which was made by Andreas Henk as a side-product of the study of the St. Donats compressive bridge (Nemčok et al., 2002). This model simulated four successive stages of pull-apart basin development characterized by (Figure 1.25):

1) 100 m underlap of main bounding strike-slip faults;
2) 0 m overlap of main bounding strike-slip faults;
3) 100 m overlap of main bounding strike-slip faults; and
4) 200 m overlap of main bounding strike-slip faults.

Controlling parameters are described in detail by Nemčok et al. (2002).

As the future main bounding strike-slip faults develop, their propagation tips contain juxtaposed advancing and retreating sides. The former develops extra contraction and the latter develops extra extension. The finite-element simulation indicates that those two advancing and receding areas undergo localized uplift and subsidence, respectively (Figure 1.25). As the future pull-apart bounding strike-slip faults propagate closer to each other, localized areas of subsidence start to interfere, initiating the causal flip-flop mechanisms for pull-apart terrains. Figure 1.25 shows that in the underlap scenario, subsiding areas at receding sides of propagating tips of meeting strike-slip faults are separated by a larger sigmoidal high. As the strike-slip faults propagate closer to each other, this high becomes narrower and smaller. It eventually vanishes when the overlap is achieved. As the overlap increases, the subsidence distribution inside the basin becomes more unified, losing the initial pronounced flip-flop character for younger stratigraphies in the basin fill. The total thickness of the basin fill, however, retains the depocenter asymmetry from the earlier stages of the pull-apart basin development.

The comparison of subsidence maxima from all four stages of the pull-apart development (Figure 1.25) demonstrates a particularly striking feature of pull-apart

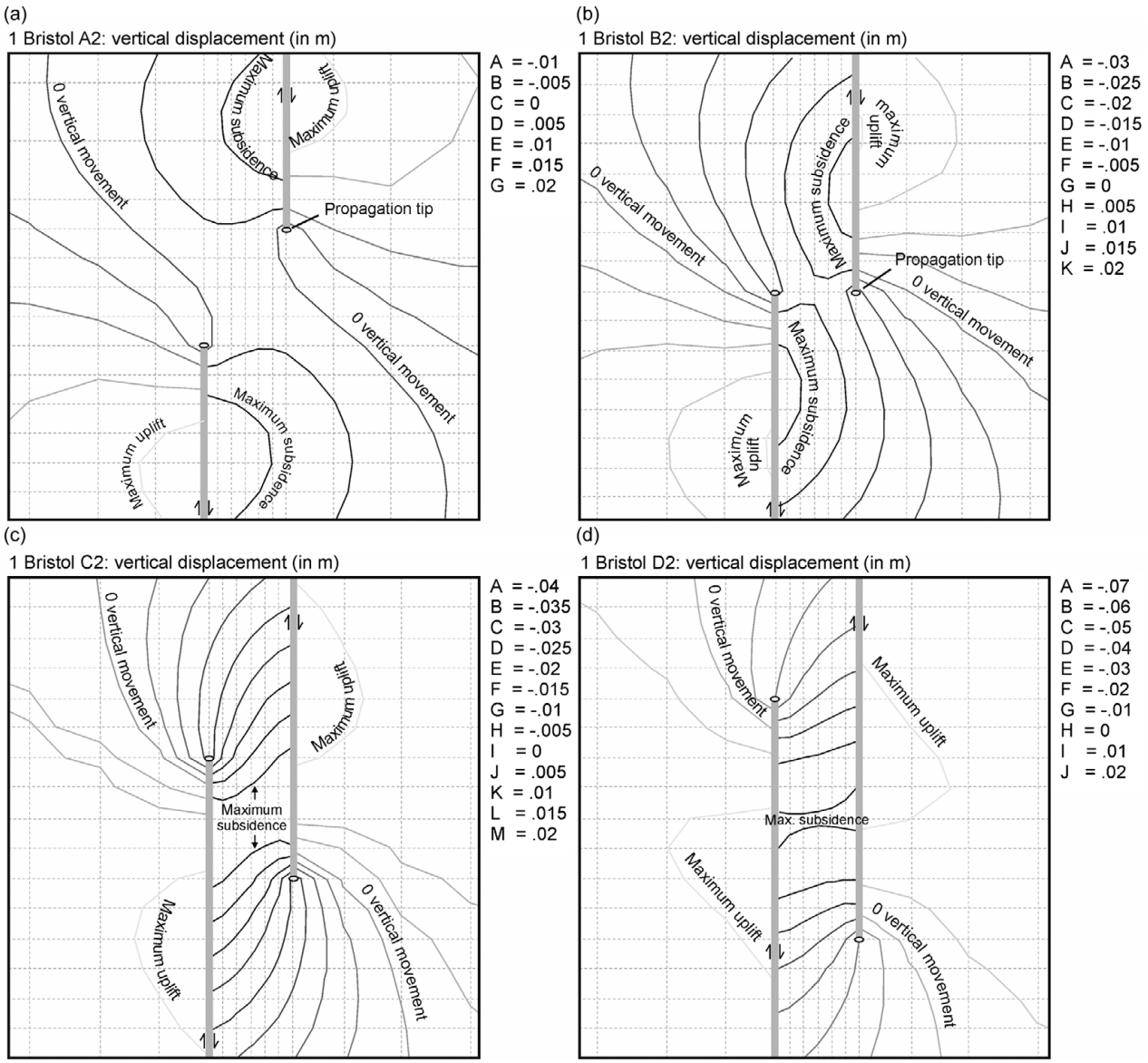

Figure 1.25 Four successive stages of the pull-apart basin development from underlapping to overlapping controlling strike-slip faults (Henk, 2001, pers. com.).

basins; the tendency for longitudinal and lateral asymmetry. Figure 1.25 shows that the depocenter can undergo large shifts in direction parallel to the controlling strike-slip faults. The depocenter of the Dead Sea Basin, for example, underwent a northward migration of over 100 km from its initial location in the Arava Valley to the Dead Sea between the Miocene and present day (Zak and Freund, 1981; Manspeizer, 1985).

It needs to be stressed, however, that the described modeling was performed using a layer of homogeneous isotropic material and for the brittle detachment scenario. Therefore, the model only indicates general trends of subsidence/uplift in relation to propagation of bounding strike-slip and normal faults. A real pull-apart basin, with its complex pattern of internal faults, would have much more complex subsidence/uplift patterns, as can be implied from the comparison of the fault pattern of the Vienna Basin (Kocák et al., 1981; Figure 1.26a) with subsidence histories from its various areas (Lankreijer, 1998; Figure 1.26b).

To add one more level of complexity, one can consider a block traveling along a complex geometry of the strike-slip fault zone from Figure 1.19a for many tens of kilometers. A reflection seismic section through such a

https://doi.org/10.1017/9781108686631.002

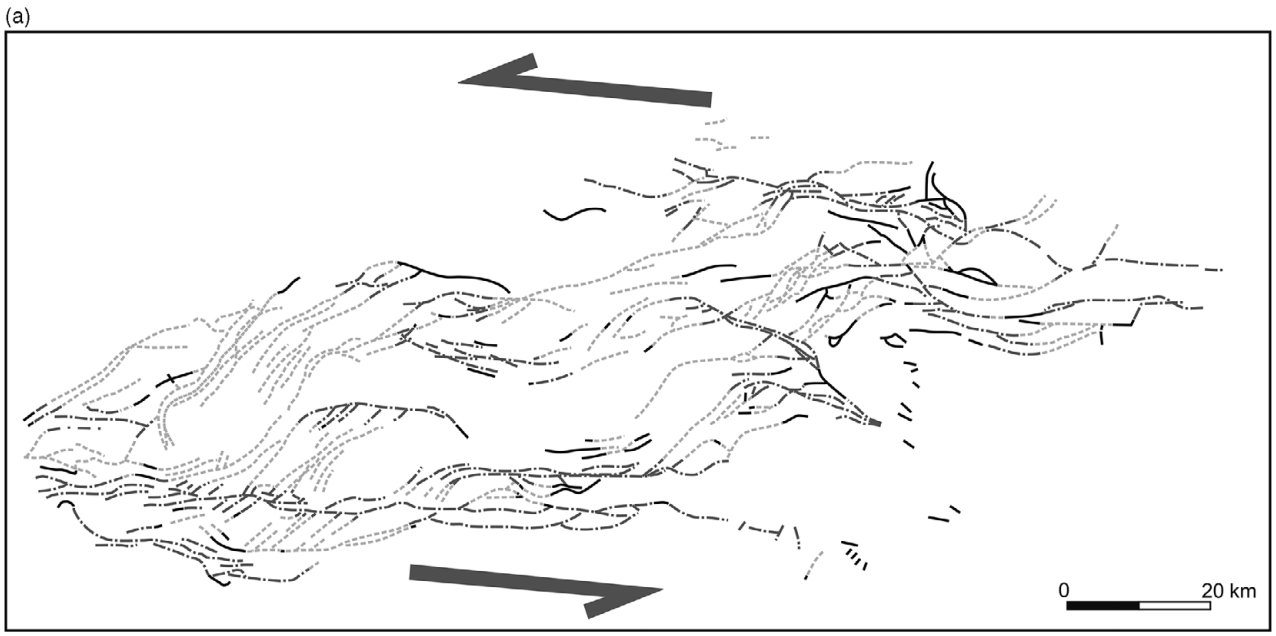

Figure 1.26 (a) Fault pattern of the Vienna Basin, Carpathians (modified from Kocák et al., 1981). Dark gray – normal faults, light gray – sinistral strike-slip faults.

block should allow one to interpret the time periods when this block was under the pure strike-slip faulting regime, when it underwent local transtension, and when it underwent local transpression on its way along the strike-slip fault zone (Figure 1.26c). A good example of such a complex behavior of a far-traveled block is provided by a whole system of numerous local and regional unconformities that occur in the Salinian Block in California (Greene and Hicks, 1990). They indicate alternating phases of subsidence and uplift, reaching sub-aerial exposure, of this block during its north-northwest translation along the dextral San Andreas Fault. This suggests that crustal slices of the Salinian Block "porpoise" along multiple restraining and releasing bends on their path along the main strike-slip fault zone, undergoing cycles of transpression, transtension, and pure strike-slip faulting.

Such a reconstruction exercise may prove to be critical in exploration projects seeking to understand charge histories from numerous passing-by source rock kitchens into the laterally traveling traps, each of them having just a limited time window for its charge into a specific trap, if mature enough at the right time. This exercise is rather important, because pull-apart basins associated with both interplate and intraplate strike-slip faults may host distinct hydrocarbon reserves, as indicated by hydrocarbon provinces of the Andaman Sea and Sumatra (Harding, 1974; Harding et al., 1985; Lowell, 1985; Williams and Eubank, 1995), the Malay Basin province in Malaysia (Ngah et al., 1996), Cuyama, Salinas, and San Joaquin provinces in California (Harding, 1976; Lillis, 1994; Peters et al., 1994), and the Ventura and Los Angeles provinces in California (Biddle, 1991; Redin, 1991; Wright, 1991).

1.7 Structural Architecture of Transform Margins

For reference in the following chapters of this book, a discussion of the structural architecture of transform margins must also include the architecture of the adjacent oceanic crust. This is because the adjacent oceanic crust contains the deformation recorded during the oceanic–continental stage of transform margin development. In contrast, the transform margin itself carries the deformation record developed during the initial continental and subsequent oceanic–continental stages of the transform margin development. The differences between deformation records of continental and oceanic crusts, their controlling factors, and dynamics are discussed in detail in Chapter 5.

The structural architecture developed by a continental transform contains all those deformation features discussed in the text on structural architectures of strike-slip faults and pull-apart basins. Tectonic settings of the continental transform can be roughly divided into the transform fault zone *sensu stricto* and

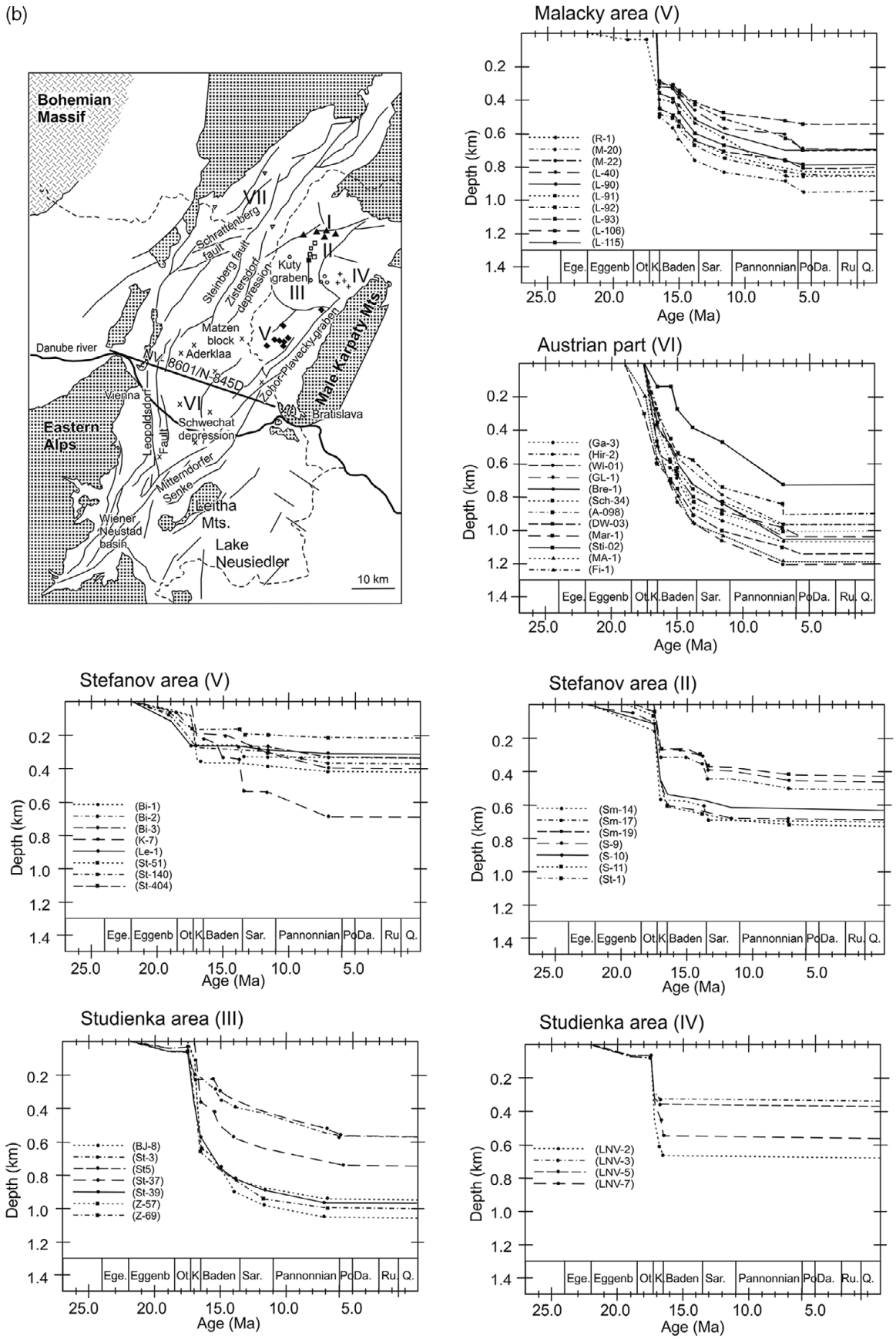

Figure 1.26 (b) Subsidence curves from various areas of the Vienna Basin pull-apart (Lankreijer, 1998).

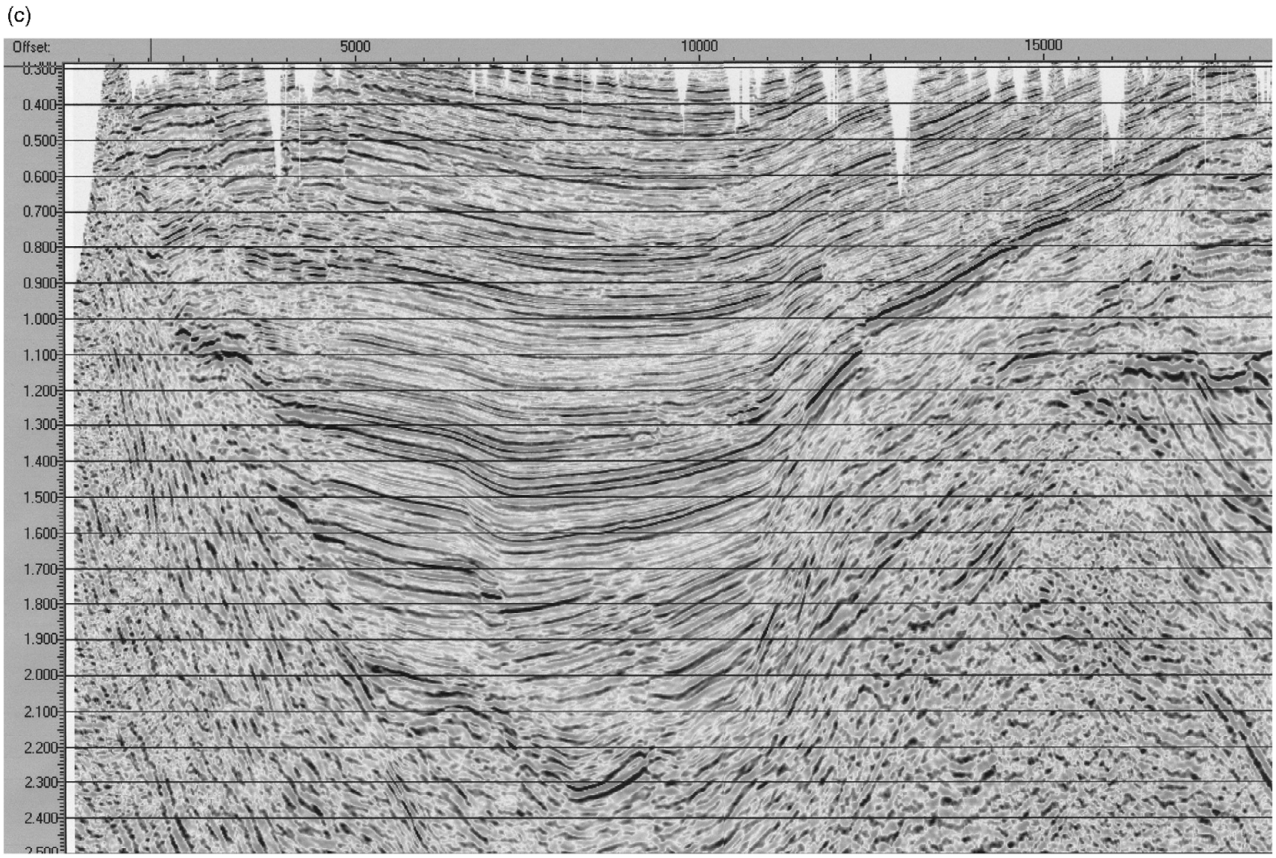

Figure 1.26 (c) Far-traveled block from the Vienna Basin with various portions of its strata representing syn-tectonic strata to transtensional strike-slip faulting, pure strike-slip faulting and transpressional strike-slip faulting (image courtesy of MND, Inc.).

horse-tail structures located at its ends. The function of the horse-tail structures is to dissipate the transform fault zone displacement down to zero at both transform terminations.

Horse-tail structures can also function as linkage structures. For example, in offshore East India, they linked the transfer fault zone preceding the Coromandal continental transform zone to neighboring orthogonal or oblique rift units (Nemčok et al., 2012b; Figure 1.27a). While the faults of the northern horse-tail structure of the Coromandal continental transform are fully linked with syn-rift faults of the Krishna–Godavari rift zone, the faults of the southern horse-tail structure first cross-cut the syn-rift faults of the Cauvery rift zone and both structures became kinematically linked only subsequently (Nemčok et al., 2012b; Sinha et al., 2016). The southern transform linkage could have been developed by the east-to-west Indian Ocean propagation through the evolving rift system. Starting in the east, the Mahanadi rift zone underwent ocean opening in the Berriasian, followed by the offshore remnant of the Cauvery rift zone in the west undergoing opening in the Valanginian (Sinha et al., 2016). However, the Krishna–Godavari rift zone, which was parallel to the successful portion of the Cauvery rift zone and located further north, eventually experienced ocean opening at the Barremian–Aptian transition and during the early Aptian in its eastern and western parts, respectively, causing a ridge jump by capturing the oceanic crust accretion that was taking place further south. Coevally with the breakup in its western portion, the faults of the Coromandal Transform fault in its post-breakup oceanic–continental stage propagated southward, eventually reaching the Cauvery rift zone.

Taking into account which horse-tail structure developed the spreading center that laterally migrated along the future transform margin in its oceanic–continental development stage and which horse-tail structure was deformed by the last active faults of the oceanic–continental transform (Figure 1.28), we can divide them into associated (AH) and joining (JH) horse-tail structures, respectively (Figures 1.27a–c). Figures 1.27a–b show that the associated horse-tail

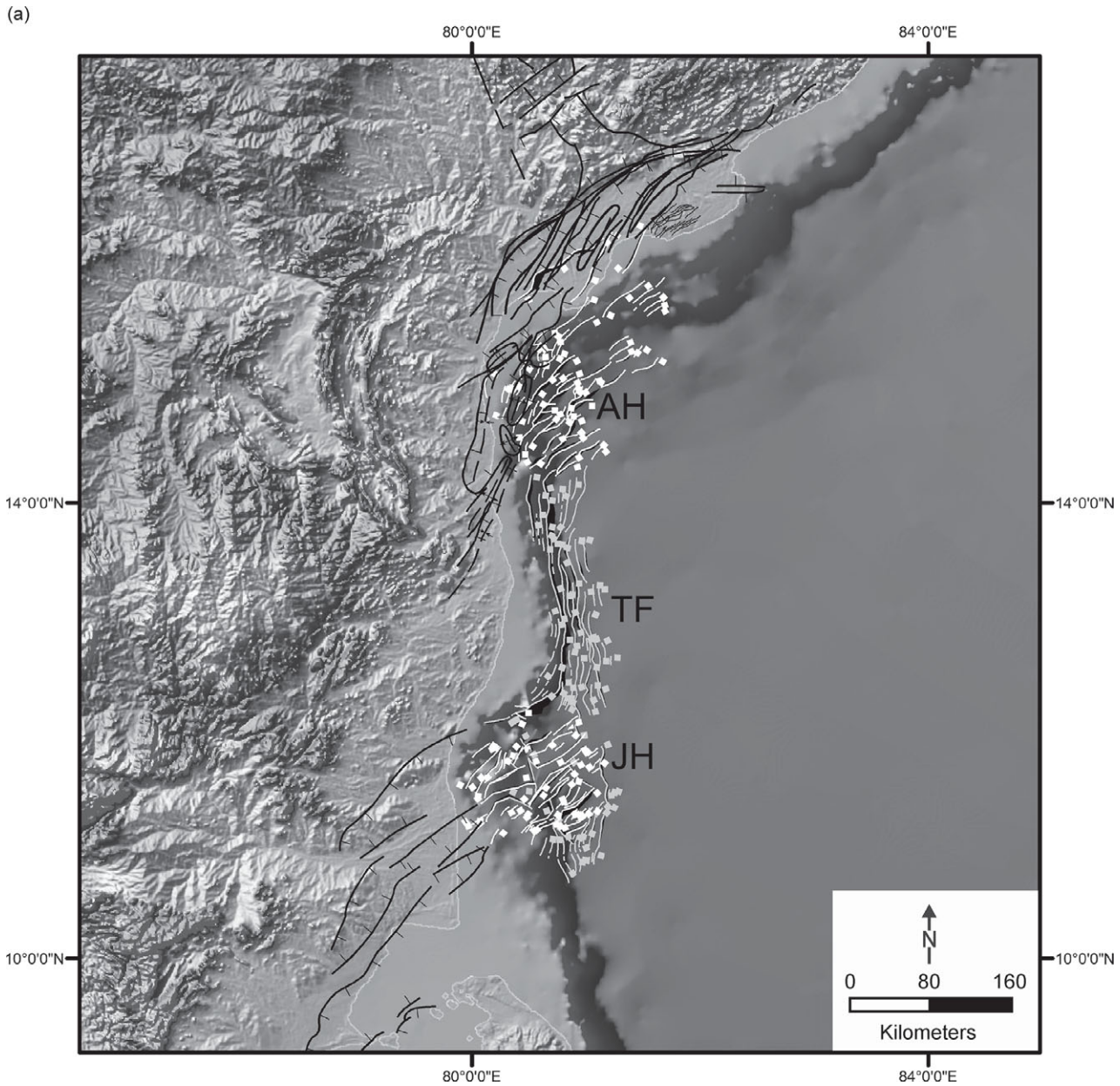

Figure 1.27 (a) Faults of the Coromandal Transform margin that were propagated during both the initial continental and subsequent oceanic–continental development stages of the transform. White faults are strike-slip, oblique-slip, and normal faults of the associated (AH) and joining (JH) horse-tail structures. Most of the faults representing the AH represent the deformation record of the continental transform stage. White faults of the JH are the deformation record of either both continental and oceanic–continental development stages of the Coromandal Transform or the record of the continental stage only. Gray faults of JH are the deformation record of the oceanic–continental stage only. Gray faults of the transform fault zone *sensu stricto* (TF) are the record of both continental and oceanic–continental stages.

structure is a relatively simple splay of faults changing from strike-slip faults to oblique-slip faults and then to normal faults in the direction away from the transform. Figures 1.27a–c indicate that the fault pattern of the transform fault *sensu stricto* is dominated by strike-slip faults, unless the pre-existing weakness caused the fault pattern to be more complex (compare Figures 1.27a and 1.27b). Figures 1.27a–c document that the fault pattern of the joining horse-tail structure is the most complex of those from these three transform margin

https://doi.org/10.1017/9781108686631.002

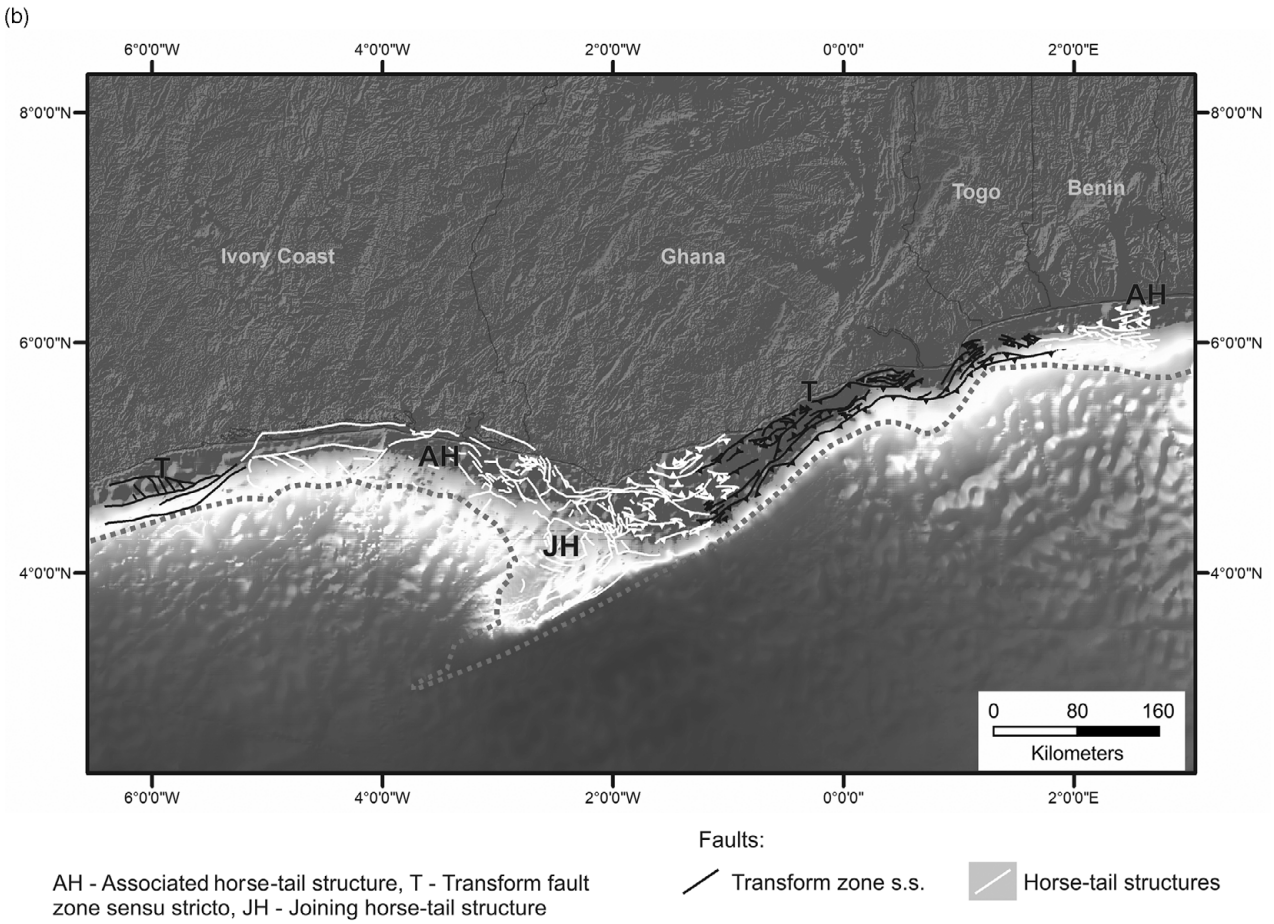

Figure 1.27 (b) Faults of the Romanche Transform margin that were propagated during both the initial continental and subsequent oceanic–continental development stages. See Figure 1.27(a) for further explanation. Background topography and bathymetry maps are from GEBCO (2019).

settings. The reason is that the propagation of the transform-related fault pattern was taking place in this setting until the final clearance of the spreading center from its contact with the future transform margin.

The geometry of fault patterns of each horse-tail structure depends on whether the transform kinematically links to a successful rift zone or a pull-apart terrain. For four combinations of such linkages, oceanic–continental transforms can be divided into transforms that link to:

1) rift zones at both ends, such as the Coromandal Transform;
2) pull-apart terrains at both ends, such as the Romanche Transform;
3) a rift zone at the AH end and a pull-apart terrain at the JH end; and
4) a pull-apart terrain at AH end and a rift zone at the JH end, such as the Zenith–Wallaby–Perth Transform.

Fault patterns of transforms *sensu stricto* in all four categories remain roughly similar. Fault patterns of horse-tail structures vary, depending on them linking to rift zones versus pull-apart terrains (compare Figures 1.27a and b).

The aforementioned fault patterns typical for three different transform margin tectonic settings control different types of traps along the transform margin (see Chapter 18).

Apart from the different fault patterns, the structural architectures of associated horse-tail structures, transforms *sensu stricto* and joining horse-tail structures differ by their different topographies and crustal thickness distributions.

The topography of a transform margin *sensu stricto* is characterized by a high plateau on the continental side, an abrupt transition between oceanic and continental crust, and a narrow shelf and slope (Figures 1.29a–b). A typical crustal thickness distribution is characterized

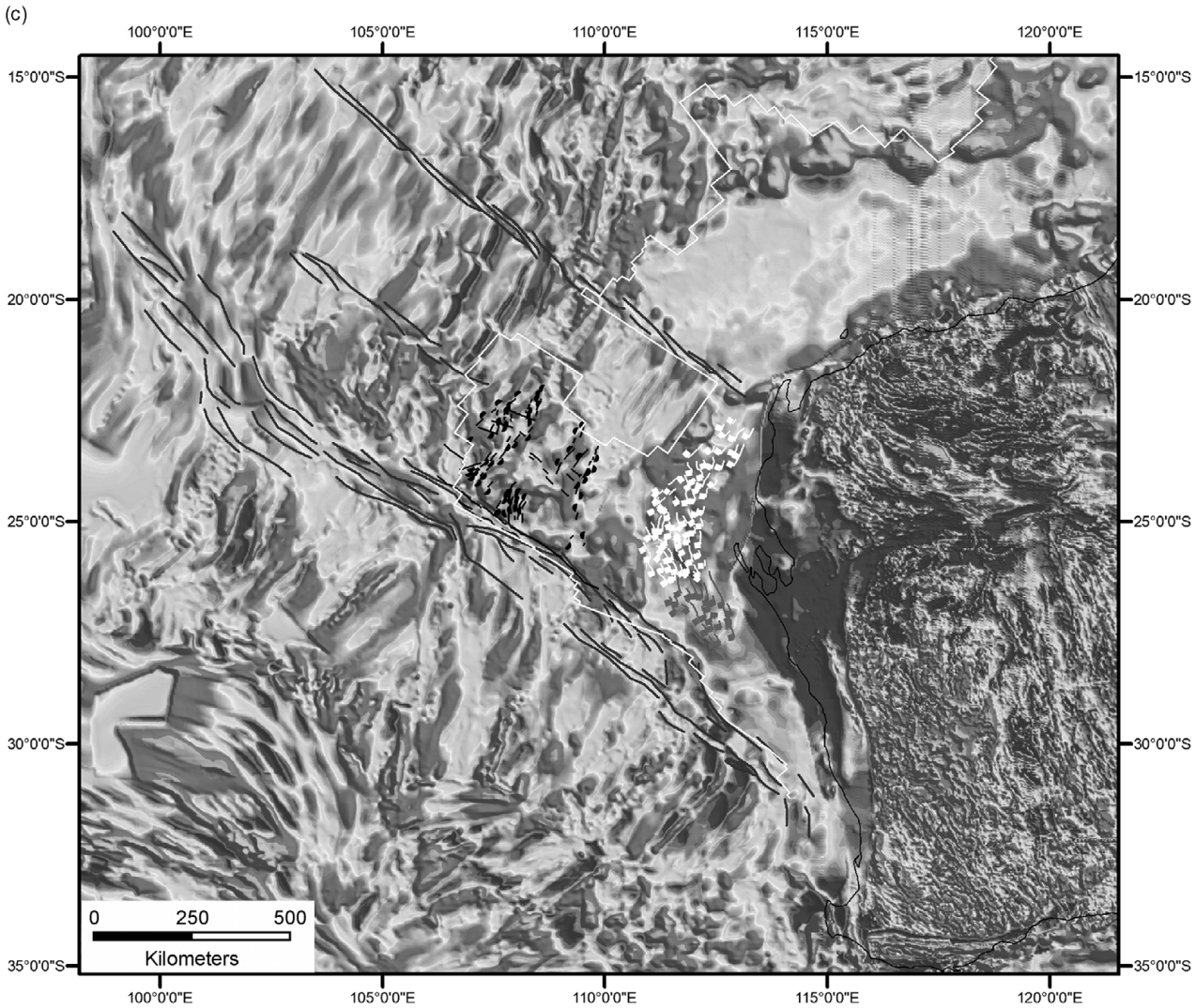

Figure 1.27 (c) Faults of the Zenith–Wallaby–Perth Transform fault system that were propagated during both the initial continental and subsequent oceanic–continental development stages. White faults with teeth – faults of the joining horse-tail structure of the continental transform fault zone; gray faults with teeth – faults of the continental transform fault zone *sensu stricto*; black faults with teeth – faults of the Wallaby Plateau; thin gray faults – faults of oceanic fracture zones and oceanic sides of oceanic–continental transform fault zones. Note that the oceanic development stage reactivated and deformed only the southern portion of the deformation pattern created by the continental transform stage. This is due to the change in plate motion vectors of involved blocks/plates that took place between the continental and oceanic–continental stages.

by a thick continental crust on the landward side of the ocean–continent boundary (Figure 1.30a) in the case of transforms *sensu stricto* dominated by strike-slip faults, such as in the case of the Coromandal Transform margin. If any pre-existing zones of weakness cause a development of pull-apart imperfections inside the transform *sensu stricto*, their extensional sides become loci of localized progressive crustal thinning (Figure 1.30b), such as in the case of the Romanche Transform margin.

The topography of the associated horse-tail structure is characterized by a system of long ridges and valleys descending in direction away from the transform in the case of linkage to a rift zone, or by a system of terraces descending in the direction away from the transform in the case of linkage to a pull-apart terrain, and a progressively wider shelf and continental slope in the direction away from the transform (Figures 1.29a–b). A typical crustal thickness distribution includes a progressive oceanward crustal thinning that becomes more

https://doi.org/10.1017/9781108686631.002

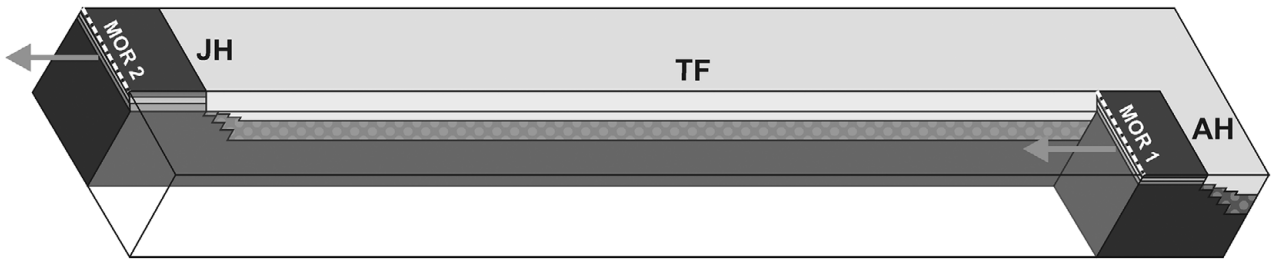

Figure 1.28 Sketch of the post-breakup situation of a transform linking two successful rift zones. It can be divided into three tectonic settings during its evolution into the transform margin. AH – associated horse-tail structure, TF – transform fault *sensu stricto*, JH – joining horse-tail structure, MOR – spreading center. Oceanic crust is divided into three layers, continental crust into two.

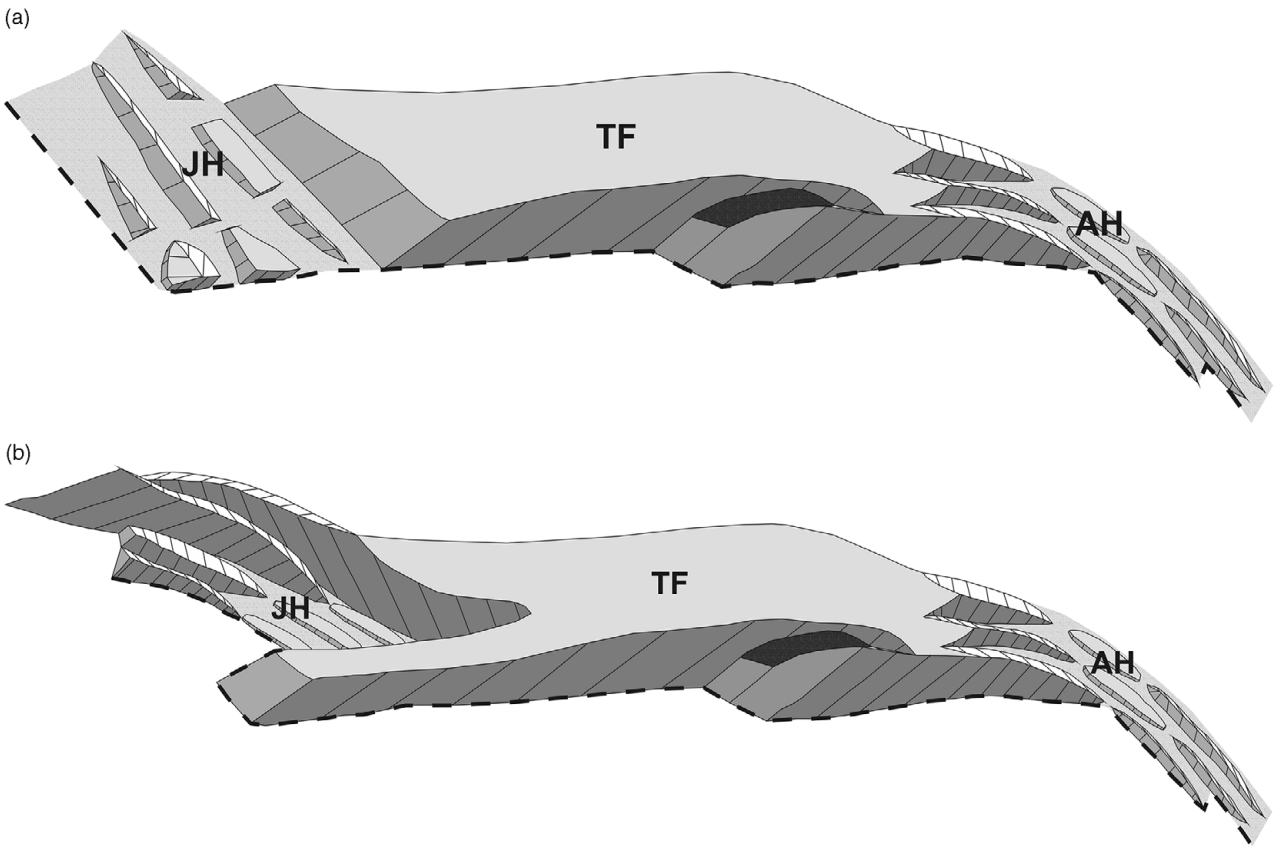

Figure 1.29 Typical topography characterizing the associated horse-tail structure, transform margin *sensu stricto*, and joining horse-tail structure in the case of a transform linking (a) successful rift zones and (b) successful pull-apart terrains. Black dashed line – boundary between oceanic and continental crusts.

and more important in the direction away from the transform, and a similar thinning style once the horse-tail structure reaches the rifted margin (Figure 1.30a). This thinning style may not be similar along the margin if it is a pull-apart rather than a rifted margin (Figure 1.30b).

The topography of the joining horse-tail structure is characterized by a system of local cylindrical highs inside the zone of last active strike-slip faults. This changes into a system of elongated highs away from this zone in the case of linkage to a rift zone, or it remains composed of local highs and lows in the case

https://doi.org/10.1017/9781108686631.002

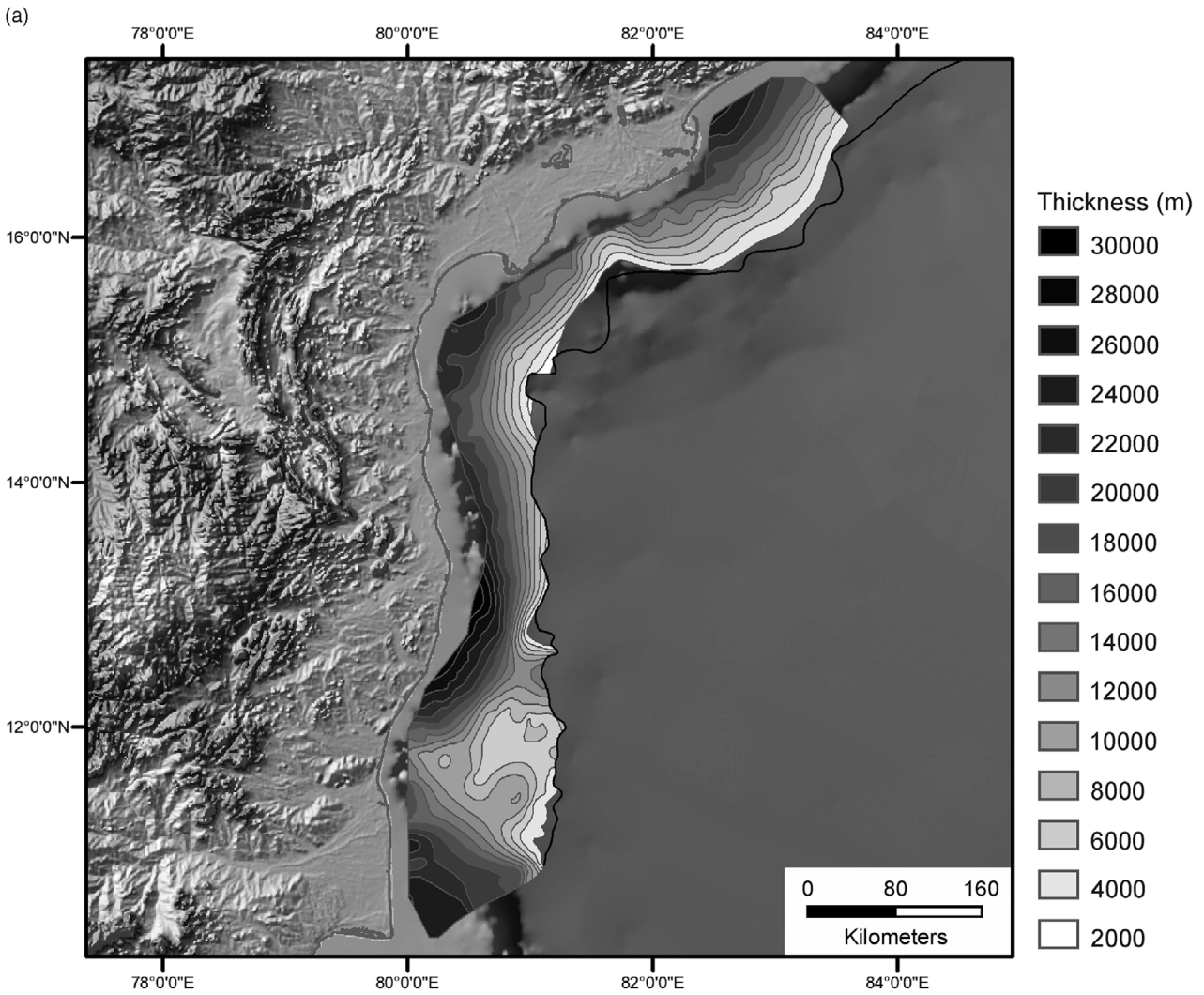

Figure 1.30 (a) Thickness map of the continental crust of the Coromandal Transform margin with location of the boundary between continental and oceanic crusts (black line), on top of offshore bathymetry and onshore topographic maps.

of linkage to a pull-apart terrain. The topography is also characterized by a wider shelf and continental slope (Figures 1.29a–b). A characteristic crustal thickness distribution is similar to that of an associated horse-tail structure and its rifted margin neighbor in the case when a transform links to a successful rift zone (Figure 1.30a). In the case of linkage to a successful pull-apart terrain, the crustal thickness distribution includes a distinct elongated reduced thickness "embayment" between the so-called marginal ridge, which is located at the oceanward extension of the transform margin *sensu stricto*, and the continental interior, both of which are underlain by thick continental crust (Figure 1.30b).

Chapters 14 and 15 show how important the different topographies and crustal thickness distributions of these three tectonic settings of the transform margin are for the distribution of the source and reservoir rocks along the transform margin. Different topographies of these three settings also control different migration patterns (see Chapter 17).

Unlike continental fault patterns of transform faults discussed earlier, which are developed by deformation of already-existing crust, faults developed in the adjacent oceanic crust have a very different thermal regime and mechanical behavior, at least in some slow spreading systems and faster systems, where the accretion of the oceanic crust is magma-rich. In these cases, as

https://doi.org/10.1017/9781108686631.002

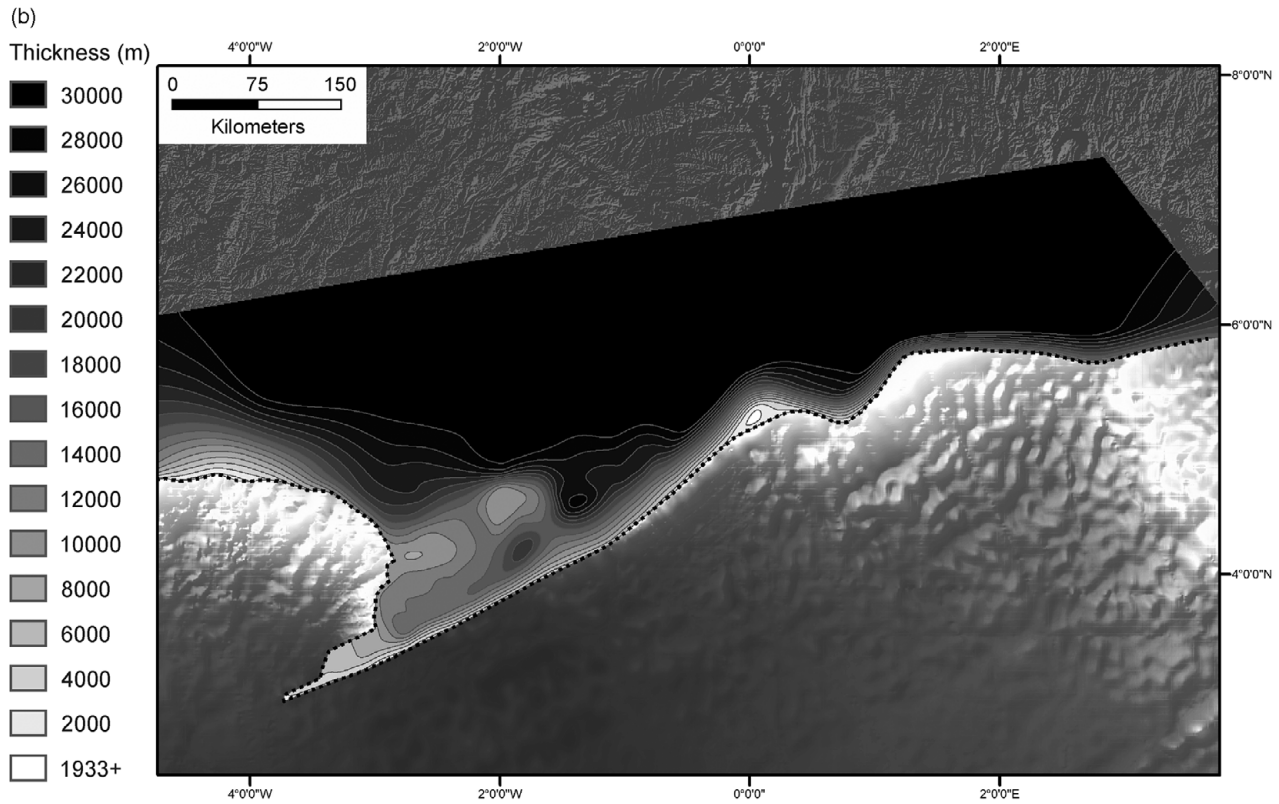

Figure 1.30 (b) Thickness map of the continental crust of the Romanche Transform margin, Africa, with location of the boundary between continental and oceanic crusts (black dotted line), on top of offshore bathymetry and onshore topographic maps (Baranowski, 2020, unpublished student project). Background topography and bathymetry maps are from GEBCO (2019).

discussed in detail in Chapter 5, the fault propagation takes part in new crust development zones. Perhaps the best way of discussing the characteristics of these faults is to study ridge transforms, as described earlier in this chapter. Accordingly, their deformation reacting to the developed transtension and transpression is different from that of continental strike-slip faults.

As pointed out by Bonatti et al. (2005), Nemčok et al. (2012a), and Maia et al. (2016), even as small a change in spreading vector as 5–10° can result in a pure strike-slip regime changing into transtension or transpression.

The Vema Transform in the southern portion of the Central Atlantic provides an example of such a transtensional adjustment (Bonatti et al., 2005). The adjustment involves a development of the topographically anomalous Vema Transverse Ridge located to the south of the transform (Figure 1.31a). It has an asymmetric dip-oriented profile. The maximum height of its northern scarp reaches 4 km above the level of the adjacent transform trough floor (Figure 1.31b), while its southern flank plunges down gradually. A combination of reflection seismic profiles with submersible sampling shows that the entire southern flank is represented by a basalt layer, which crops out in the northern scarp, together with underlying sheeted dyke and gabbro layers underlain by mantle peridotites (Auzende et al., 1989; Bonatti et al., 2005), representing a southward-tilted multilayered feature exposed at its northern edge. The basalt layer thins erosionally at the summit.

The explanation for this flexure-related tilt (Figure 1.31c) is a few-degree sinistral spreading vector rotation, which loaded the Vema Transform with an extra extension component since 11–12 Ma. It lasted until 10 Ma. The resultant transtension controlled both the development of the northern scarp fault with a distinct dip-slip component and flexure-driven tilting of the slab between the Vema and Lema fracture zones. The slab dimensions are 300×80 km. The calculated uplift rate reached 2–4 mmy^{-1}.

The numerical simulation of the transtensional event indicates the importance of the thickness of the crust affected by the northern scarp fault (Bonatti et al., 2005). The thicker the slab, the larger the footwall uplift.

https://doi.org/10.1017/9781108686631.002

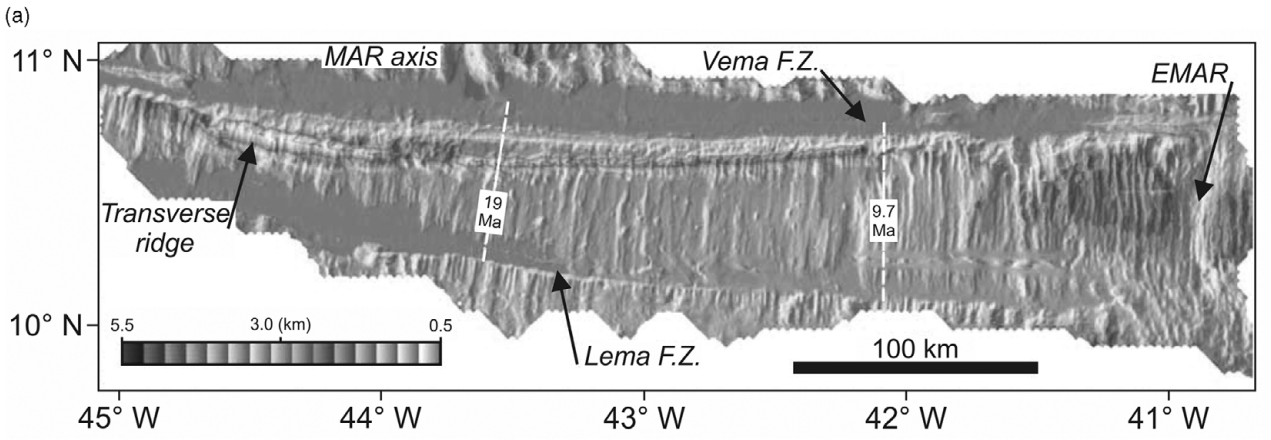

Figure 1.31 (a) Bathymetric map of the Vema ridge transform (Bonatti et al., 2005). The Vema transverse ridge abruptly starts at about 140 km west from the southern neighboring spreading ridge. The ridge-parallel structural architecture produced by the southern center changes its orientation where is crust is roughly 11 Ma old.

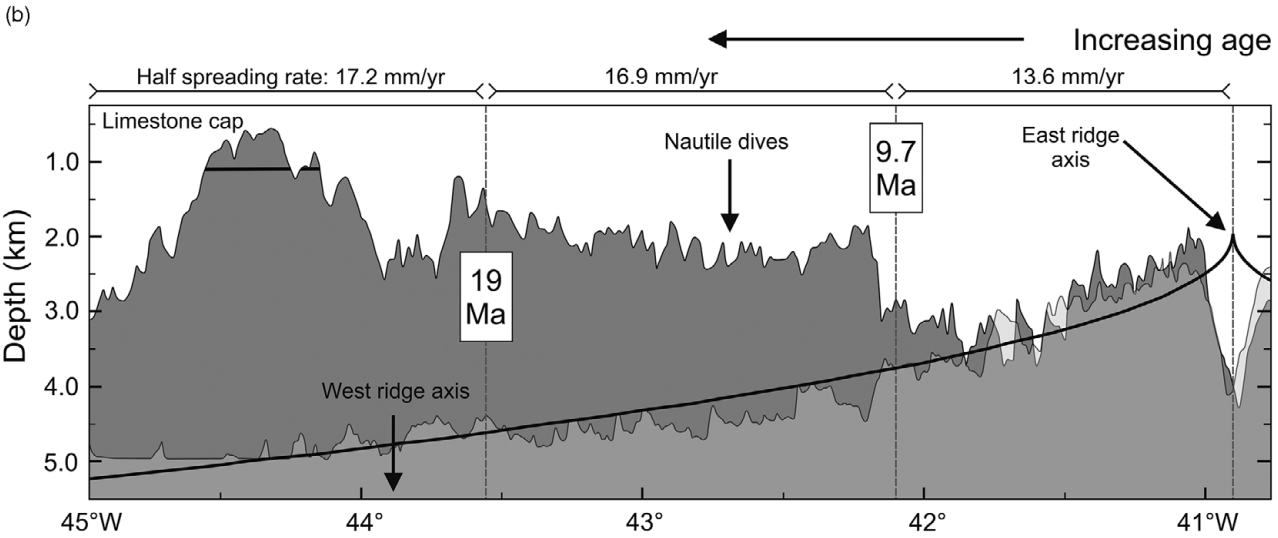

Figure 1.31 (b) Two east–west topographic profiles through the oceanic crust to the south of the Vema Transform fault (Bonatti et al., 2005). The normal oceanic crust accreted by the southern center, shown by light gray profile, deepens with its age due to its thermal subsidence. In contrast, the profile along the Vema transverse ridge indicates such thermal subsidence only until 10 Ma old crust. The older crust forms a prominent positive topographic feature reaching a maximum elevation of 4 km above the depths calculated from the thermal subsidence model (thicker black line).

The St. Paul ridge transform in the Equatorial Atlantic provides an example of transpressional adjustment (Maia et al., 2016). The adjustment involves segmentation of the transform fault with associated push-up ridges in the western transfer zone and a system of stepovers and faults with distinct thrust component in the central transpressional zone (Figures 1.32 and 1.33).

The transpression was triggered by the 5° sinistral rotation of the spreading vector that added an extra contraction component to the St. Paul Transform

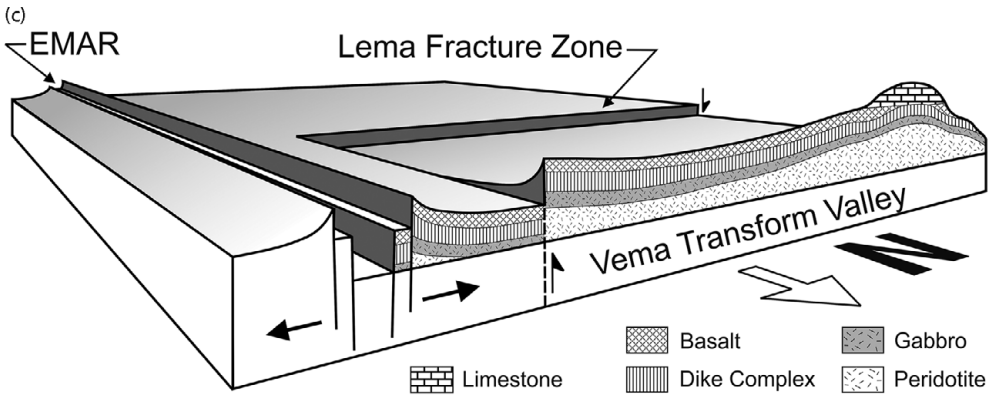

Figure 1.31 (c) Model of the flexure of the lithospheric slab between the Vema and Lema ridge transforms and their fracture zones (Bonatti et al., 2005).

Reprinted from the *Earth and Planetary Science Letters*, 240(3). Bonatti, E., Brunelli, D., Buck, W. R., Cipriani, A., Fabretti, P., Ferrante, V., Gasperini, L., and Ligi, M. Flexural uplift of a lithospheric slab near the Vema Transform (Central Atlantic): timing and mechanisms. 642–655. ©2005, with permission from Elsevier.

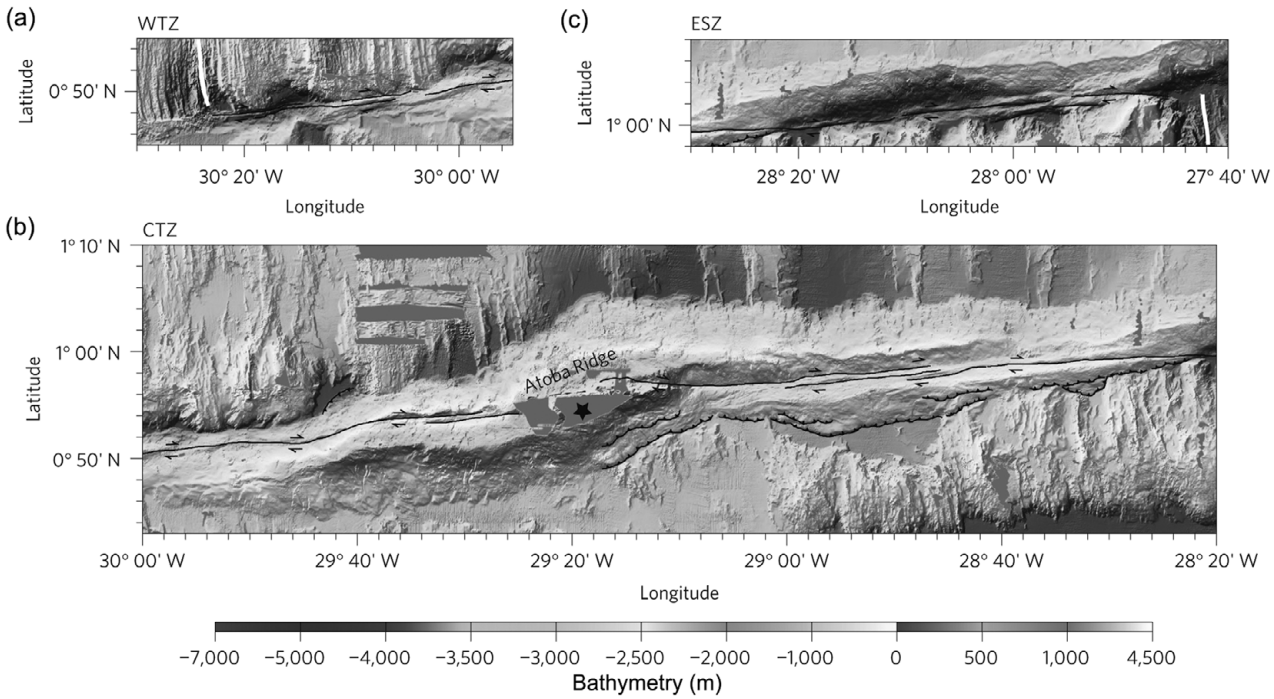

Figure 1.32 Bathymetric maps of the western transfer zone (a), central transpressional zone (b), and eastern shear zone (c) of the St. Paul Transform, Equatorial Atlantic (Maia et al., 2016). (a) The western transfer zone represents a multi-segment transform sub-parallel to the present-day spreading vector, which includes three push-up ridges in en echelon pattern. (b) The central transpressional zone represents a system of stepovers of the transform fault. The Atobá Ridge is the largest one. The lower southern flank of the zone contains thrust faults. (c) The eastern shear zone represents a transform fault crossing a deep trough.

Reprinted by permission from Springer Nature: *Nature Geoscience Letters*. Maia, M., Sichel, S., Briais, A., Brunelli, D., Ligi, M., Ferreira, N., Campso, T., Moungel, B., Brehme, I., Hemond, C., Motoki, A., Moura, D., Scalabrin, C., Pessanha, I., Alves, E., Ayres, A., and Oliveira, P. Extreme mantle uplift and exhumation along a transpressive transform fault, 9, 619–623. ©2016.

(Ligi et al., 2002; Bonatti et al., 2005). The transpressional adjustment was inhomogeneous, causing formation of the aforementioned restraining bends and offsets in the central zone and localized transpression in the western portion of the flexural transverse ridge (Maia et al., 2016). Associated thrusts create distinct positive topography and help to expose deep rocks (Figure 1.33).

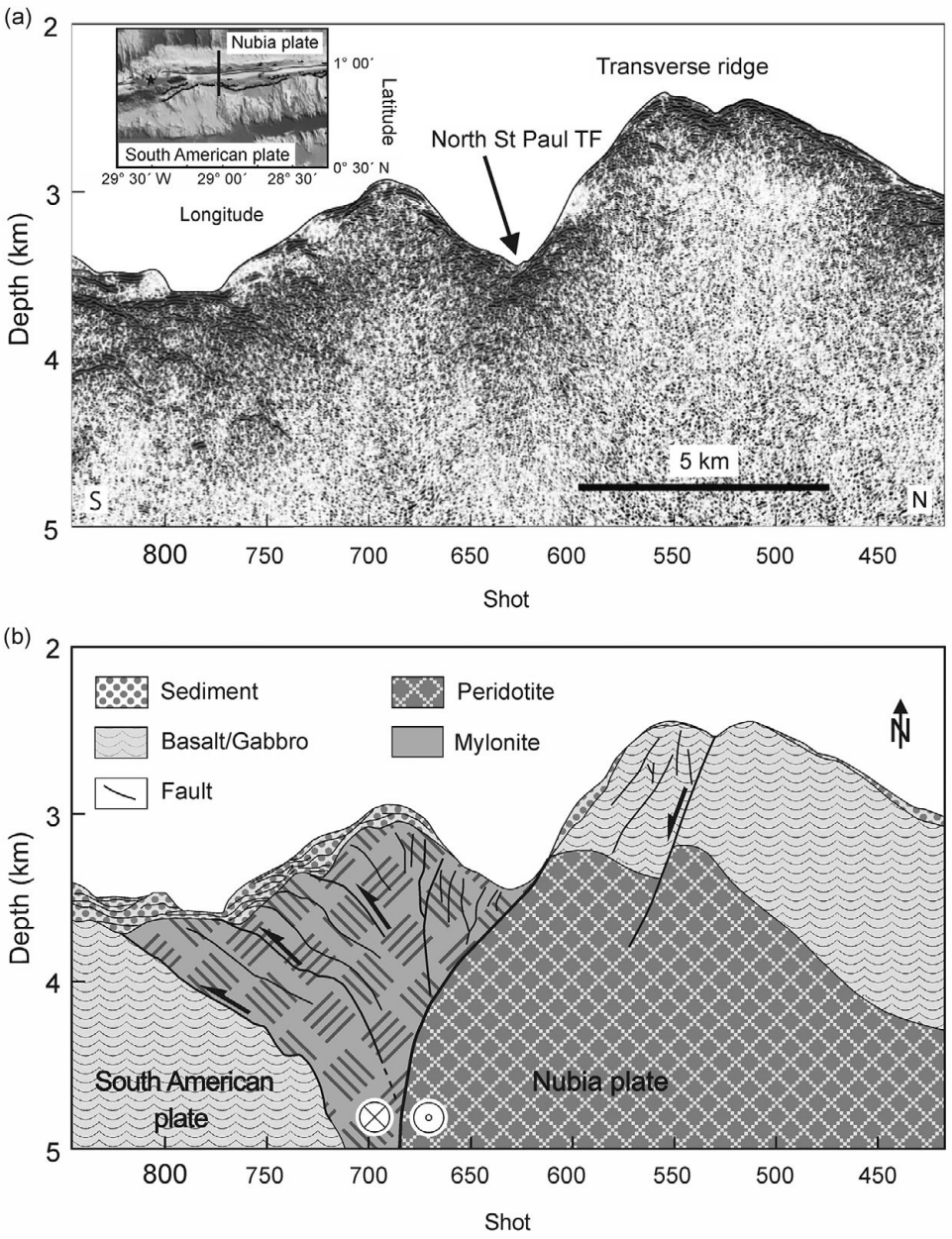

Figure 1.33 Uninterpreted and interpreted reflection seismic profiles through the St. Paul Transform (Maia et al., 2016). Reprinted by permission from Springer Nature: *Nature Geoscience Letters*. Maia, M., Sichel, S., Briais, A., Brunelli, D., Ligi, M., Ferreira, N., Campso, T., Moungel, B., Brehme, I., Hemond, C., Motoki, A., Moura, D., Scalabrin, C., Pessanha, I., Alves, E., Ayres, A., and Oliveira, P. Extreme mantle uplift and exhumation along a transpressive transform fault, 9, 619–623. ©2016.

The Clarion Transform, a further example of transpressional adjustment, indicates that the structural architecture of the intra-transform spreading centers in the external portions of the transform fault zone responded to transpression up to 5 Ma earlier than those in the central portion, indicating a complex spatial and temporal distribution of transpression-driven deformation (Morrow et al., 2016). Numerical simulation indicates an inhomogeneous distribution of compression and extension components in the segmented transform zone where individual intra-transform spreading centers act as buffers in the process of stress transmission through the entire zone.

Because transform fault zones in their continental–oceanic stage have both types of crust and structural

architectures involved on their opposite sides, they become the structures where two different mechanical behaviors and thermal regimes interact in control of the developing structural architecture. As shown by numerical simulation (Nemčok et al., 2012a), it took just a 9° change in the spreading vector trend between 108 and 92 Ma to cause transpression with a convergence component of about 3 mmy^{-1} across the Romanche Transform and its fracture zone. In combination with a younger transpressional event during 65 to 52 Ma, the continental side of the ocean–continent transform reacted by the 2.5 km uplift affecting a broad zone along the transform. The fact that the amount of uplift is insensitive to the modeled dip of the transform fault and affects a 30–40 km wide zone of the continental lithosphere, which has been significantly thermally weakened by the heat conduction and advection from the passing spreading centers and young oceanic crust, indicates a distinct pure shear component affecting the rock volume lacking a distinct flexural strength. One of the transpression-indicative features in this rock volume is a system of anticlines affecting only this zone.

https://doi.org/10.1017/9781108686631.002